January 2010

Dual-modality thermoacoustic and photoacoustic imaging

Manojit Pramanik
Washington University in St. Louis

WASHINGTON UNIVERSITY IN ST. LOUIS

School of Engineering and Applied Science

Department of Biomedical Engineering

Dissertation Examination Committee:
Prof. Lihong V. Wang, Chair
Prof. Frank C. P. Yin
Prof. Gregory M. Lanza
Prof. Igor R. Efimov
Prof. Joseph P. Culver
Prof. Younan Xia

DUAL-MODALITY THERMOACOUSTIC AND PHOTOACOUSTIC IMAGING

by

Manojit Pramanik

A dissertation presented to the Graduate School of Arts and Sciences
of Washington University in partial fulfillment of the
requirements for the degree of

DOCTOR OF PHILOSOPHY

May 2010
Saint Louis, Missouri

ABSTRACT OF THE DISSERTATION

Dual-modality thermoacoustic and photoacoustic imaging

by

Manojit Pramanik

Doctor of Philosophy in Biomedical Engineering

Washington University in St. Louis, 2010

Research Advisor: Prof. Lihong V. Wang

Diagnosis of early breast cancer is the key to survival. The combined contrasts from thermoacoustic and photoacoustic tomography (TAT and PAT) can potentially predict early stage breast cancer. We have designed and engineered a breast imaging system integrating both thermoacoustic and photoacoustic imaging techniques to achieve dual-contrast (microwave and light absorption), non-ionizing, low-cost, high-resolution, three-dimensional breast imaging. We have also developed a novel concept of using a negative acoustic lens to increase the acceptance angle of an unfocused large-area ultrasonic transducer, leading to more than twofold improvement of the tangential resolution in both TAT and PAT when the object is far from the scanning center.

A contrast agent could be greatly beneficial for early cancer diagnosis using TAT/PAT, because the early stage intrinsic contrast can be low. We have developed a carbon nanotube-based contrast agent for both TAT and PAT. In comparison with deionized water, single-walled carbon nanotubes (SWNTs) exhibited more than twofold signal

enhancement for TAT at 3 GHz, and in comparison with blood, they exhibited more than sixfold signal enhancement for PAT at 1064 nm wavelength. Using PAT in conjunction with an intradermal injection of SWNTs, we have shown the feasibility of noninvasive *in vivo* sentinel lymph node imaging in a rat model.

We have also developed and demonstrated molecular photoacoustic imaging using unique "soft-type" colloidal gold nanobeacons (GNBs) in the near-infrared region. GNBs represent a novel class of stable, colloidal gold nanoparticles, incorporating small metallic gold nanoparticles that can clear from the body when the particles are metabolically disrupted. We have also imaged the sentinel lymph node using different sizes of GNBs, showing that size plays an important role in their *in vivo* behavior and uptake to the lymph nodes.

In addition to providing diagnostic imaging, TAT and PAT can be used in therapy for real-time temperature monitoring with high spatial resolution and high temperature sensitivity, which are both needed for safe and efficient thermotherapy. Using a tissue phantom, these noninvasive methods have been demonstrated to have a high temperature sensitivity of 0.15 ^oC at 2 s temporal resolution (20 signal averages).

Acknowledgments

I am truly blessed with the best parents one could ever have. It is their hard work and sacrifice which guided me through the PhD phase of my life. They have always encouraged me to the utmost at every step of my career.

I am extremely grateful to Prof. Lihong Wang, my mentor, who introduced me to thermoacoustic and photoacoustic tomography and their application in biomedical imaging. It is a most honorable experience for me to receive the doctoral degree under his supervision. His consistent guidance and ideas helped me a lot in taking a correct approach to various problems and shifted the paradigm from a narrow spectrum of thinking to a broader one.

I would like to thank Dr. Frank Yin, Chairman of The Department of Biomedical Engineering, for giving me the opportunity to be part of the department and all the facilities. I owe my heartiest gratitude to Dr. Gregory Lanza, Dr. Joseph Culver, Dr. Igor Efimov, and Dr. Younan Xia, my committee members, for their constructive suggestions and their time serving on my dissertation committee.

I would like to thank our collaborators Dr. Balaji Sitharaman, Dr. Dipanjan Pan, and Dr. Angana Senpan for giving me the opportunity to work with them and learn about contrast agents, nanomedicine, and nanotechnology.

I would like to thank all my lab members for their assistance, scientific discussions, and friendship over these years, inside and outside the lab. Special thanks go to Dr. Geng Ku, Dr. Chulhong Kim, Dr. Changhui Li, Dr. Kwang Hyun Song, Dr. Sri-Rajasekhar Kothapalli, and Dr. Alejandro Garcia-Uribe.

I would like to thank all the staff members of the Biomedical Engineering Department (Amanda Moritz, Katie Moulton, and Karen Teasdale) for their help. Special thanks to Glen Reitz for his friendship and help throughout my stay in the department. Special thanks also to Jim Ballard for correcting all my manuscripts, presentations, and proposals, as well as my dissertation, and to John Witty for his help in the machine shop.

On a personal note, I would like to thank my friends Saurish, Poulomi, Satyaki, MrinmoyDa, GargiDi, Debomita, Tanika, Pinaki, Satya, Debajit, and Sudeshna for making my life enjoyable in St. Louis. I would also like to thank the St. Louis Cricket Club and the Yorkers Cricket Team for letting me have a life outside of research.

<div align="right">

Manojit Pramanik

</div>

Washington University in Saint Louis
May 2010

Dedicated to my parents.

Contents

List of Tables

List of Figures

Abbreviations

AFM	Atomic force microscopy
ALND	Axillary lymph node dissection
ANSI	American National Standards Institute
AUS	Axillary ultrasound
BV	Blood vessel
CNR	Contrast-to-noise ratio
DCIS	Ductal carcinoma in situ
DOT	Diffuse optical tomography
DI	Deionized water
EM	Electromagnetic
FDA	Food and Drug Administration
FDTD	Finite difference time domain
FFDM	Full-field digital mammography
FOV	Field of view
GNBs	Gold nanobeacons
HIFU	High intensity focused ultrasound
HRTEM	High resolution transmission electron microscopy
i.d.	Inner diameter
LDPE	Low-density polyethylene
MAP	Maximum amplitude projection
MO	Mineral oil
MPE	Maximum permissible exposure
MRI	Magnetic resonance imaging
MWNTs	Multi-walled carbon nanotubes
NIR	Near infrared
OCT	Optical coherence tomography
o.d.	Outer diameter
PA	Photoacoustic
PAT	Photoacoustic tomography
PDI	Polydispersity index
PET	Positron emission tomography
PRR	Pulse repetition rate

rf	Radio frequency
SAR	Specific absorption rate
SLN	Sentinel lymph node
SLNB	Sentinel lymph node biopsy
SNR	Signal-to-noise ratio
SWNTs	Single-walled carbon nanotubes
TA	Thermoacoustic
TAT	Thermoacoustic tomography
TEM	Transmission electron microscopy
UST	Ultrasonic transducer
UHF	Ultra high frequency

Chapter 1

Introduction to thermoacoustic and photoacoustic tomography

Breast cancer is currently the second leading cause of cancer deaths in women (after lung cancer) and is the most common cancer among women, excluding nonmelanoma skin cancers. One woman in eight either has or will develop breast cancer in her lifetime. In 2009, there were an estimated 192,370 new cases of breast cancer among females, and 1,910 new cases among males. About 40,170 female and 440 male died of breast cancer in 2009 in the USA [1].

Despite major strides in cancer prevention and treatment during the past decades, there has been only a modest effect on overall survival. Newer treatment regimens have had some impact on breast cancer mortality, but most of the observed reduction in mortality is due to the wider use of screening mammography and detection at earlier stages. National statistics have shown a shift to more early stage diagnoses of breast cancer. Some of these are smaller invasive cancers, but others are ductal carcinoma in situ (DCIS), which now represents 20-30% of mammographically detected breast

cancers. The absolute number of these cases began increasing in the late 1980's and 1990's, when screening prevalence increased in the USA.

Early diagnosis is the key to cancer survival. At present, x-ray **mammography** is the only mass screening tool used for detecting nonpalpable breast cancers. The sensitivity of mammography for breast cancer detection is good, and randomized trials have documented that its widespread use results in a reduction in breast cancer deaths. However, despite great strides in quality control and interpretation standards, its sensitivity is limited in the dense breast. Moreover, the use of ionizing radiation (x-ray) limits the frequency of mammographic screening. In spite of using low doses of radiation, repeated x-ray exposure can cause problems. Further, it is difficult to image dense glandular tissue and the region close to the chest wall or underarm. And finally, very early stage tumors that do not yet exhibit microcalcifications cannot be imaged. Recent technological developments have resulted in the advent of full-field digital mammography (FFDM). A recent trial showed that FFDM was significantly better than film-screen mammography for women under age 50 and for women with dense breasts [2]. While FFDM might represent an improvement for a subset of patients with dense breasts, its ability to make early stage diagnoses is limited by the same factors as screen-film mammography.

Sonography is now routinely used in breast imaging centers as an essential complement to physical examination and mammography for the evaluation of breast masses, and as a tool to guide breast interventions. Sonography can readily differentiate cystic from solid breast masses and can be used to characterize masses, although it is not tissue specific. Ultrasound specificity in breast cancer detection is limited by the overlapping acoustic characteristics of benign and malignant solid lesions. Current ultrasound scanners can detect and resolve breast lesions a few millimeters in size.

Anecdotally breast screening ultrasound in high risk women can find additional mammographically occult non-palpable breast cancers. A prospective multi-institutional national screening trial comparing mammography to mammography plus sonography in high risk women with dense breasts is now underway, and the results are expected soon. Other sensitivity studies which have compared mammography, ultrasound, and magnetic resonance imaging (MRI) have shown that ultrasound does not perform as well as MRI for invasive cancers, nor as well as mammography for ductal carcinoma *in situ*. Ultrasound may miss tiny nonpalpable breast tumors because they have low acoustic contrast, or because of operator variability [3].

<u>MRI</u> offers improved tissue characterization compared to other imaging modalities. Contrast-enhanced MRI is increasingly used as a complementary diagnostic modality in breast imaging [4]. The sensitivity of breast MRI in the detection of malignancy has consistently been reported to be excellent. However, the specificity has been rather variable. Study protocols and imaging techniques are not standardized, and there is still a great deal of uncertainty about the role of MRI in clinical practice. MRI has been shown to be the best modality to image the extent of breast cancer in patients with newly diagnosed breast cancer. It has also been shown to be best at detecting unsuspected breast cancer in the contralateral breast of patients with newly diagnosed breast cancer [5], as well as detecting breast cancer when screening high risk women [3]. The American Cancer Society issued new guidelines suggesting that high risk women be screened with MRI as an adjunct to mammography [6]. MRI, however, is the most costly breast imaging modalities and requires the use of contrast agents which are not innocuous. Recent reports of kidney disease following MRI contrast agent administration are concerning, even though this is a rare occurrence [7]. Furthermore, conventional MRI gives only morphological information.

Thermoacoustic (TA) tomography (TAT)

In microwave induced TAT, a short-pulsed microwave source irradiates the tissue. The dominant effect of microwaves on biological tissues is thermal. When electromagnetic energy is transformed in to kinetic energy in absorbing molecules, heating and subsequent thermoacoustic emission occurs in the medium. Thus the absorbed microwave energy causes emission of thermoacoustic waves from within the irradiated tissue. The dielectric properties of the tissues determine their patterns of energy deposition upon irradiation. The relatively long wavelength of the microwave, e.g., 1.5–3.5 cm at 3 GHz in tissues (10 cm in vacuum), serves to illuminate the tissue relatively homogeneously, although heterogeneity on the scale of the wavelength can result. The microwave heating must be rapid to produce thermoacoustic waves of sufficiently high frequencies; in other words, a static temperature distribution or slow heating does not produce thermoacoustic waves. A wide-band ultrasonic transducer acquires the thermoacoustic waves, which carry the microwave absorption properties of the tissue.

The dielectric properties of normal and malignant tissues (Fig. 1.1) vary appreciably over a range of frequencies [8, 9]. Soft tissues of high water/sodium content have a large increase in the relative dielectric constant at frequencies below 0.1 GHz and a large increase in conductivity at frequencies above 1 GHz [10]. At frequencies below 0.1 GHz, the large increase in the relative dielectric constant is due to the charging of cell membranes, with smaller contributions coming from the protein constituents and possibly ionic diffusion along surfaces in the tissue. At frequencies above 0.1 GHz, the changes in the relative dielectric constant and conductivity probably reflect relaxation of the tissue proteins and protein-bound water, as well as other sources. At frequencies above 1–5 GHz, the dipolar relaxation of water primarily determines
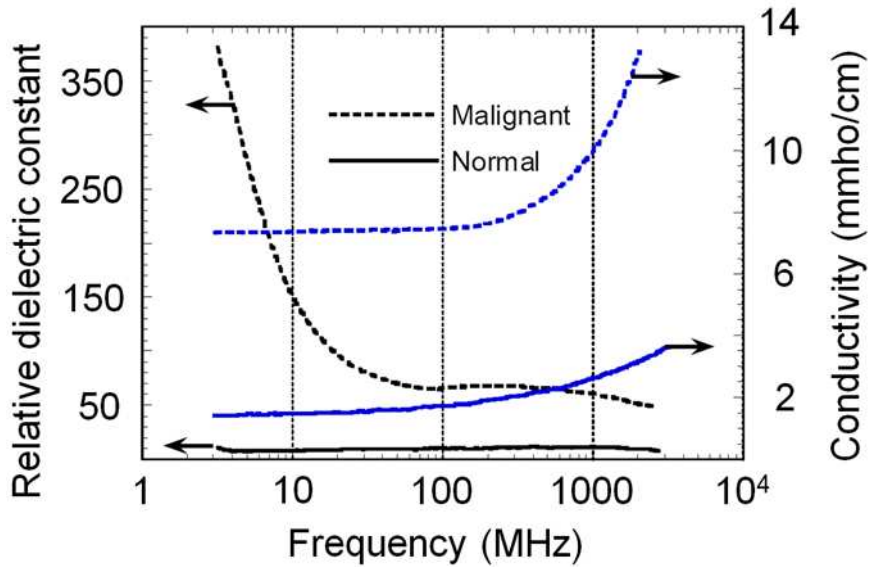
Figure 1.1: Dielectric properties of human breast tissues [8].

the change in the dielectric properties. Because of the free water and sodium in malignant tissue, conductivity increases significantly with frequency. In addition, the "static" permittivity of the free water contributes predominantly to the permittivity of tissue at ultra high (> 300 MHz) frequencies (UHF). The radio frequency (rf) contrast between tumor tissue and normal tissue, about a factor of 4 as shown in Figure 1.1, is primarily caused by the extra water and sodium in the tumor tissue [11]. This large contrast is the primary motivation for our research on TAT, which measures the conductivity contrast. In comparison, x-ray contrast is typically only a few percent among soft tissues. Based on the data in Figure 1.1, the $1/e$ penetration depth can be calculated (Fig. 1.2). Since TAT can sustain several $1/e$ attenuations, it can image multiple cm deep in tissue.

The phenomenon of generating acoustic waves in electromagnetically lossy media using rf pulses was used in the 1980s for imaging of biological tissues [12–15]. These pioneering works, however, produced only planar images instead of tomographic or depth-resolved images [16].

5
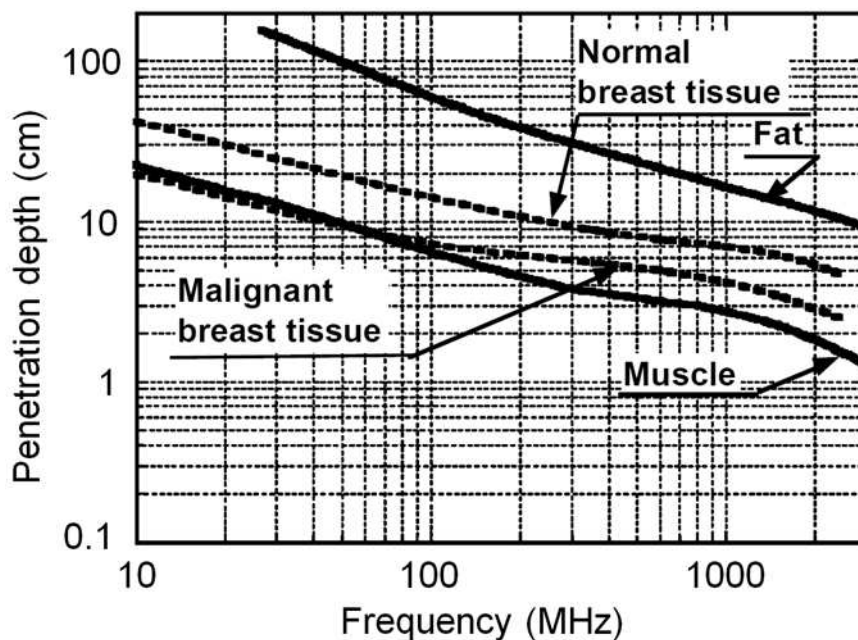
Figure 1.2: Penetration depths versus frequencies [8].

TAT combines the advantages of pure-ultrasound and pure-rf imaging [17, 18]. Traditional imaging technology with pure ultrasound (ultrasonography) offers satisfactory spatial resolution but poor soft-tissue contrast [19], while pure-rf imaging provides good imaging contrast but poor spatial resolution [20–28]. The best spatial resolution in pure-rf imaging is on the order of 10 mm despite its near-field operation, whereas the achievable resolution in pure-ultrasound imaging is ∼1 mm. TAT bridges the gap between them by physically integrating ultrasound and rf. It provides both satisfactory spatial resolution (0.5 mm) and high soft-tissue contrast.

Photoacoustic (PA) tomography (PAT)

A. G. Bell first reported the observation of sound generated by light in 1880 [29]. When a short-pulsed laser irradiates biological tissues, wideband ultrasonic waves (PA waves) are induced as a result of transient thermoelastic expansion. If the laser

6

pulse is so short that thermal diffusion is negligible – a condition referred to as thermal confinement, the photoacoustic wave equation in an inviscid medium is given as [30]:

$$(\bigtriangledown^2 - v_s^{-2}\partial^2/\partial t^2)p(\vec{r},t) = -(\beta/C_P)\partial H(\vec{r},t)/\partial t \qquad (1.1)$$

Here, $p(\vec{r},t)$ denotes the acoustic pressure at location $\vec{r}$ and time t, v_s denotes the acoustic speed, β denotes the thermal expansion coefficient, C_P denotes the specific heat at constant pressure, and H denotes the heating function defined as the thermal energy converted per unit volume and per unit time. The left-hand side of this equation describes the wave propagation, whereas the right-hand side represents the source term. The source term is related to the first time derivative of H. Therefore, time-invariant heating does not produce a pressure wave, only time-variant heating does. In practice, laser heating must be rapid to produce PA waves efficiently.

The initial photoacoustic pressure excited by a $\delta(t)$ laser pulse is $p_0 = \Gamma\eta_{th}A_e$, where $\Gamma = \beta V_s^2/C_p$ denotes the Grueneisen parameter (dimensionless), A_e denotes the specific optical absorption (energy deposition) (J/cm^3), and η_{th} denotes the percentage of the absorbed energy that is converted in to heat. Since $A_e = \mu_a F$, where μ_a denotes the optical absorption coefficient and F denotes the optical fluence (J/cm^2), we have $p_0 = \Gamma\eta_{th}\mu_a F$. In soft tissue imaging, Γ and η_{th} are usually treated as constants.

In PAT, a short-pulsed laser irradiates the tissue, and the PA waves are measured by wide-band ultrasonic transducers around the tissue. A key task in PAT is to determine the optical absorption density (or specific absorption) distribution from the measured photoacoustic data, i.e., to map the optical absorption heterogeneity of the tissue. We can use a focused ultrasonic transducer to localize the photoacoustic sources and then construct the images directly from the data [31–38]. Alternatively, we can use an

7

unfocused ultrasonic transducer to acquire the data and then reconstruct the optical absorption distribution [39–46]. Since optical absorption is sensitive to physiological parameters such as the total concentration and oxygenation of hemoglobin, PAT can provide functional imaging. Optical absorption contrast due to both oxy- and deoxy-hemoglobin relative to background can be as high as 10:1 or even 100:1, depending on the optical wavelength [47].

PAT overcomes the limitations of other optical modalities and combines optical contrast with ultrasonic resolution. In PAT, the contrast is related to the optical properties of the tissue, but the resolution is not limited by optical diffusion caused by multiple photon scattering. It has been shown experimentally that the spatial resolution is bandwidth- and diffraction-limited by the photoacoustic waves [48] because ultrasonic scattering is weak compared to optical scattering. PAT does not depend on ballistic or backscattered light as optical coherence tomography (OCT) does. Any light, including both singly and multiply scattered photons, contributes to the imaging signal. As a result, the imaging depth in PAT is relatively large. Furthermore, PAT is free of speckle artifacts [49], which plague OCT and ultrasonography. Photoacoustic waves propagate one way to the ultrasonic transducers in PAT, whereas ultrasound propagates two ways in conventional ultrasonography. Therefore, PAT is less susceptible to acoustic tissue heterogeneity. The motivation for developing PAT is summarized in Table 1.1. The key advantages of PAT include (1) a combination of high optical contrast and high ultrasonic resolution, (2) good imaging depth, (3) no speckle artifacts, (4) scalable resolution and imaging depth with ultrasonic frequency, (5) the use of nonionizing radiation (used properly, both laser and ultrasound pose no known hazards to humans), and (6) relatively inexpensive cost.

Table 1.1: Comparison of various imaging modalities.

Modalities	OCT [50]	DOT [50]	Ultrasonic imaging (UI, 3 MHz) [51]	PAT [47, 52]
Contrast	Good (scattering & polarization)	Excellent (functional)	Poor for early cancers (backscattering)	Excellent (=DOT)
Resolution	Excellent ($\sim$10 μm)	Poor ($\sim$5 mm)	Excellent & scalable ($\sim$0.5 mm)	Excellent (= UI)
Imaging depth	Poor ($\sim$1 mm)	Good ($\sim$5 cm)	Good & scalable ($\sim$6 cm)	Good (= DOT)
Speckles	Strong	None	Strong	None
Scattering	Strong ($\sim$100 /cm)	Strong ($\sim$100 /cm)	Weak ($\sim$0.1 /cm)	

In **Chapter II,** we present the design and engineering of a breast imaging system that integrates both thermoacoustic and photoacoustic techniques to achieve dual contrast (microwave and light absorption) imaging [53]. The breast scanner system includes the breast holder, the microwave source and delivery subsystem, the laser source and delivery subsystem, image reconstruction subsystem (software), and the master control of all subsystems. This scanner is non-ionizing, low-cost, and can potentially provide high-resolution, dual-modality, three-dimensional images of the breast. The scanner uses front instead of side breast compression, and dry instead of gel ultrasonic coupling. We validate the proposed imaging system with tissue phantom imaging, and quantify the resolution, imaging depth, signal-to-noise ratio, and contrast.

We also study how the tangential resolution and the image quality of the proposed system depend on the transducer [54]. The use of large active area diameter flat transducers for acquiring thermoacoustic and photoacoustic images gives rise to poor tangential resolution (depending on the object location inside the scanner) and some artifacts related to the object shape recovery. We present a novel concept of using

a negative acoustic lens to increase the acceptance angle of an unfocused large-area ultrasonic transducer (detector), leading to more than twofold improvement of the tangential resolution in both TAT and PAT. For a given transducer bandwidth, the aperture size of the detector affects the tangential resolution greatly when the object of interest is near the detector surface. We are able to overcome such tangential resolution deterioration by attaching an acoustic concave lens, made of acrylic, in front of the flat detector surface. We then quantify the tangential resolution improvement using phantom images. We also show that the use of the negative lens preserves the shape of an object after the image is reconstructed.

In **Chapter III,** we describe studies on the feasibility of single-walled carbon nanotubes (SWNTs) as a multimodal contrast agent [55]. Although high rf and optical contrast exists between well-developed malignant tumor tissue and normal tissue, the contrast during the early stages of cancer maybe insufficient. Thus, targeted contrast agents can be greatly beneficial for early cancer diagnosis using TAT/PAT, increasing cancer contrast and targeting specific gene expressions to improve early detection limits. We develop a carbon nanotube-based contrast agent for both TAT and PAT. In comparison with deionized water (DI), single-walled carbon nanotubes exhibit more than twofold signal enhancement for TAT at 3 GHz. In comparison with blood, they exhibit more than sixfold signal enhancement for PAT at 1064 nm wavelength. We also study the clinical application of SWNTs as a contrast agent in noninvasive sentinel lymph node (SLN) mapping using PA imaging [56].

In **Chapter IV,** we develop and demonstrate molecular PAT using unique colloidal gold nanobeacons (GNBs) [57, 58]. GNBs represent a novel class of stable, phospholipid-encapsulated, colloidal gold nanoparticles, incorporating small metallic spherical or rod-shaped gold nanoparticles (2–4 nm) that can clear from the body

when the particles are metabolically disrupted. These nanoparticles target vascular markers of thrombosis (i.e., fibrin) and angiogenesis (i.e., integrin) with enhanced specificity. Their particle size ($\sim$200 nm) constrains their distribution within the vasculature, preventing interactions with the same epitopes in extravascular tissues. Preliminary results confirm our hypothesis that GNBs act as an exogenous contrast agent, and that the strong PA signal in the near infrared (NIR) region points to the potential of this platform for molecular PAT. The concept of molecular PAT of fibrin, a critical component of intravascular thromboses, are studied *in vitro*. We also demonstrate the *in vivo* imaging capability of GNBs by imaging sentinel lymph nodes in rats. We further show that the lymphnode distribution and *in vivo* trafficking of the GNBs are governed by the hydrodynamic radii of these particles.

In **Chapter V,** we present another novel application of the TA and PA techniques, in monitoring temperature noninvasively [59]. During thermotherapy it is necessary to monitor the temperature distribution in the tissues for the safe deposition of heat energy and efficient destruction of tumor and abnormal cells. Thus, real-time temperature monitoring with high spatial resolution ($\sim$1 mm) and high temperature sensitivity (1 ^{o}C or better) is needed. Using a tissue phantom,we demonstrate that the TA/PA technique has high temporal resolution and temperature sensitivity. Because both TA and PA signal amplitudes depend on the temperature of the source object, the signal amplitudes can be used to monitor the temperature. The signal is proportional to the dimensionless Grueneisen parameter of the object, which in turn varies with the temperature of the object. The deep tissue imaging capability of these techniques can potentially lead us to *in vivo* temperature monitoring in thermal or cryogenic applications.

Finally, in **Chapter VI,** we summarize this work and suggest future directions.

Chapter 2

A novel dual-modality breast imaging system

2.1 Design and evaluation of a novel breast cancer detection system*

2.1.1 Introduction

Diagnosis of early breast cancer depends on the recognition of subtle changes in breast tissue properties, such as mechanical properties (hardness), optical absorption, rf absorption (change in ion and water concentrations). Treatment is more likely to work well when cancer is found early. At present, x-ray mammography is the only mass screening tool. However, there are several limitations of mammography [60]. Sonographic examination of the breast with high-frequency multi-element linear-array transducers are not so useful because of the poor soft tissue contrast. MRI for breast

---

screening has a high sensitivity, but it is the most expensive breast imaging modalities. To overcome some of these difficulties, we have developed a breast screening modality that combines nonionizing radio frequency electromagnetic waves and a visible/NIR laser for the early breast cancer screening based on thermoacoustic/photoacoustic tomography. The rf contrast between malignant tumor tissue and normal human breast tissue is about a factor of 4 [8]. A more recent study has shown the dielectric-properties contrast between malignant breast tissues and normal adipose-dominated breast tissues is large, ranging up to 10:1 [61]. Extra water and sodium in the tumor tissue cause the enhanced dielectric property of the malignant tumor tissue [11]. The dielectric properties of malignant tumors show no significant variation with tumor age [62], suggesting that a large contrast could exist even at earlier stages of tumor development. This large contrast is the primary motivation for our research on TAT, which measures the conductivity contrast. In comparison, x-ray contrast is typically only a few percent among soft tissues. TAT and PAT are capable of giving additional information such as water/ion concentration, blood volume, and oxygenation level of hemoglobin. Because these parameters can change during the early stages of cancer, the combined TAT and PAT can potentially enhance early stage cancer diagnosis ability. Integrating the two modalities in a single system will have the following advantages: (1) It will reduce the image acquisition time, (2) It will be cost effective, and (3) Acquiring two images in the same setup avoids moving and realigning the patient all over again. Moreover, TAT and PAT are both highly compatible with ultrasonography as they share the same ultrasound detection system. Therefore, in the future, ultrasound pulse-echo imaging can also be incorporated very easily into this system.

2.1.2   System description

In x-ray mammography the breast is compressed from the sides to reduce the thickness so that x-ray penetrates well. This compression causes some discomfort for the patient. Moreover, one needs to take a mammogram from different angles to interpret the images accurately. Our breast scanner is designed to minimize the compression pain. The breast is compressed from the front (nipple side) to give it a cylindrical shape. This technique has advantages in three ways. First, transducers can scan around the cylindrical breast for a full 360^0 and along the length to obtain a full three-dimensional (3D) data set. Full 3D reconstruction can be done to view the breast in 3D. Second, compression from the front is less painful than one from the side. Third, microwave/laser irradiation from the front of the cylindrically compressed breast can potentially penetrate deep enough to image near the chest wall.

A cylinder made out of low-density polyethylene (LDPE), which has low ultrasound absorption and an acoustic impedance close to that of water ($\sim$1.5 at room temperature), holds the compressed breast. LDPE minimizes the loss of ultrasound signal due to a mismatched boundary. Figure 2.1(a) shows the schematic diagram of the scanner. The breast is inserted into the front opening of the scanner. A supporting plate made of acrylic pushes the breast from the rear opening of the scanner to obtain a cylindrical shape. After the compression, a brass retaining ring holds the supporting plate in position. The microwave/laser source is kept behind the scanner, and a horn antenna is pushed inside the scanner from the opening to irradiate rf/light on the compressed breast. An aluminum cylinder (rotating cylinder) with many holes holds the ultrasonic transducers around the breast holder cylinder. During data collection, the rotating cylinder is turned by a worm-gear mechanism and a stepper motor. The
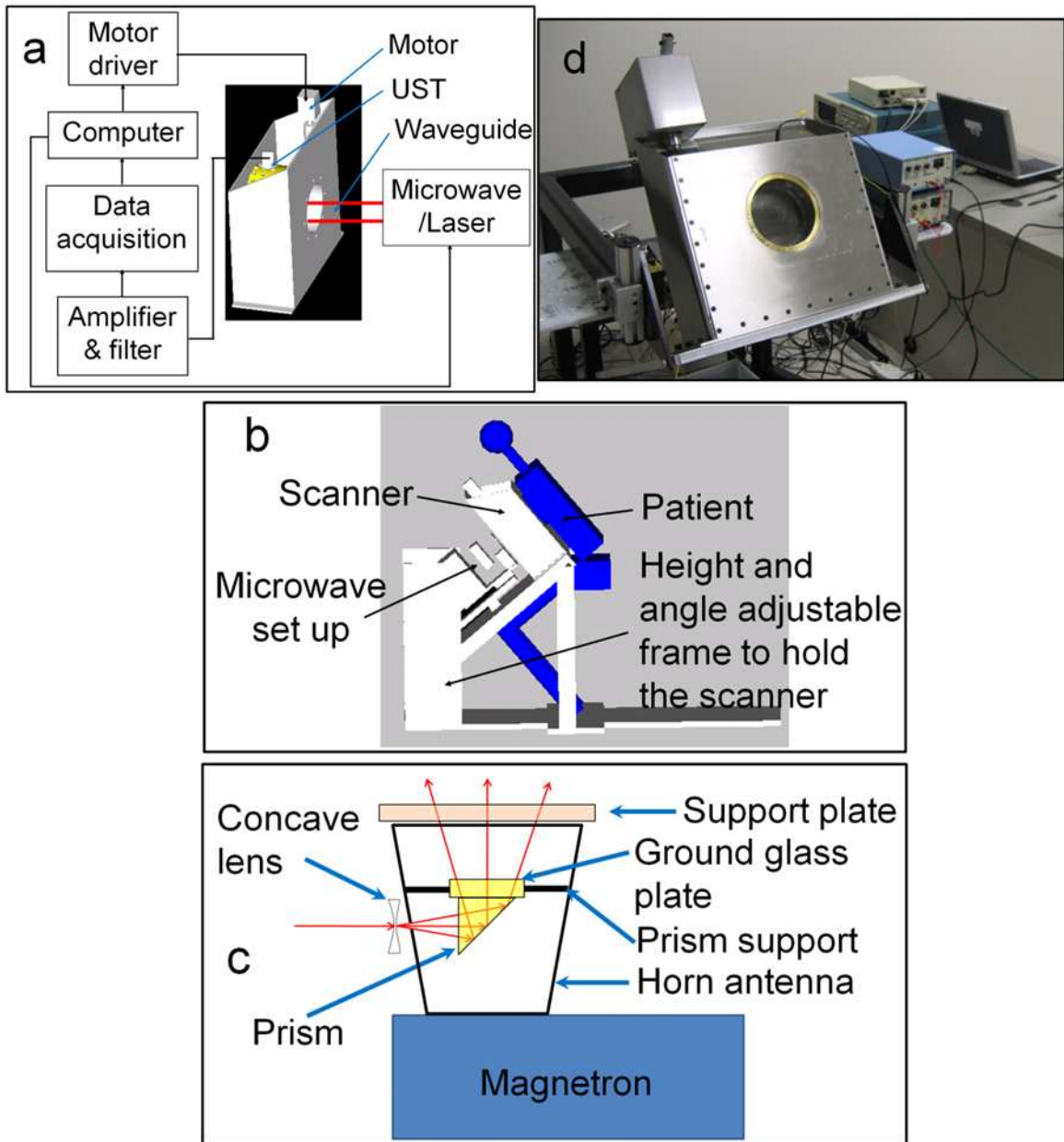
Figure 2.1: Design of the system. (a) Schematic diagram of the breast scanner. UST: Ultrasonic Transducer. (b) The position of the patient with respect to the system. (c) Design of the integrated microwave horn antenna and optics. (d) Photograph of the system.

whole setup is mounted inside a stainless steel frame filled with mineral oil that facilitates the coupling of ultrasound to the transducer and also lubricates the worm gear. The scanner is placed on a height- and angle- adjustable metal frame. Figure 2.1(b) shows how a patient will be positioned, sitting on a chair and leaning onto the scanner.

The microwave/laser assembly is placed on the backside of the scanner behind the support plate. We illuminate the breast by either microwave or laser alternately for TAT/PAT. The microwave is delivered to the breast using a horn antenna, whereas the laser is delivered by a free space optical assembly. Some parts of the laser illumination system are incorporated inside the microwave horn antenna. As a result, we do not need to mechanically switch between the microwave and laser sources. The switching is electronic and instantaneous – once a TAT image is collected using microwave illumination, the microwave is switched off and the laser is switched on electronically to collect a PAT image. We have placed a prism and a ground glass plate inside the microwave horn antenna. Both are nonmetallic and therefore will not affect the microwave illumination. A drilled ∼10-mm-diam hole in one narrow wall of the horn antenna delivers the light. The laser beam is broadened by a concave lens placed outside the hole on the horn antenna, then reflected by the prism, and homogenized by the ground glass. Figure 2.1(c) shows a schematic diagram of the integration of the light delivery through the horn antenna.

Microwave source: A 3.0 GHz microwave source produces pulses of width 0.5 μs with a repetition rate of up to 40 Hz. The breast is illuminated using an air-filled pyramidal horn type antenna (WR284 horn antenna W/EEV flange, HNL Inc.) with an opening of 7.3×10.7 cm^2. The pulse energy is estimated to be around 10 mJ (= 20 kW $\times$ 0.5 μs) (within the IEEE safety standards [63]). The support plate and the

breast are separated from the opening of the antenna by about 1 cm, which is much less than the 10 cm microwave wavelength in air. Therefore most of the microwave energy either goes to the sample or gets reflected back to the horn antenna. Since the horn antenna is made of good conducting material with the only opening at the end facing the breast, most of the microwave energy is deposited into the breast even if microwave reverberation, due to impedance mismatch, exists between the breast and the horn antenna. Because the speed of the electromagnetic (EM) wave is so high, pulse broadening due to any reverberation is negligible. Therefore, the spatial resolution of TAT is not compromised.

The horn antenna is designed to transport the TE_{10} mode of EM waves, so the electric field is parallel (or nearly parallel for a horn) to the surface of either narrow side (y polarized in our system) and approaches zero near the inner surface of either narrow wall. By contrast, the electric field is nonzero near the surface of either wide wall. Therefore, opening the light delivery hole on the narrower side of the horn antenna (or wave guide) minimizes power leakage.

<u>Laser source</u>: A Q-switched Nd:YAG laser with a repetition rate of 10 Hz provides 6.5-ns-wide (at 1064 nm wavelength) laser pulses. The laser system can provide 850 mJ maximal output energy at 1064 nm wavelength. The laser is operated at this wavelength for maximum penetration into tissue. In this spectral region, absorption of melanin is relatively low and is not expected to limit the delivery of light into the breast, even for African American patients, as demonstrated in a previous study of diffuse optical imaging of the breast [64]. The laser beam is expanded by a concave lens, homogenized by a ground glass, and then directed onto the breast. This type of beam expansion scheme has been used extensively before [65–67]. The incident

laser fluence on the tissue surface is controlled to < 20 mJ/cm^2 to conform to the American National Standards Institute (ANSI) standards [68].

Detection of ultrasound: For detecting the ultrasound signal, 13-mm/6-mm-diam active area nonfocused transducers operating at 2.25 MHz central frequency (ISS 2.25 $\times$ 0.5 COM, ISS 2.25 $\times$ 0.25 COM, Krautkramer) are used. The transducers are scanned around the sample a full 360^0 to collect data at different angular positions. The signal is first amplified by a low-noise pulse amplifier (5072PR, OlympusNDT), then filtered electronically, and finally recorded using a digital data acquisition card (14 bit Gage Card). When microwave is the illumination source, a delay/pulse generator (SRS, DG535) triggers the microwave pulses and synchronizes the data sampling of the Gage Card. On the other hand, during laser illumination, the sync out of the laser system synchronizes the laser pulses and the data sampling of the Gage card. There are various reconstruction algorithms that can be used to reconstruct the TAT/PAT images from the raw data [48, 52, 69–71]. Here, a delay and sum (backprojection) algorithm is used for all image reconstruction. Figure 2.1(d) shows a photograph of the system.

2.1.3 Results and discussion

Integrating TAT/PAT: TAT and PAT have been separately used for tissue imaging by many groups [17, 31, 66, 69–76]. However, these two modalities have never been combined before in a single system for breast imaging. To substantiate the new design of integrating optics with the microwave horn antenna, we performed the following experiment. Four water-based agar gel cylinders with $\sim$10 mm diameter and $\sim$10 mm length were placed inside a mineral oil bath, and images were acquired. Figure
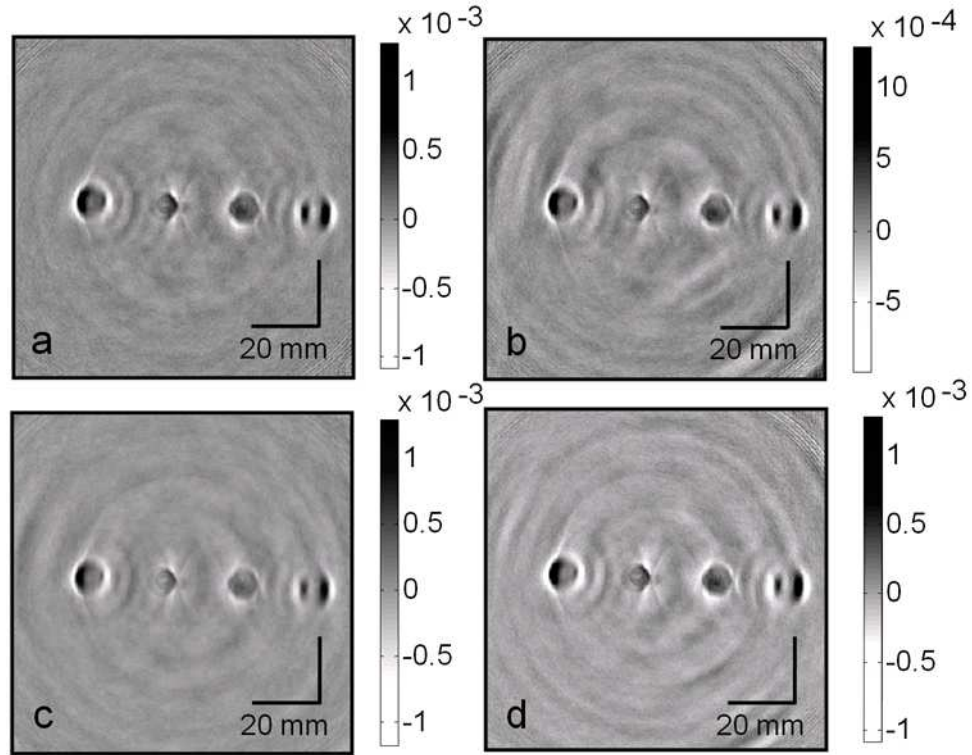
Figure 2.2: Reconstructed TAT images acquired with (a) the intact horn antenna, (b) a prism mounted inside the horn antenna, (c) a 5-mm-diam hole drilled in a sidewall of the horn antenna, and (d) the hole in the sidewall and the prism mounted inside.

2.2 shows the reconstructed images under different conditions. Figure 2.2(a) shows the original image with no optical device inside the microwave horn antenna. Figure 2.2(b) shows the image acquired when we put a prism inside the horn antenna. Figure 2.2(c) shows the image acquired after a hole of 5 mm diameter was drilled in the horn antenna, with no optical devices placed inside. Figure 2.2(d) shows the image obtained with the hole in the horn antenna and the prism placed inside. We can clearly see all four embedded objects with similar maximum signals (note that the gray scales are the same), except for some small background variations. From these four figures, we conclude that inserting the prism inside the horn antenna and drilling a hole in the sidewall do not cause much of signal loss or image distortion. These

experimental results strongly support the placement of optical components (here, the prism and the ground glass plate) inside the horn antenna to deliver light, and as a result we are able to integrate both light and microwave delivery.

Dry coupling: Unlike conventional ultrasound imaging, where coupling gel is used between the body and the ultrasonic transducer, we will be using dry coupling. Since the cylindrically compressed breast will be held tightly inside the LDPE breast holder, there will not be a large air gap to hinder ultrasound propagation. To test the feasibility of dry coupling we used a thin rubber balloon filled with mineral oil as a breast model. We put the balloon inside the breast holder chamber and then compressed it to a cylindrical shape that fit tightly inside the LDPE breast holder cylinder. This experiment was done with the scanner tilted at 45^0. There was a little bit of air gap at the top portion of the breast holder cylinder. Even with this little air gap between the balloon and the breast holder cylinder, when we made a transmission ultrasound measurement around the breast holder cylinder we saw very good ultrasound coupling. Figure 2.3 shows the transmission ultrasound coupling at different depths of the compressed balloon.

From Figure 2.3 we can see that, except near the two ends of the compressed balloon [Figs. 2.3(a) and 2.3(g)], the remaining planes have quite good ultrasonic transmission, which means we have good ultrasonic coupling. Even for those few planes where we do not have good coupling, we have good coupling over 80% of the area. Since we do tomography and collect data at different angular positions for reconstruction, losing data over 20% of the area will not affect the reconstructed image.
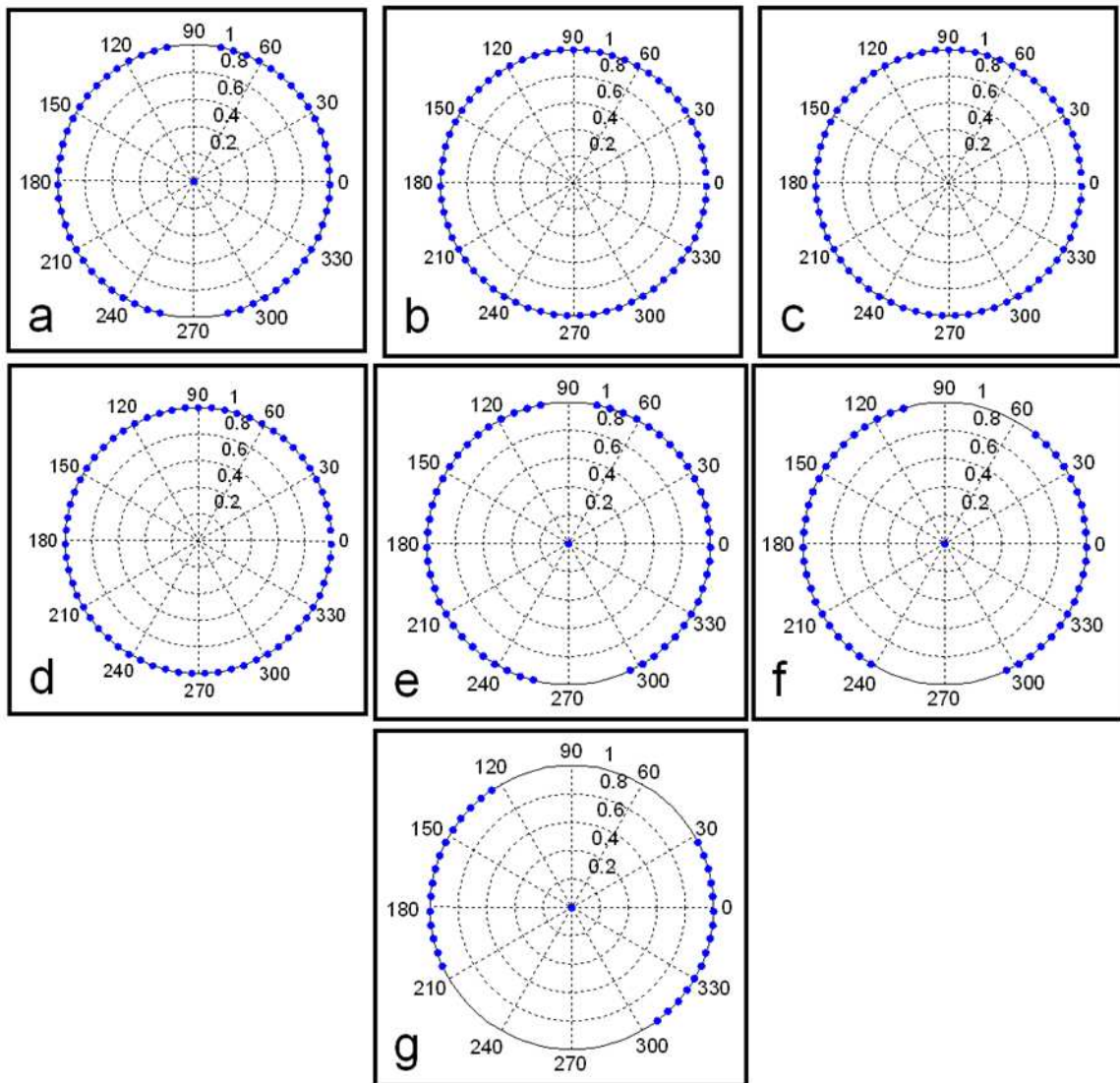
Figure 2.3: The transmission of ultrasound around the breast holder at different depths with a compressed balloon filled with mineral oil inside the breast holder chamber. The blue dots represent the transmission of ultrasound in that region. Depths: (a) 9.0 mm, (b) 1.2 cm, (c) 3.0 cm, (d) 4.3 cm, (e) 4.6 cm, (f) 4.8 cm, and (g) 5.0 cm.

Phantom experiments: We tested our system using tissue phantoms. Porcine fat was used as the background medium mimicking the fatty breast tissue, and water-based agar gel was used to model the inhomogeneity (target) in the background. The target gel objects were made of 2% agar, 2% salt and 96% water. Salt was added to increase the microwave absorption. A total of five target objects of diameter ∼6 mm were buried inside ∼7-cm-diam porcine fat. Two targets were made of clear gel. The remaining three targets were made of black gel; the color was obtained by mixing black India ink during the preparation of the agar gel. The location of the target objects inside the base fat is shown in Figure 2.4(a), a photograph of the phantom. The rf absorption contrast between the target gel and the background fat tissue was estimated to be ∼4:1. The optical contrast between the black target gel and background fat tissue was estimated to be ∼5:1. Both microwave and optical contrast were in the similar range of what we can expect in real human breast. The sample was placed inside the breast holder chamber, and the chamber was then filled with mineral oil, an ultrasound coupling medium. The sample was first illuminated with microwave and then by a 1064 nm wavelength laser.

Figures 2.4(b) and 2.4(c) show the reconstructed TAT images with 13- and 6-mm-diam active area ultrasonic transducers, respectively. The contrast and signal-to-noise (SNR) in the reconstructed images are ∼3.5:1 and 34, respectively, for a 13-mm-diam transducer [Fig. 2.4(b)] and the same numbers for a 6-mm-diam transducer are ∼2.5:1 and 20, respectively [Fig. 2.4(c)]. The resolution is calculated to be ∼1.2 and ∼0.7 mm for the images obtained by 13- and 6-mm-diam transducers, respectively. Distortion of the TAT images is noted. Although the target object has a circular cross section, the reconstructed images from TAT appear to be split in to two objects [Fig. 2.2, Fig. 2.4(b), and Fig. 2.4(c)]. Various factors such as the target object size,
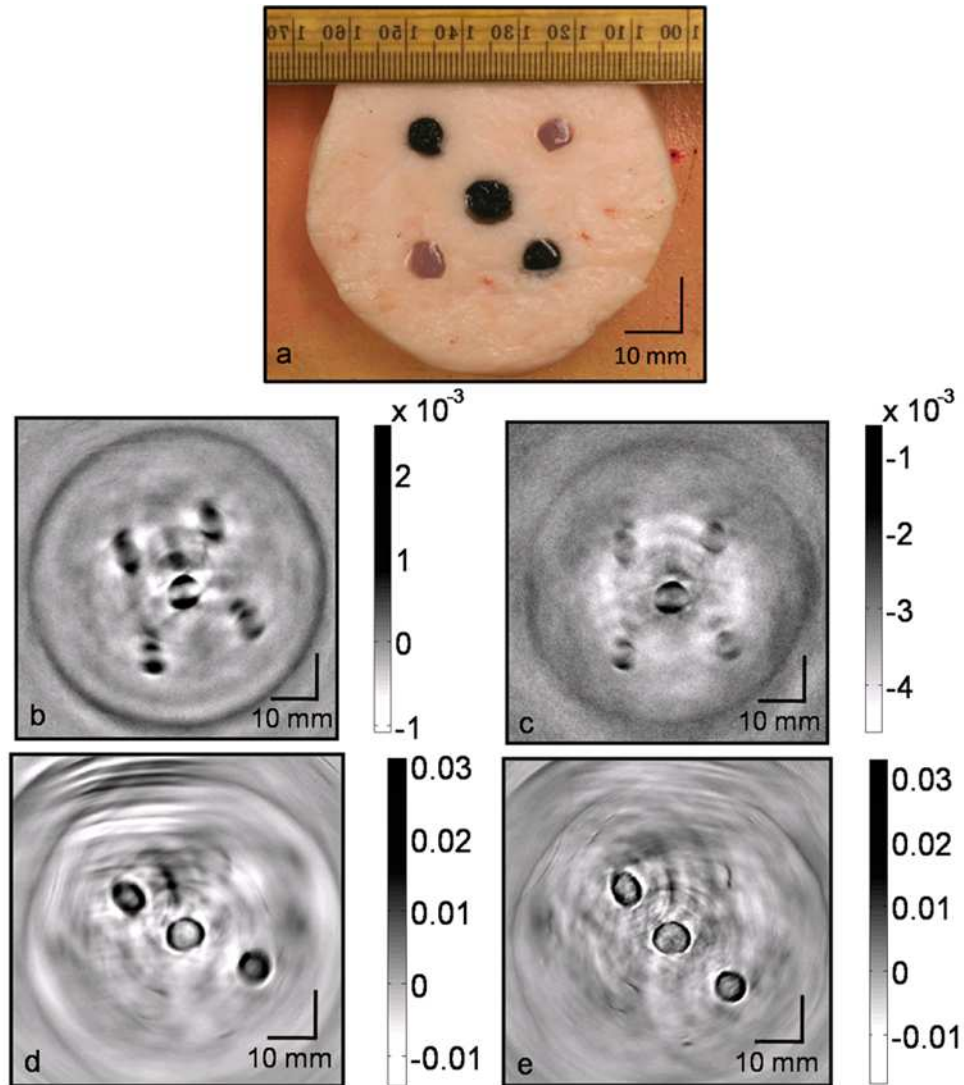
Figure 2.4: Cross-sectional TAT and PAT images of tissue mimicking phantom obtained from the scanner. Five water-based agar gel targets were embedded inside a porcine fat base. (a) Photograph of the phantom. Two targets were clear objects and the other three targets were black. (b) TAT image obtained using 13-mm-diam active area transducer. (c) TAT image obtained using 6-mm-diam active area transducer. (d) PAT image obtained at 1064 nm wavelength using a 13-mm-diam active area transducer. (e) PAT image obtained at 1064 nm wavelength using a 6-mm-diam active area transducer.

23

conductivity of the target objects, and microwave diffraction contribute to the image distortion [77]. Figures 2.4(d) and 2.4(e) show PAT images with 13- and 6-mm-diam active area transducers, respectively. The contrast and SNR in the reconstructed images are ∼4.1:1 and 64, respectively, for the 13-mm-diam transducer [Fig. 2.4(d)] and the same numbers for the 6-mm-diam transducer are ∼3.8:1 and 27, respectively [Fig. 2.4(e)]. The resolution of the images obtained by both the transducers is calculated to be ∼0.7 mm.

As expected, we can clearly see all five objects in the TAT images [Figs. 2.4(b) and 2.4(c)]. TAT is based on microwave absorption and all five objects are made of water-based gel that is much more opaque to microwave than the background fat tissue. In contrast, PAT images reveal only three black target objects as the contrast in PAT imaging is dependent on light absorption coefficient. Thus the combination of both PAT and TAT will provide us with more information about the target objects.

2.2 Tangential resolution improvement using a negative acoustic lens[†]

2.2.1 Introduction

Spatial resolution is one of the important parameters in both TAT and PAT. Figure 2.5(a) shows how radial and tangential resolutions are defined for planar circular scanning. Various factors affect the spatial resolution, but the two main limiting factors are the finite bandwidth of the ultrasound detection system and the size of the detector aperture. It was shown theoretically that both the radial and the tangential resolution are dependent on the bandwidth and that the tangential resolution is dependent on the aperture size [48]. It was also shown that the dependency of spatial resolution on bandwidth is space invariant for any recording geometry but that the dependency of tangential resolution on the detector aperture size is not space invariant. The farther the target is from the scanning center, the greater the blurring effect. In other words, the tangential resolution becomes worse as the target moves toward the detector surface.

One way of improving the tangential resolution is to use small-aperture unfocused detectors – ideally, point detectors – that can receive signals from a large angle of acceptance. However, the small active area of point detectors leads to high thermal-noise-induced electric voltage in the transducer, making the sensitivity too low to detect weak signals. Thus, we need to use large-area detectors to get better sensitivity, compromising the receiving angle. Without compromising the sensitivity of the

imaging system to a great extent, it was shown that the use of a negative cylindrical lens increases the acceptance angle and increases the detection region in PAT [78]. We extended the same concept of using a negative lens detector in our combined TAT/PAT breast scanner to quantify the tangential resolution improvement. We conducted phantom experiments for all quantitative analyses. We also showed that the use of a negative lens detector helps to preserve the shape of the target object in the reconstructed image.

In our breast scanner the cylindrical breast holder has a diameter of ∼15.5 cm, and the ultrasound detectors, placed outside the breast holder, scan around it in a full circle to collect data. The scanner is based on circular scanning mechanism and an orthogonal detection system suitable for deep tissue imaging. Due to large scanning region, the tangential resolution near the breast holder boundary (i.e., far from the scanning center) is extremely poor compared to the resolution in the vicinity of the scanning center. An ideal imaging system would have uniform radial and tangential resolution across the entire scanning region. One way of improving the near-boundary tangential resolution would be to put the detectors far from the scanning region. In doing so, the SNR would be reduced. Therefore, the negative lens detector concept was adopted, and studies were carried out to quantify the resolution of the imaging system at different locations inside the scanning region. Although a TAT/PAT combined breast scanner system was used here, the same concept can be extended to other TAT and/or PAT imaging systems where unfocused detectors are used for receiving signals.
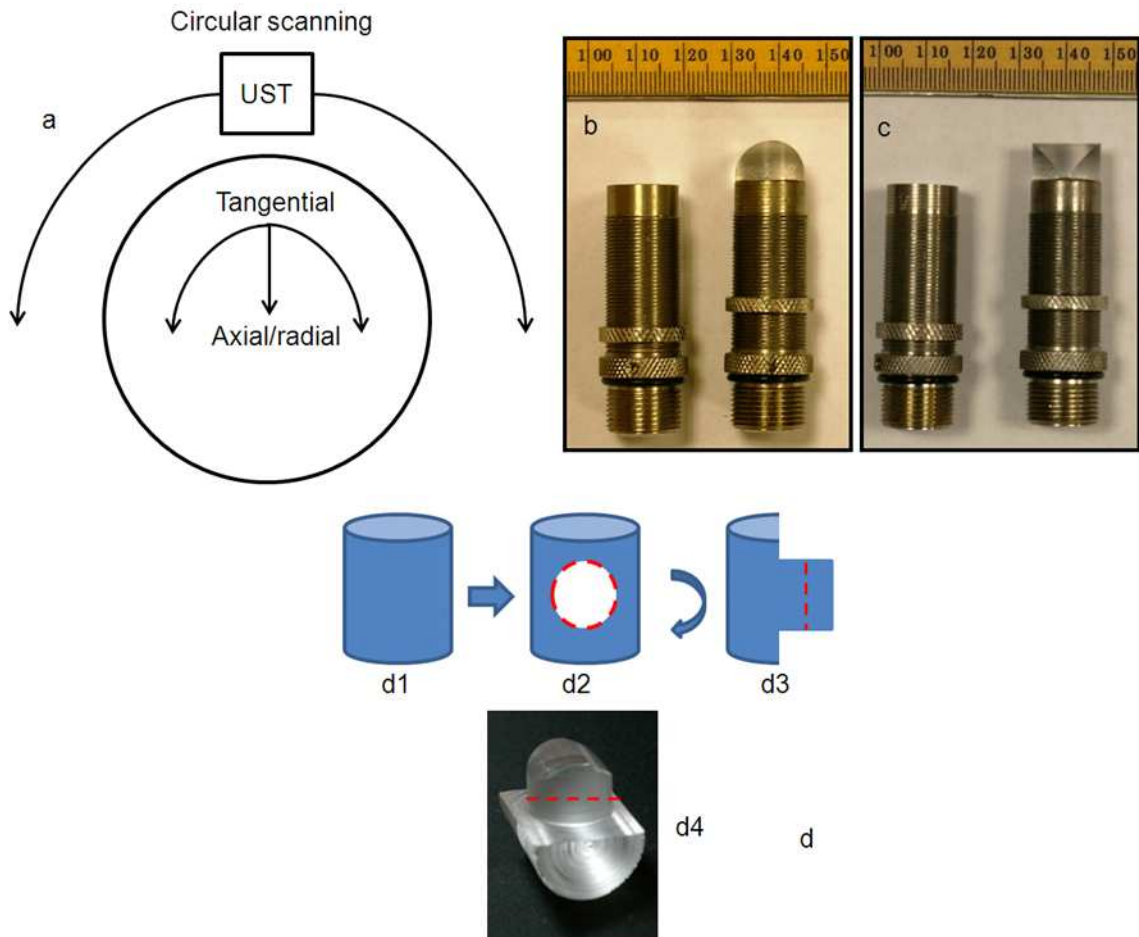
Figure 2.5: (a) Diagram showing how radial and tangential resolution is defined in planar circular scanning configuration. (b, c) Photographs of the flat ultrasonic transducer and the ultrasonic transducer glued to a negative cylindrical lens made of acrylic. The active area of the detector was completely covered by the lens. Minor ticks: 1 mm. (b) and (c) are two orthogonal views of the same transducer. (d) Step-by-step schematic of how the negative cylindrical lens is made from an acrylic cylindrical lens.

2.2.2 System description

A combined TAT/PAT scanner [53] was used for all the experiments. For TAT, a 3.0 GHz microwave source with a 0.5 μs pulse duration and 100 Hz pulse repetition rate was used. PAT was done at 532 nm wavelength. A Q-switched Nd:YAG laser with a 10 Hz pulse repetition rate, 5 ns (at 532 nm wavelength) laser pulse width, and 450 mJ maximal output energy was the light source. All other parameters used were given in detail here [53]. A modified delay-and-sum (backprojection) algorithm was used for all image reconstructions, taking into account both the dependence of time delay on the angle in the lens and also the accurate directivity factor [78].

The acoustic concave lens (negative cylindrical lens) was made of acrylic (density 1.19 g/cm^3, speed of sound 2.75 mm/μs). The lens made of a 14.5-mm-diam acrylic rod, was 8.3 mm thick. The lens was epoxied to the flat surface of the transducer. Figures 2.5(b) and 2.5(c) show the photograph of the transducers with and without the negative cylindrical lens. Once the lens was glued to the transducer, the active area of the transducer was completely covered by the lens. Figures 2.5(b) and 2.5(c) are two orthogonal views of the same transducer. Figure 2.5(d) is a schematic of how the cylindrical negative lens was made from an acrylic cylinder. Figure 2.5(d1) shows the 14.5-mm-diam acrylic cylindrical rod. Figure 2.5(d2) shows how the rod was machined to cutout a circular part (red dotted circle, this circular part has a diameter similar to that of the transducer surface). Figure 2.5(d3) shows the side view of the rod after machining. Figure 2.5(d4) is a digital photograph. The lens is cut out of the acrylic base along the red dotted line [Figs. 2.5(d3) and 2.5(d4)].
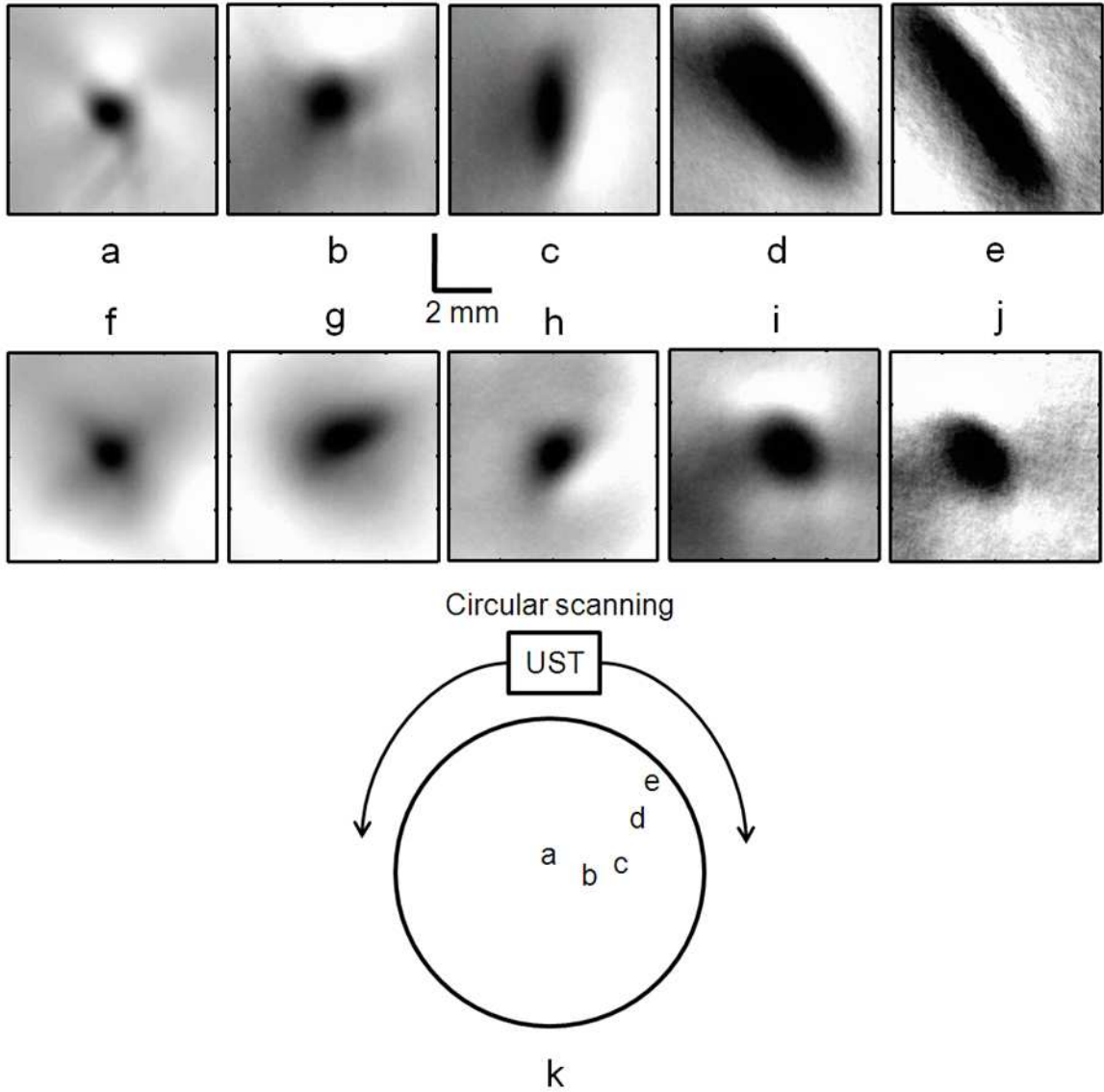
Figure 2.6: Reconstructed TAT images, using the flat ultrasonic detector, of a needle (18 gauge, 1 mm in diameter) inserted inside a pork fat base placed at a distance of (a) ∼4 mm, (b) ∼14 mm, (c) ∼32 mm, (d) ∼50 mm, and (e) ∼64 mm from the scanning center. Corresponding TAT images obtained with the negative lens detector are shown in (f), (g), (h), (i), and (j), respectively. (k) Location of the needle inside the scanner is shown.

2.2.3 Results and discussion

An 18 gauge needle (1 mm diameter) inserted inside a pork fat base was the target object for the TAT experiments. The detector was located $\sim$75 mm away from the scanning center. Considering the scanning center to be at $(0, 0)$, other object locations were as follows: Figure 2.6(a) (-1.4 mm, 4.0 mm), distance from center $\sim$4.0 mm, distance from detector $\sim$71 mm. Figure 2.6(b) (13.5 mm, 1.5 mm), distance from center $\sim$14 mm, distance from detector $\sim$61 mm. Figure 2.6(c) (32.0 mm, 2.0 mm), distance from center $\sim$32 mm, distance from detector $\sim$43 mm. Figure 2.6(d) (40.5 mm, 28.0 mm), distance from center $\sim$50 mm, distance from detector $\sim$25 mm. Figure 2.6(e) (52.5 mm, 36.5 mm), distance from center $\sim$64 mm, distance from detector $\sim$11 mm. Figures 2.6(a)–2.6(e) show the TAT reconstructed images of the needle with a flat detector when the needle was placed at different distances from the scanning center as mentioned earlier. It is evident that when the object is far from the scanning center, the object is blurred in the reconstructed image and becomes elongated in the tangential direction. Figures 2.6(f)–2.6(j) show the corresponding images when the same target was imaged with a negative lens detector. Figure 2.6(k) shows the location of the needle inside the scanning region. The radial resolution remains almost the same for all the objects at different locations, as the dependency of radial resolution on the bandwidth and aperture size is spatially invariant. Moreover, the radial resolution is not improved by the use of the negative lens. In contrast, the tangential resolution is poor when the target object is far from the scanning center [Figs. 2.6(c)–2.6(e)], and it is improved significantly with the use of the negative lens [Figs. 2.6(h)–2.6(j)]. For objects 3, 4 and 5, we see a more than twofold tangential resolution improvement [Fig. 2.6(c) versus Fig. 2.6(h), Fig. 2.6(d) versus Fig. 2.6(i), and Fig. 2.6(e) versus Fig. 2.6(j)].
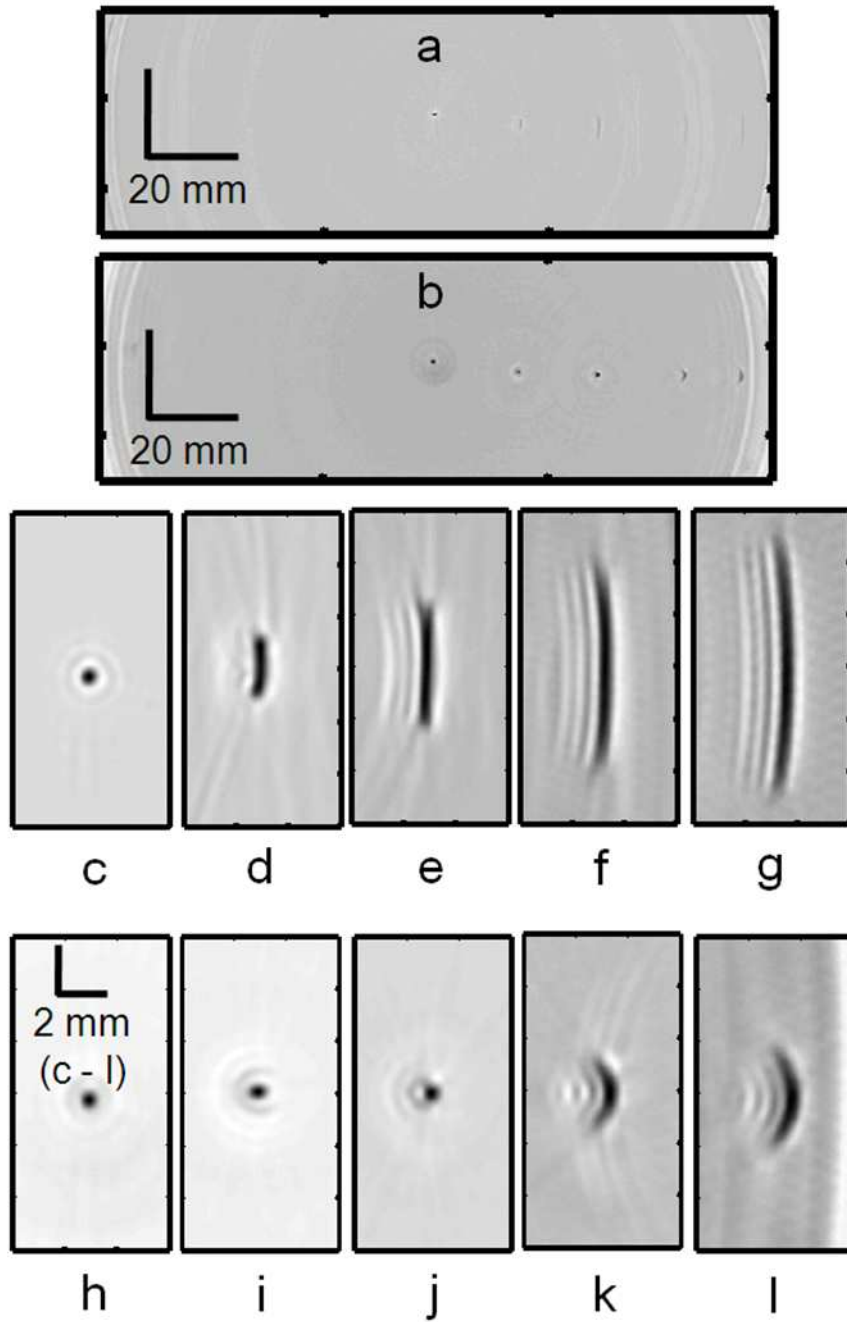
Figure 2.7: PAT images of five 0.5-mm-diam pencil leads placed inside the scanning region at different distances from the scanning center. (a) Reconstructed PAT image using the flat detector. (b) Reconstructed PAT image using the negative lens detector. (c–g) Close-up images of all five objects in (a) at distances of ∼2 mm, ∼19 mm, ∼36 mm, ∼55 mm, and ∼67 mm from the scanning center, respectively. (h–l) Corresponding close-up images obtained with the negative lens detector.

PAT experiments were done using 0.5-mm-diam pencil leads as target objects. Figures 2.7(a) and 2.7(b) show the PAT reconstructed image with the flat and negatively focused detectors, respectively, when five pencil leads were placed inside the scanner at different locations. The pencil lead locations were (−0.5 mm, 2.0 mm), (18.5 mm, −0.6 mm), (36.0 mm, −1.2 mm), (55.0 mm, −1.2 mm), and (67.5 mm, −1.4 mm). Figure 2.7(b) clearly shows all five objects (two of them near the detector surface are blurred), whereas Figure 2.7(a) fails to show the target objects except for the one near the scanning center. Figures 2.7(c)–2.7(g) show the close-up reconstructed images of each of the target objects. It is evident that when the object is far from the scanning center, the object is blurred and elongated in the tangential direction. Figures 2.7(h)–2.7(l) show the corresponding images acquired with a negative lens detector. Once again, as expected, the radial resolution is the same for all the objects (spatial invariance), and it is not improved with the use of a negative lens. But the tangential resolution has spatial dependence [Figs. 2.7(d)–2.7(g)] and it is significantly improved with the use of a negative lens [Figs. 2.7(i)–2.7(l)]. For objects 3, 4 and 5 we see a more than threefold tangential resolution improvement [Fig. 2.7(e) versus Fig. 2.7(j), Fig. 2.7(f) versus Fig. 2.7(k), and Fig. 2.7(g) versus Fig. 2.7(l)].

In the next step, we demonstrate how the type of transducer used for imaging affected the shape of the target object in the reconstructed image. To do so, an LDPE tube [∼1 cc volume, inner diameter (i.d.) ∼6 mm] filled with salt water (salt was added to increase the TAT signal strength) was placed at different locations, and TAT images were taken using both the flat and negative lens detectors. The tube locations were as follows: Figure 2.8(a) (1.0 mm, −1.5 mm); Figure 2.8(b) (17.5 mm, 15.5 mm); Figure 2.8(c) (21.0 mm, −33.0 mm); and Figure 2.8(d) (−2.0 mm, −48.5 mm). Figures 2.8(a)–2.8(d) show the TAT reconstructed cross-sectional images of the tube placed
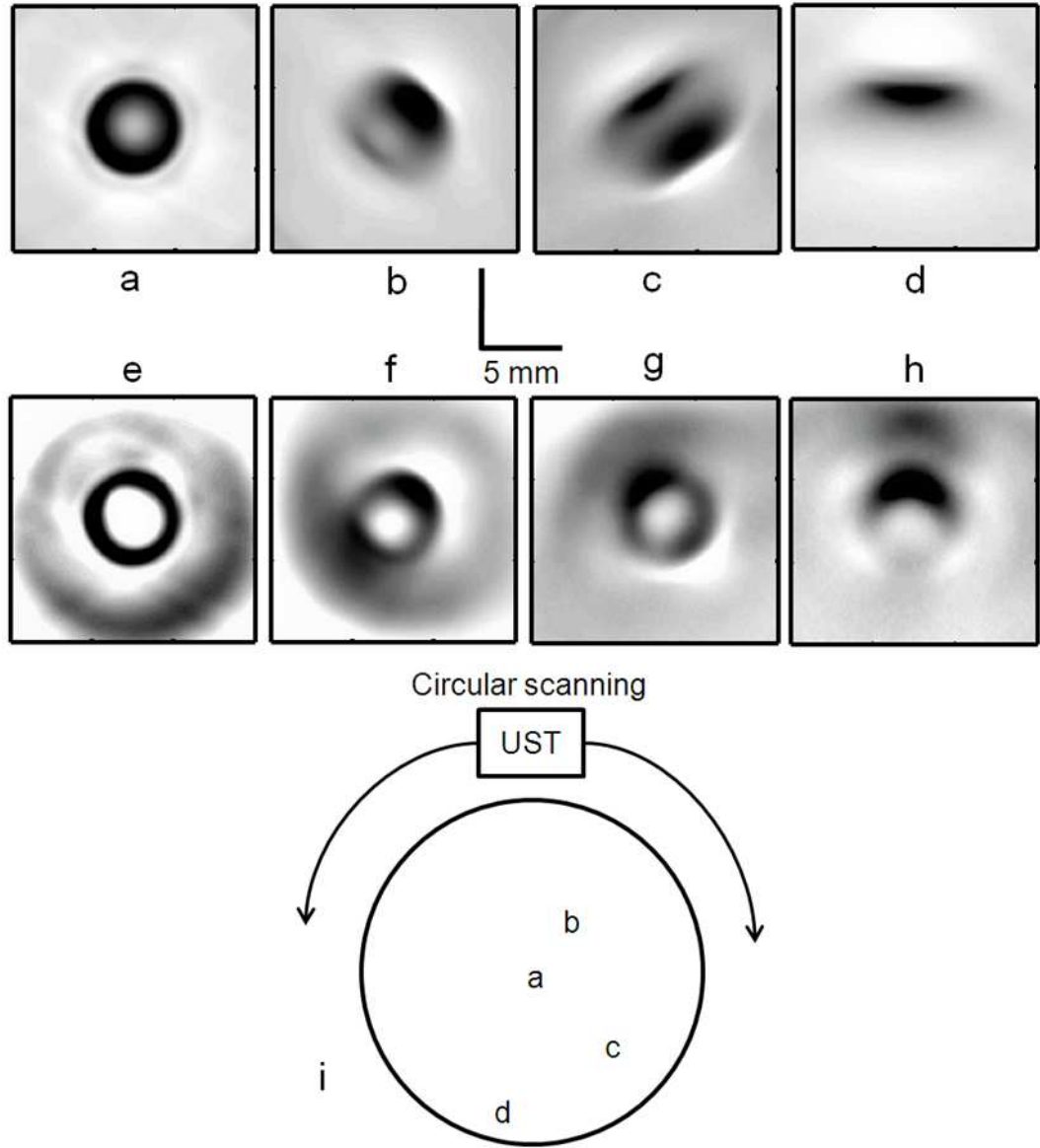
Figure 2.8: Cross-sectional TAT images, using the flat detector, of an LDPE tube filled with salt water placed at distances of (a) ~2 mm, (b) ~23 mm, (c) ~39 mm, and (d) ~49 mm from the scanning center, respectively. Corresponding TAT images obtained with the negative lens detector are shown in (e), (f), (g), and (h), respectively. (i) Location of the tube inside the scanner is shown.

at different locations in the scanning region. When the object is near the scanning center, we can clearly see the circular shape of the tube's crosssection [Fig. 2.8(a)], but when the target is located increasingly farther from the scanning center, the object loses its shape in the reconstructed image [Figs. 2.8(b)–2.8(d)]. Figures 2.8(e)–2.8(h) show the corresponding images when the negative lens detector was used to get the image. All clearly show the circular boundary of the target object, but the corresponding images acquired with the flat detector fail to do so, except for the object near the scanning center. Figure 2.8 (i) shows the location of the tube inside the scanning region.

For PAT, two LDPE tubes filled with diluted India ink solution were placed at different locations in the scanner. Figures 2.9(a) and 2.9(b) show the PAT reconstructed cross-sectional images of two tubes, one placed near the scanning center and the other placed at a distance of ∼50 mm from the scanning center, with the flat and negative lens detectors, respectively. The tube locations were (∼0, ∼0) and (0.5 mm, −49.3 mm). For the tube near the scanning center, we can clearly see the circular shape of the cross section using both detectors, but as the target object moves farther from the scanning center, it loses its shape when the flat detector was used. Figures 2.9(c) and 2.9(d) show close-up images of the tube placed at ∼50 mm from the scanning center, acquired with the flat and negative lens detectors, respectively. Figure 2.9(d) clearly shows the circular shape of the object, whereas Figure 2.9(c) fails to show the actual shape of the target object.

The artifacts seen in the images could be due to the quality of the lens fabrication and to imperfections in the glue film between the lens and the detector surface (air bubbles could be trapped in the film). A better lens quality and a bubble-free interface between the detector surface and the lens are probably the best ways to get rid of
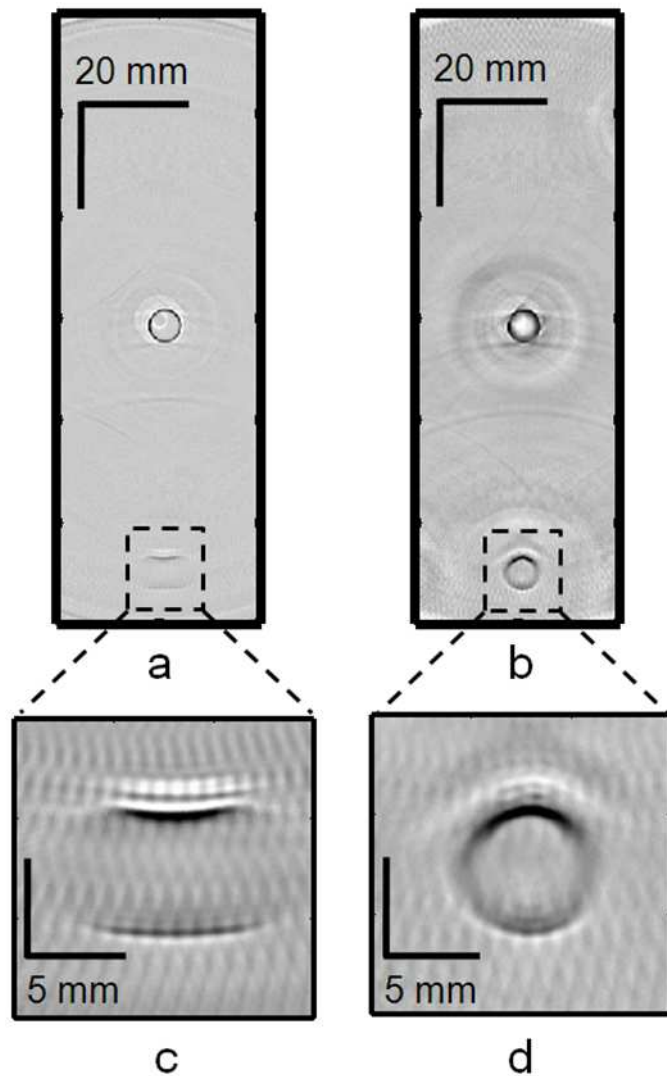
Figure 2.9: Reconstructed cross-sectional PAT images of two LDPE tubes (∼1 cc volume; i.d. ∼6 mm) filled with diluted India ink, one placed near the scanning center and the other at a distance of ∼50 mm from the scanning center. (a) Image using the flat detector. (b) Image using the negative lens detector. (c) Close-up image of the tube at ∼50 mm from the scanning center using the flat detector. (d) Close-up image of the tube at ∼50 mm from the scanning center using the negative lens detector.

the artifacts in the images. There is also a loss of signal due to the absorption of ultrasound inside the acrylic lens and another loss due to impedance mismatch between the acoustic coupling mineral oil and the acrylic lens. In addition, the reverberation of sound trapped inside the lens could also affect the reconstructed images. Some of these issues could be resolved if instead of using a negative lens we could curve the piezo material used for ultrasonic detection itself to a convex shape. In that way, we could get rid of the sound absorption inside the lens material and also the signal loss due to impedance mismatch.

2.3   Conclusions

TAT and PAT together can provide additional functional information for the diagnosis of breast cancer. We have successfully integrated the two imaging modalities into one system. Our system should be much more comfortable for the patient, and we will not need to apply gel or other chemicals on the skin: our system operates with dry coupling. We have also achieved good quality TAT and PAT images on tissue mimicking phantoms. In the future, pure ultrasound pulse-echo images can also be obtained in this modality. Thus we are able to provide multimodality, high resolution, high contrast, and low cost breast images which can be potentially used for early breast cancer detection. We also propose use of negative lens to improve the tangential resolution more than twofold in both TAT and PAT. The same concept can be extended to other tomographic imaging systems where a large imaging area is needed and flat transducers are used as detectors to receive signals. Use of negative lens also helps preserving the shape of the reconstructed object, such shape preservation could be important in accurate diagnosis and treatment of tumors.

Chapter 3

Multimodal contrast agent

3.1 Single-walled carbon nanotubes as a multimodal contrast agent[‡]

3.1.1 Introduction

The advent of numerous noninvasive imaging modalities, such as x-ray, computed tomography, single photonemission computed tomography, positron emission tomography (PET), MRI, ultrasound imaging, rf, and optical imaging now allows scientists and clinicians to acquire *in vivo* images of the anatomy and physiology of animals and humans [79, 80]. Each of these *in vivo* imaging techniques possesses characteristic strengths and weaknesses. For each imaging modality, substantial attention has been devoted to developing contrast agents not only for improving the contrast of the acquired images, but also for molecular imaging targeting specific biomolecules, cell tracking, and gene expression [81–84].

[‡]Reprinted with permission from M. Pramanik, M. Swierczewska, D. Green, B. Sitharaman, and
L. H. V. Wang,"Single-walled carbon nanotubes as a multimodal - thermoacoustic and photoacoustic
- contrast agent," Journal of Biomedical Optics 14(3), 034018 (2009).

TAT/PAT synergizes the advantages of pure-ultrasound and pure-rf/optical imaging [17, 18], allowing both satisfactory spatial resolution and high soft-tissue contrast. For instance, PAT is a unique noninvasive technology for imaging and quantifying the levels of vascularization and oxygen saturation in tumors [75, 76, 85–87]. These features are associated with angiogenesis and hypoxia accompanying malignant tumors [88, 89]. TAT/PAT is also capable of revealing information such as water/ion concentration, blood volume, and oxygenation of hemoglobin. Because these parameters can change during the early stages of cancer, TAT/PAT offers opportunities for early detection. However, even though high rf and optical contrast exists between well-developed malignant tumor tissue and normal human breast tissue, the contrast during very early stages of cancer may be insufficient. Thus, a targeted contrast agent could be greatly beneficial for early cancer diagnosis using TAT/PAT.

Recently, carbon nanotube-based contrast agents have shown promise for a variety of imaging techniques [90–93]. The strategies for development of these contrast agents have included encapsulation of medically relevant metal ions within their carbon sheath [90], external functionalization of the carbon sheath with a variety of imaging agents [92, 93], and exploiting the intrinsic physical properties of the carbon nanotubes [91]. Here, we have explored the intrinsic optical [94, 95] and rf [96] absorbing properties of single-walled carbon nanotubes (SWNTs) with the goal of developing them as multimodal contrast agents for simultaneous TAT and PAT.

3.1.2   Methods and materials

The combined TAT/PAT scanner [53] was used. For TAT, a 3.0 GHz microwave source with 100 Hz pulse repetition rate, and for PAT a Q-switched Nd:YAG laser at

1064 nm wavelength was used (See appendixC for more details). A reflection-mode PA imaging system [97] was used to test the *in vitro* blood signal enhancement using the SWNTs. A 5 MHz central frequency, spherically focused ultrasonic transducer (V308, Panametrics-NDT) was used to acquire the generated PA signals (See appendixC for more detail). See appendixA for SWNTs synthesis and characterization.

3.1.3 Results and discussion

LDPE vial with an i.d. of 6 mm and 1 cc volume was used as a sample holder. The vial was filled with the sample and placed inside the TAT/PAT scanner. Deionized water was used for TA signal comparison, whereas blood was used for PA signal comparison. Water and ions are two well-known sources of microwave absorbers in the human body, and they produce strong TA signals. Therefore, to show that a new material (in this case SWNTs) can function as a contrast agent, we have to first show that that SWNTs are capable of generating TA signals comparable to or stronger than a known TA signal producer in the body. The rf contrast between malignant tumor tissue and normal human breast tissue is as high as 4:1 [8]. The rf absorption of water compared to background human breast tissue is also on the order of 4:1. Thus, we compared the rf absorption of SWNTs to that of water. Similarly, blood is a dominant light absorber in the human body and produces strong PA signals. Therefore, to show that SWNTs can function as a contrast agent in PA, we must first show that SWNTs are capable of generating PA signals comparable to or stronger than that of a known absorber in the body. Blood was thus an obvious choice for comparison here.

Table 3.1: Peak-to-peak TA/PA signal amplitudes obtained from various samples. An LDPE (6 mm i.d., 1 cc volume) vial was the sample holder. TA was done at 3 GHz, and PA was done at 1064 nm wavelength.

	Transducer active area			
	0.5 in	0.25 in	0.5 in	0.25 in
Sample	TA signal (mV_{p-p})		PA signal (mV_{p-p})	
Deionized water	47	14	-	-
SWNTs (1 mg/mL)	**95**	**28**	**113**	**81**
Fullerene (C_{60})	51	15	55	68
Graphite microparticles	38	10	28	30
MWNTs (o.d. = 10–15 nm)	40	12	95	81
Aldrich MWNTs (o.d. = 20–30 nm)	40	12	58	67
MWNTs (o.d. = 40–70 nm)	39	10	28	27
MWNTs (o.d. = 110–170 nm)	47	15	62	70
Blood	-	-	33	31

An initial assessment was made for all the carbon nanostructures [SWNTs, multi-walled carbon nanotubes (MWNTs), C_{60}, and graphite microparticles]. Table 3.1 summarizes the peak-to-peak TA/PA signal amplitudes obtained from various samples with the two different diameter transducers. Among all the samples, only SWNTs showed a significant increase in TA signal compared to deionized water and a significant increase in PA signal compared to rat blood. To avoid overinterpretation of the data presented in Table 3.1, it is important to mention here that the TA and PA signals generated from the MWNT are not directly proportional to the outer diameter (o.d.). Other parameters, such as the inner diameter, nanotube length, and number of concentric nanotubes, may also affect the generated signal amplitudes. The only conclusion that can be drawn from Table 3.1 is that the SWNT sample generates a

PA and TA signal stronger than that from blood, water, and other carbon nanostructures. Because only SWNTs showed a significant increase in both TA and PA signals, they were used for further studies.

Figure 3.1(a) displays the TA signals from an LDPE vial filled with DI water and another vial filled with 1 mg/mL SWNTs. The peak-to-peak TA signal amplitudes generated by DI water and 1 mg/mL SWNTs are 42 ± 0.32 and 101 ± 0.24 mV, respectively. Figure 3.1(b) shows the peak-to-peak TA signal amplitude and fractional increase in TA signal versus the concentration of SWNTs. The largest standard deviation of the data points, measuring 0.92 mV, was observed at 0.75 mg/mL concentration SWNTs. The data show an approximately linear relationship between the TA signal amplitude and the SWNTs' concentration. We observe a maximum of 140% increase in the peak-to-peak signal amplitude for 1 mg/mL SWNTs over DI water. Figure 3.1(c) displays the PA signals from LDPE vial filled with blood and with 1 mg/mL SWNTs. The peak-to-peak PA signal amplitudes generated by blood, and the 1 mg/mL SWNTs are 0.22 ± 0.002 and 1.32 ± 0.009 V, respectively. Figure 3.1(d) shows the peak-to-peak PA signal amplitude and fractional increase in PA signal versus the concentration of SWNTs. The largest standard deviation of the data points, measuring 0.027 V, was again observed at 0.75 mg/mL concentration SWNTs. The data again show an approximately linear relationship between the PA signal amplitude and the SWNTs' concentration. We observe a maximum 490% increase in the peak-to-peak signal for 1 mg/mL SWNTs over blood.

In vitro tests were carried out with SWNTs (0.1 mg/mL) mixed with blood in different proportions, and then PA signals were recorded. Keeping in mind that in other applications NIR light (700–800 nm) would be used for *in vivo* deep tissue imaging, the light used here was of 754 nm wavelength in the reflection mode PA imaging
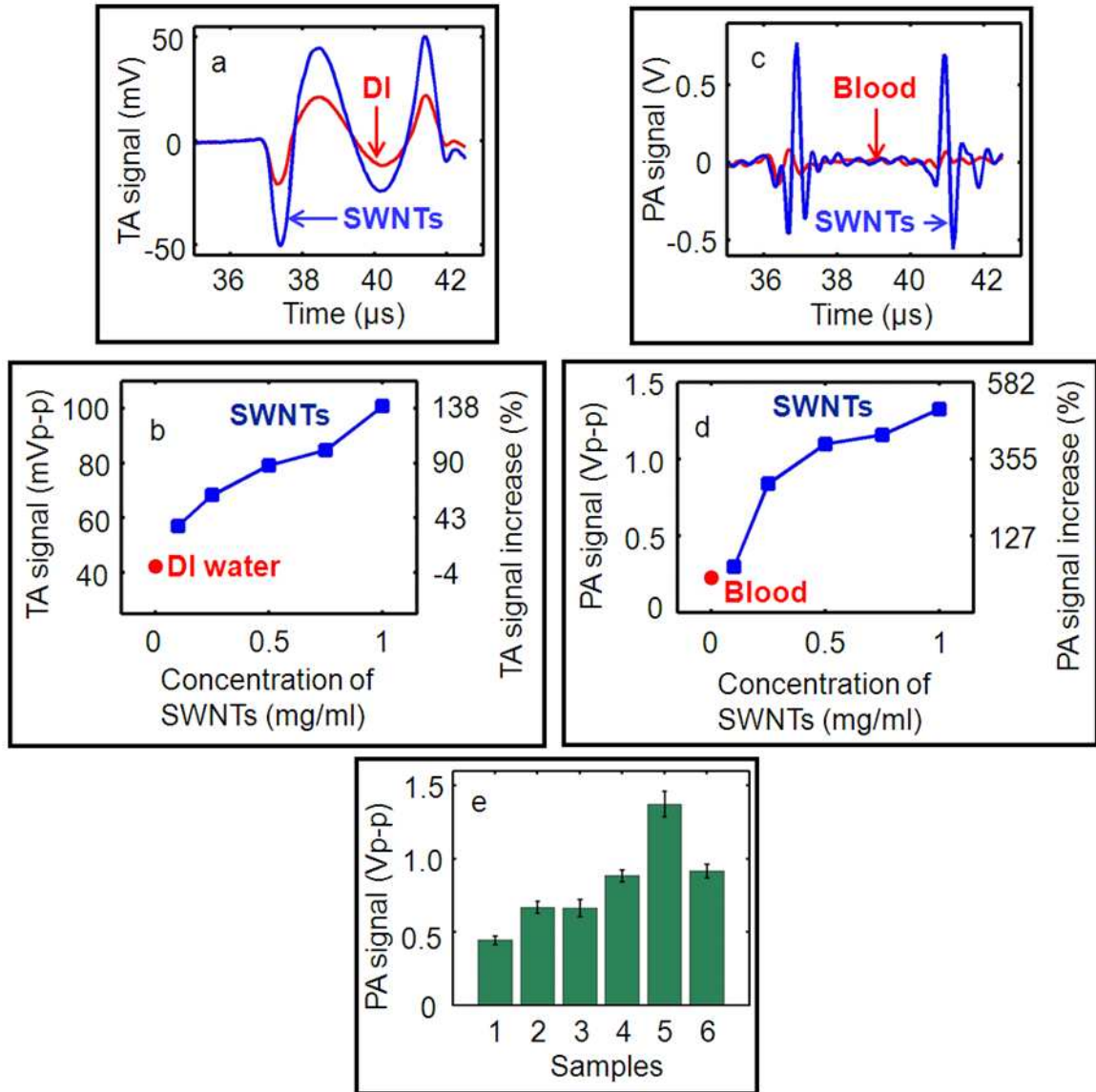
Figure 3.1: (a) TA signals at 3 GHz from a LDPE vial (i.d. 6 mm, volume 1 cc) filled with DI water and 1 mg/mL SWNTs. (b) Peak-to-peak TA signal amplitude and fractional increase in TA signal versus SWNTs concentration. (c) PA signals at 1064 nm wavelength from a LDPE vial filled with rat blood and 1 mg/mL SWNTs. (d) Peak-to-peak PA signal amplitude and fractional increase in PA signal versus SWNTs concentration. (e) Peak-to-peak PA signal amplitudes from blood mixed with various amounts of SWNTs. 1: Blood only, 2: blood (90% v/v) + SWNTs (10% v/v), 3: blood (75% v/v) + SWNTs (25% v/v), 4: blood (50% v/v) + SWNTs (50% v/v), 5: blood (25% v/v) + SWNTs (75% v/v), and 6: SWNTs alone. The light source was of 754 nm wavelength. A tube (Silastic laboratory tubing, Dow Corning Corp., with 300 μm i.d., 640 μm o.d.) was used to hold the sample.

system [97]. A tube (Silastic$^{\circledR}$ laboratory tubing, Dow Corning Corp., with 300 μm i.d. and 640 μm o.d.) was filled with blood, blood (90% v/v) + SWNTs (10% v/v), blood (75% v/v) + SWNTs (25% v/v), blood (50% v/v) + SWNTs (50% v/v), blood (25% v/v) + SWNTs (75% v/v), and SWNTs alone. Figure 3.1(e) shows the peak-to-peak PA signal amplitudes for those six samples, clearly indicating that the PA signal from blood was enhanced when SWNTs were mixed with the blood. The experiments were carried out 10 times to get the average and the standard deviation. We observed a PA signal of 1.37±0.09 V from a mixture of 75% SWNTs and 25% blood, compared to a 0.44±0.02 V PA signal from only blood. Therefore, when SWNTs were mixed with the blood, we saw a > 210% increase in the PA signal at 754 nm wavelength.

As shown in previous studies [98], the optical absorption properties of SWNTs are strong in the visible and NIR region. Currently, no studies have demonstrated SWNTs' absorption property in the 3 GHz microwave region, but their conductive properties make them promising for strong absorption [99]. SWNTs have high permittivity when exposed to electromagnetic radiation at frequencies between 0.5 and 3 GHz, and as the frequency increases to > 3 GHz, the permittivity decreases [100, 101], indicating that SWNTs could be used as contrast agents at < 3 GHz. Another study showed the feasibility of iron oxide nanoparticles as a contrast agent in TAT [102]. We successfully demonstrated that SWNTs are suitable as a contrast agent for both TAT and PAT. It will be particularly interesting to characterize their effectiveness at lower rf frequencies. It is well known that the human body becomes more transparent at lower rf frequencies, allowing an increase in the imaging depth. However, because of lower tissue absorbance at lower rf frequencies, the intrinsic image contrast suffers. Therefore, if the SWNTs work as a contrast agent at lower rf frequencies, we can potentially achieve low-background, high-sensitivity, deep-tissue imaging.

The broad absorption range of SWNTs in the visible/NIR region [99] is also bene-
ficial for optical imaging because one can use a wide range of laser wavelengths for
imaging without the need to tune the contrast agent to a particular wavelength to
optimize light absorption. In comparison, other contrast agents suitable for PAT,
such as gold nanoparticles, are tuned to a particular wavelength range and can be
used only with light within that range [65, 103]. Furthermore, our results suggest
that a minimum detectable concentration of SWNTs should be comparable to that
of gold nanoparticles [103]. Using previously derived equations [104], we have cal-
culated that carbon nanotubes of 2 nm average diameter and 1 μm average length
have $\sim 10^5$ carbon atoms, giving an average molecular weight of $\sim 10^6$ Da or g/mol
(multiply the number of carbon atoms by 12, the atomic weight of carbon). From
Figure 3.1, it is clear that the minimum detectable concentration is < 0.1 mg/mL
or 100 nM (0.1 mg mL^{-1}/10^6 g mol^{-1}, 1 M = 1 mole/Liter) SWNTs concentration,
allowing their detection in the nM range. It is also evident that even at 0.1 mg/mL
SWNTs concentration, there is a 35% increase in peak-to-peak TA signal compared
to deionized water and a 32% increase in peak-to-peak PA signal compared to blood.
In this study, we have detected signals with very high signal-to-noise ratio (SNR $>$
~ 100 in both TA and PA) at 1 mg/mL SWNT concentration, suggesting that the
minimum detectable SWNT concentration could be as low as 0.01 mg/mL or ~ 10
nM with this system, making them suitable for *in vivo* applications in various tissues.
In general, the minimum detectable concentration of an exogenous contrast agent by
PAT/TAT is dependent on many factors, such as incident light/microwave energy,
ultrasound detector sensitivity, data acquisition electronics, etc. For *in vivo* studies,
the concentration(s) of the SWNTs will depend on the specific application and the
sensitivity of the imaging system [56, 105].

The SWNTs also have a number of additional benefits. (i) Other than TAT and PAT, SWNTs can also be used as a contrast agent for other imaging modalities, such as MRI, PET, NIR optical imaging, and nuclear imaging [90–93]. Therefore, in a true sense they can work as a multi-modal contrast agent. (ii) The external carbon sheath of the SWNTs can be directly functionalized for targeting and drug delivery. This capability is not possible for other optical contrast agents, such as gold nanoparticles, where one does not functionalize the gold, but rather the capping agents or the bio-compatible coating used to stabilize and/or dispense gold nanoparticles in solution. (iii) SWNTs now offer the exciting and tantalizing prospect of achieving TAT and/or PAT molecular imaging and simultaneous therapy by NIR and rf-induced hyperther-mia. Recently, SWNTs have been shown to facilitate the NIR and rf-induced ablation of tumor cells/tissues [91, 106]. Thus, these unique features of SWNTs should allow the design of multimodal imaging and multitherapeutic approaches within a single platform.

3.2 Carbon nanotube-enhanced noninvasive sentinel lymph node mapping[§]

3.2.1 Introduction

For the majority of invasive breast cancers, the surgical removal of primary breast tumor and level I and level II axillary lymph node dissections (ALND) are widely performed [107]. However, the common side effects after ALND include upper-extremity lymphedema, arm numbness, impaired shoulder mobility, arm weakness, and infections in the breast, chest, or arm [108]. A less invasive, more accurate alternative to ALND is sentinel lymph node biopsy (SLNB). For patients with clinically node-negative breast cancer, SLNB has rapidly become the standard of care [109, 110]. The concept of a sentinel lymph node biopsy assumes that the primary draining or sentinel node will be the first to contain metastases. The hypothesis is that both the mammary gland and overlying skin share a common lymphatic pathway to the same axillary sentinel node. Therefore, intradermal injection of blue dye will lead to the accumulation of the dye in the sentinel lymph nodes [111]. In this surgery, a special blue dye and/or a radioactive substance is first injected into the breast to determine which lymph nodes are the first to receive drainage from the breast. These nodes are potentially the first to be invaded by cancer cells. One to three sentinel nodes are usually removed and tested for cancer. If cancerous, then all the lymph nodes are removed. This surgery has fewer complications than axillary node dissection, but the physicians performing the procedure must have special training. The identification

---

[§]Reprinted with permission from M. Pramanik, K. H. Song, M. Swierczewska, D. Green, B. Sitharaman, and L. H. V. Wang, "In vivo carbon nanotube-enhanced non-invasive photoacoustic mapping of the sentinel lymph node," Physics in Medicine and Biology 54(11), 3291-3301 (2009).

rate and sensitivity of this technique are less than 95%, even in experienced hands [109, 110, 112]. Furthermore, the complications associated with the SLNB procedure include seroma formation, lymphedema, sensory nerve injury, and limitation in the range of motion [113]. These limitations of SLNB strongly suggest that alternative strategies to stage the axilla should be explored.

Axillary ultrasound (AUS) has been proposed as a potential noninvasive technique for identifying axillary metastases [114–116]. AUS can visualize the lymph node's size, shape, and contour, as well as changes in cortical morphology and texture that appear to be associated with the presence of axillary metastases. However, the ability of AUS alone to stage the axilla accurately is limited because the sonographic signs of metastatic disease may overlap with those of benign reactive changes. On the other hand, *in vivo* identification of a SLN using photoacoustic imaging would allow noninvasive axillary staging, in conjunction with either percutaneous fine needle aspiration biopsy (FNAB) or other emerging molecular techniques.

In vivo PA imaging of SLN in a rat model was also reported using methylene blue [117]. However, methylene blue does not permit molecular imaging. We exploited the intrinsic optical absorbance [94, 95] of carbon nanotubes to develop them as contrast agents, and used them to perform noninvasive imaging of SLN in a rat model *in vivo*.

3.2.2 Methods and materials

A reflection-mode PA imaging system [97] was used. A 5 MHz central frequency, spherically focused ultrasonic transducer (V308, Panametrics-NDT) was used to acquire the generated PA signals (See appendixC for more detail on system description). See appendixA for SWNTs synthesis, characterization, animal and drug information.

3.2.3 Results and discussion

Deep tissue imaging: The sensitivity of the PA imaging system was determined from chicken tissue phantom experiments, used to mimic human breast tissue [117]. The light source was tuned to 793 nm wavelength. A tube (Silastic® laboratory tubing, Dow Corning Corp.) with 1.47 mm i.d. was placed between two layers of chicken breast tissue. The tube was filled with 1 mg/mL SWNTs. The thickness of the tissue layer on top of the tube was ~20 mm. Figure 3.2(a) shows the maximum amplitude projection (MAP) [38] image of the tube. The tube is clearly seen in the image, with a high contrast-to-noise ratio (CNR) of 25. Figure 3.2(b) shows the B-scan PA image [along the dotted line in Fig. 3.2(a)]. The bright spot in the B-scan represents the PA signal generated from the tube filled with SWNTs. Figure 3.2(c) shows the A-line PA signal [along the dotted line in Fig. 3.2(b)], clearly showing the strong PA signal from the tube filled with SWNTs compared to the weak signal from the surrounding chicken breast tissue. These results prove that use of SWNTs as a contrast agent enables tissue imaging more than 20 mm deep.

Sentinel lymph node imaging noninvasively in a rat *in vivo*: Adult Sprague Dawley rats with various body weights (250–350 g) were used for the experiments. A control PA image of the shaved axillary region was taken. Then, an intradermal injection of 0.075 mL of 0.5 mg/mL SWNTs was performed on the forepaw pad. Four PA images were acquired at intervals of 25–30 min after the SWNTs injection. For all the PA images, the following parameters were used: field of view (FOV) = 25 mm × 30 mm, step size along the X direction = 0.2 mm, step size along the Y direction = 0.4 mm, total scan time = ~23 min. Please note that no signal averaging was done for any of these images. The images shown here are cropped to a FOV of 16 mm × 24 mm, since the outside region was not of interest.
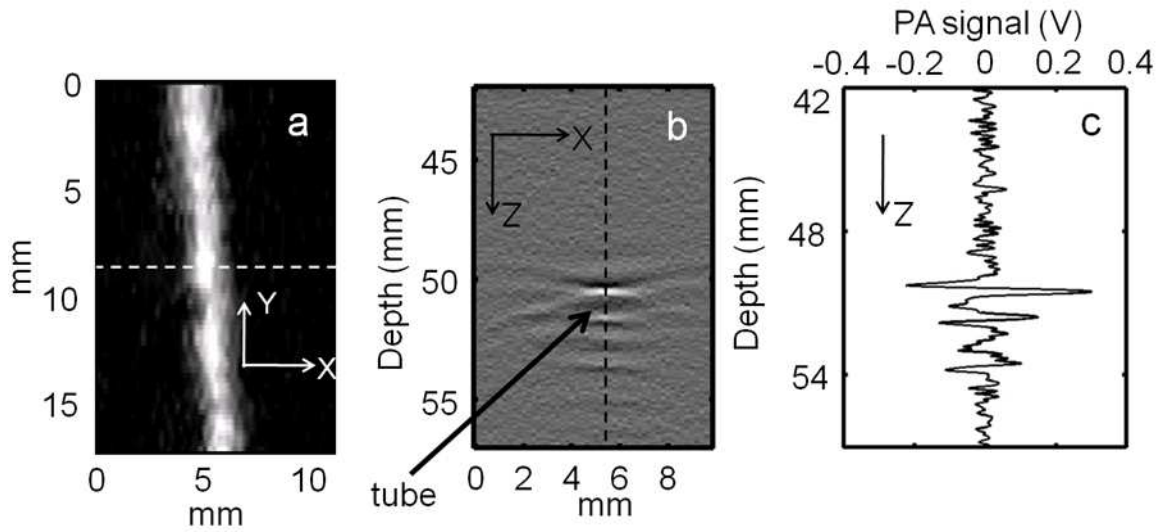
Figure 3.2: (a) MAP image of a tube (Silastic® laboratory tubing, Dow Corning Corp., with 1.47 mm i.d.) filled with SWNTs (1 mg/mL) placed inside chicken breast tissue. The tube was placed 20 mm below the top surface of the tissue. The PA image clearly shows the tube, with a CNR of 25. (b) PA B-scan image along the dotted line in (a), with the bright spot showing the PA signal originating from the tube filled with SWNTs. (c) Photoacoustic A-line along the dotted line in (b).

Figure 3.3(a) shows a representative digital photograph of a rat taken prior to image acquisition, and Figure 3.3(b) shows the shaved axillary surface where the PA imaging was performed. Before the SWNTs injection, a PA control image was obtained, which is shown in the form of a MAP [38] in Figure 3.3(c). The vasculature near an axial node (one blood vessel is marked as BV) was clearly imaged, with a high CNR of ~79 and good resolution of ~500 μm. Note that no lymph nodes are visible in the control image, since there is no intrinsic optical absorption in lymph nodes to produce any PA signal to image. Figure 3.3(d) shows the PA image (MAP) of the same area immediately after the SWNTs were injected, approximately 30 min after the control image was taken. Figures 3.3(e)–3.3(g) are the post-injection PA images (MAP) of the same area 30 min, 55 min, and 85 min after the SWNTs injection. The SLN appears at the left lower quadrant, marked as SLN in Figure 3.3(f), and is clearly
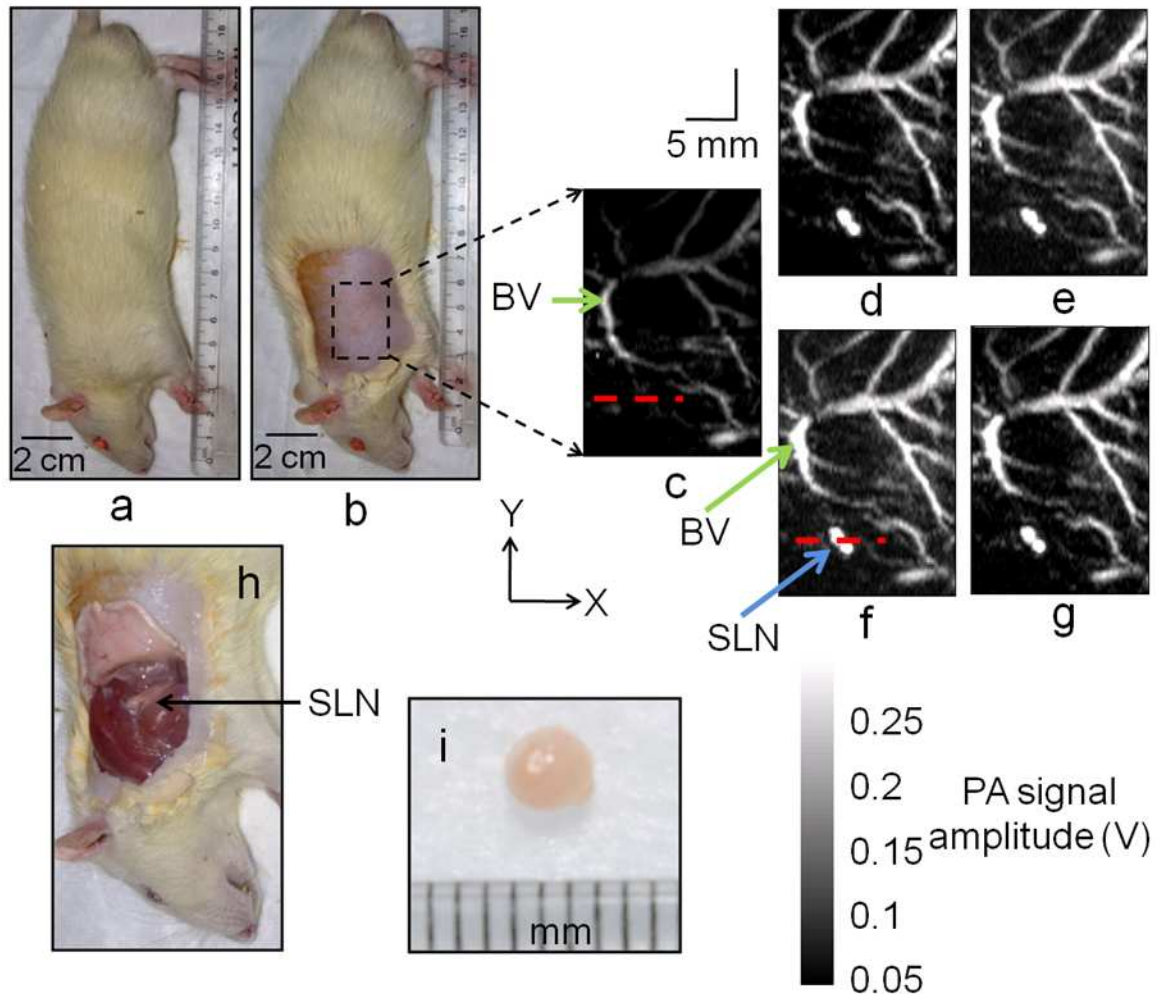
Figure 3.3: Noninvasive *in vivo* PA images (MAP) of the SLN in a rat. $\lambda = 793$ nm. (a) Photograph of the rat. (b) Photograph of the rat after the hair was removed from the scanning region before taking the PA images. The scanning region is marked with a black dotted square. (c) Control PA image acquired before SWNTs injection. Bright parts represent optical absorption, here, from blood vessels (BV). (d) PA image (MAP) acquired immediately after the SWNTs injection. (e) 30 min post-injection PA image. (f) 55 min post-injection PA image. (g) 85 min post-injection PA image. Blood vessel (BV) and sentinel lymph node (SLN) are marked with arrows, and the SLN is visible in all images except the control image. (h) Photograph of the rat with the skin removed after PA imaging. (i) The excised lymph node. For (c)–(g): FOV = 25 mm $\times$ 30 mm, step size along the X direction = 0.2 mm, step size along the Y direction = 0.4 mm, total scan time = ~23 min. No signal averaging was used. Only a FOV of 16 mm $\times$ 24 mm is shown.

visible in all the post-injection PA images [Figs. 3.3(d)–3.3(g)]. The images show high CNRs [74 in Fig. 3.3(d), 67 in Fig. 3.3(e), 84 in Fig. 3.3(f), and 89 in Fig. 3.3(g)]. The contrast of the SLN to the surrounding blood vessel was up to 1.8 (ratio of the peak-to-peak PA signal amplitude obtained from SLN and BV) after SWNTs injection. The signal amplitude of the surrounding blood vessels was also increased by up to ∼124% compared to that in the control image [94% in Fig. 3.3(d), 110% in Fig. 3.3(e), 124% in Fig. 3.3(f), and 105% in Fig. 3.3(g)], although the CNR remained almost the same. This increase in signal amplitude suggests that the SWNTs have traveled in to the blood stream and the nearby tissues boosting the blood vessel signal as well as the background signal. Figure 3.3(h) is a digital photograph of the same rat with the skin removed after the completion of the PA imaging. Figure 3.3(i) is a digital photograph of the SLN removed from the rat [arrow in Fig. 3.3(i)]. The photograph shows the SLN size to be 2 to 3 mm, matching the size obtained from PA images [Figs. 3.3(d)–3.3(g)].

We used a 0.5 mg/mL concentration of SWNTs for our *in vivo* study (the average molecular weight of SWNTs is ∼106 Da or g/mol; 0.5 mg/mL = 0.5 mg mL^{-1}/106 g mL^{-1} = 500 nM). However, that choice does not limit the use of SWNTs at other lower concentrations [105]. Currently, this imaging system is limited by its slow scanning speed. Employing a higher pulse-repetition-frequency laser and an ultrasound array system could accelerate acquisition, potentially allowing real-time PA imaging [118–120]. The *in vivo* biocompatibility of SWNTs needs to be thoroughly examined before its translation for clinical use. Nevertheless, since SLN identification by PA imaging is totally noninvasive and safe, it shows potential future clinical applications without the limitations of current invasive and minimally invasive techniques.

3.3 Conclusions

In summary, we have successfully shown that SWNTs provide more than twofold signal enhancement in TAT at 3 GHz and more than sixfold signal enhancement in PAT at 1064 nm. At lower rfs, these exogenous contrast agents offer a new paradigm for low-background, high-sensitivity, deep-tissue, and targeted molecular imaging by TAT. We have also demonstrated a noninvasive SWNTs-enhanced PA identification of SLN in a rat model *in vivo*. Our results suggest that this technology could be a useful pre-clinical and possibly clinical tool to identify SLNs noninvasively *in vivo*. In the future, the identification rate of node-negative breast cancer could be improved by functionalization of the SWNTs with targeting groups.

Chapter 4

Colloidal nanobeacons and molecular photoacoustic imaging

4.1 Molecular photoacoustic tomography with colloidal nanobeacons¶

Molecular imaging has emerged as an interdisciplinary area that shows promise in understanding the components, processes, dynamics, and therapies of a disease at a molecular level [121–127]. The unprecedented potential of nanoplatforms for early detection, diagnosis, and personalized treatment of diseases is being explored in every noninvasive biomedical imaging method [128, 129]. Despite myriad advances in the past decade, developing contrast agents with prerequisite features for these imaging modalities continues to remain a challenge.

¶Reprinted with permission from [D. Pan, M. Pramanik], A. Senpan, X. Yang, M. J. Scott, H. Zhang, P. J. Gaffney, S. A. Wickline, L. H. V. Wang, and G. M. Lanza,"Molecular Photoacoustic Tomography with Colloidal Nanobeacons," Angewandte Chemie International Edition 48(23), 4170-4173 (2009).

A number of contrast agents for PAT have been suggested recently [87, 105, 130], but only a few were shown to have the potential for targeted imaging. To achieve molecular PAT, a major and mostly uninvestigated task is to develop nanometric molecular contrast agents. The prerequisite features include improved properties, such as contrast enhancement, stability, and high target specificity.

We have prepared a novel class of accessible and commercially amenable platform technologies (Fig. 4.1). Colloidal GNBs of a "soft" nature are used to target vascular pathology, such as thrombus (fibrin), the proximate cause of stroke, and myocardial infarction. Our hypothesis is that GNBs will act as an exogenous contrast agent and could be used as a targeted molecular agent in PAT. In a typical synthesis [Fig. 4.1(a)], a commercially available octanethiol-coated gold nanoparticle (AuNP, 2 w/v%, 2–4 nm) that is soluble in organic solvents is suspended in almond oil (20 vol%) and microfluidized with phospholipid surfactants (2 vol%). The surfactant mixture is comprised of phosphatidylcholine (lecithin-egg PC, 91 mol% of lipid constitutents), cholesterol (8 mol%) and biotin-caproyl-phosphatidylethanolamine (1 mol%). This synthesis resulted in approximately 1200 biotin units per nanoparticle for biotin avidin interaction. A control nanobeacon was prepared identically except for exclusion of the gold nanoparticles.

The GNB particles have a nominal hydrodynamic diameter of 154±10 nm. The polydispersity and zeta potential were measured to be 0.08±0.03 and −47±7 mV, respectively. Gold content, determined by ICP-MS, was 1080 μg/g of the 20% colloid suspension. UV/Vis spectroscopy [Fig. 4.1(d)] showed absorptions at about 520 nm and in the NIR window, which corresponds to the presence of gold nanobeacons. The particle size and zeta potential of these nanobeacons varied less than 5% over more than 100 days when stored at 4 ^{o}C under argon in sealed serum vials (see
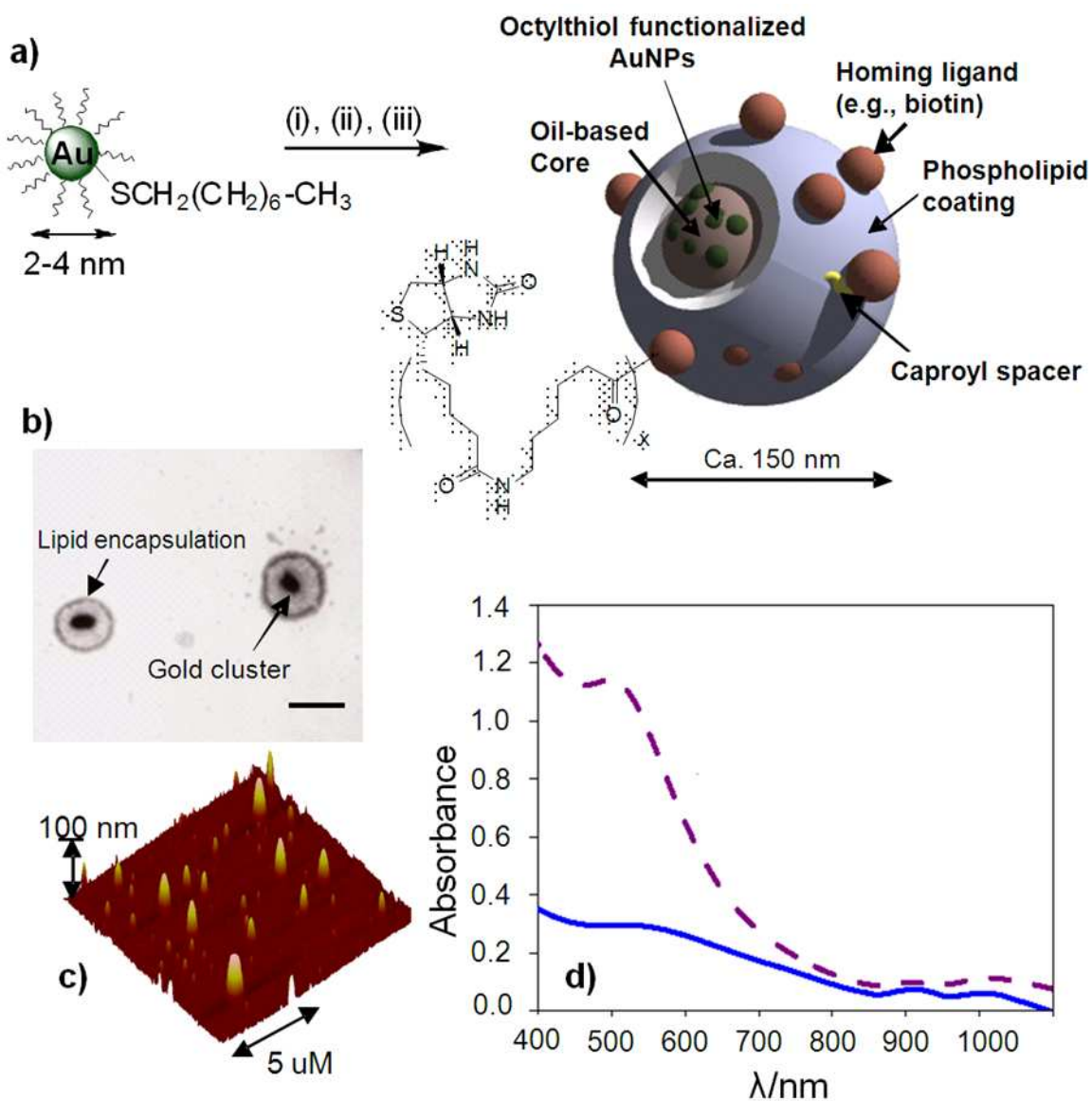
Figure 4.1: (a) Preparation of gold nanobeacons from octanethiol-functionalized gold nanoparticles (AuNPs). x = 1–2 mol% phospholipid coating. (b) Transmission electron microscopy (TEM) image of gold nanobeacons (drop deposited over nickel grid, 1% uranyl acetate; scale bar: 100 nm). (c) Atomic force microscopy (AFM) image of gold nanobeacons. Average height $H_{av}/nm = (101\pm51)$ nm. d) UV/Vis spectroscopic profile. Solid blue line: gold nanobeacons; purple dashed line: octanethiol-coated AuNPs. Spectra are not normalized.

appendixB for details). Nanocrystal platforms (< 50 nm) for NIR contrast have been reported [87, 105, 130]; however, particles in this size range rapidly distribute beyond the vasculature and into tissues where binding to non-target cells or simple matrix entrapment can lead to nonspecific signals and increased background noise. For GNBs, the tiny metallic gold nanoparticles (2–4 nm) are incorporated within a larger, vascular-constrained colloidal particle that is constrained to the circulation and intraluminal accessible biomarkers.
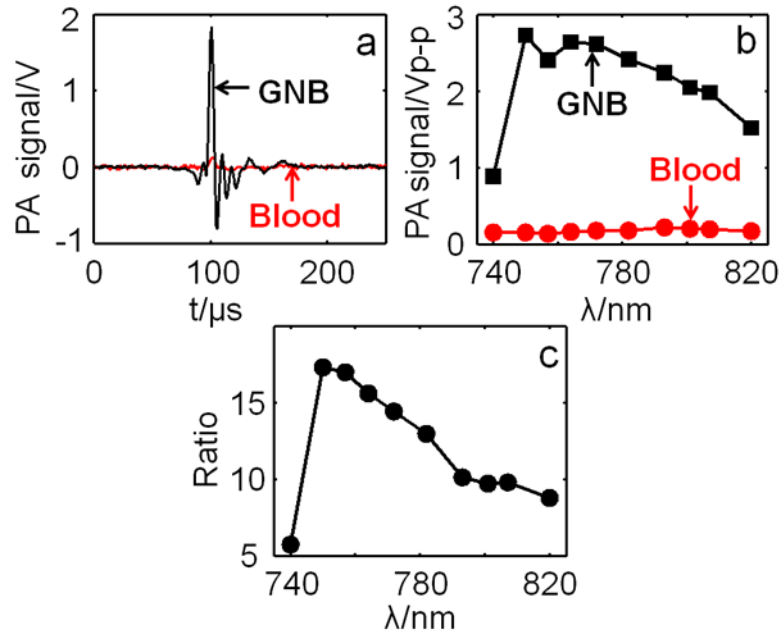
Figure 4.2: (a) PA signals generated from a tygon tube filled with GNBs and rat blood. (b) PA spectrum of GNBs and rat blood (740–820 nm range). (c) Ratio of the peak-to-peak PA signal amplitudes generated from GNBs to those of blood.

Figure 4.2(a) shows the PA signals (excitation wavelength $\lambda = 764$ nm) obtained from a tygon tube (i.d. 250 μm, o.d. 500 μm) filled with GNBs and whole rat blood. At this excitation wavelength, the peak-to-peak PA signal amplitude V_{p-p} obtained from GNBs is about 2.64 V, compared to 0.17 V peak-to-peak PA signal amplitude from rat blood. Figure 4.2(b) shows the PA spectrum of the GNBs over the NIR

wavelength range 740–820 nm. Figure 4.2(c) shows the ratio of the peak-to-peak PA signal amplitude of GNBs to that of rat blood. The PA signal from the tygon tube filled with GNBs is more than 15 times strong than that from rat blood. Over the 740–820 nm window, the PA signal from GNBs is more than ten times stronger. The NIR window is well-known for providing deep tissue PA imaging at the expense of blood contrast owing to the weak blood absorption. The strong PA signal from GNBs in the NIR region indicates the potential for molecular PAT of this platform.

The concept of molecular PAT of fibrin, a critical component of intravascular thromboses, was then studied *in vitro*. Using acellular fibrin clot phantoms, the biotinylated gold nanobeacons and the control nanobeacons (containing no metal) were targeted to the fibrin clots with classic avidinbiotin interactions using a well-characterized biotinylated anti-human fibrin-specific monoclonal antibody (NIB5F3) [131]. Figures 4.3(a) and 4.3(b) show cross-sectional PAT images of a LDPE tube (1 cc volume, i.d. 6 mm) filled with plasma clot (control) and plasma clot targeted with biotinylated GNBs using a curved array PAT system [97]. An 800 nm wavelength laser was used for the light source. The control clot treated with targeted nonmetallic nanoparticles has negligible contrast [Fig. 4.3(a)], whereas the targeted fibrin clot shows up in the PAT image [Fig. 4.3(b)] with high contrast. Figures 4.3(c) and 4.3(d) show cross-sectional PAT images, using a PA breast scanner system [53], of the same control and targeted plasma clot. For this system, a 532 nm wavelength laser source was used. As expected, the targeted plasma clot is clearly visible [Fig. 4.3(d)] in the PAT image, whereas the control image does not show any plasma clot [Fig. 4.3(c)].We have analytically tested the clot phantoms targeted with three controls for total gold content analyses. The total gold content of the clots targeted with biotinylated GNBs (with gold), non-biotinylated GNBs (with gold), and biotinylated control nanobeacons (no
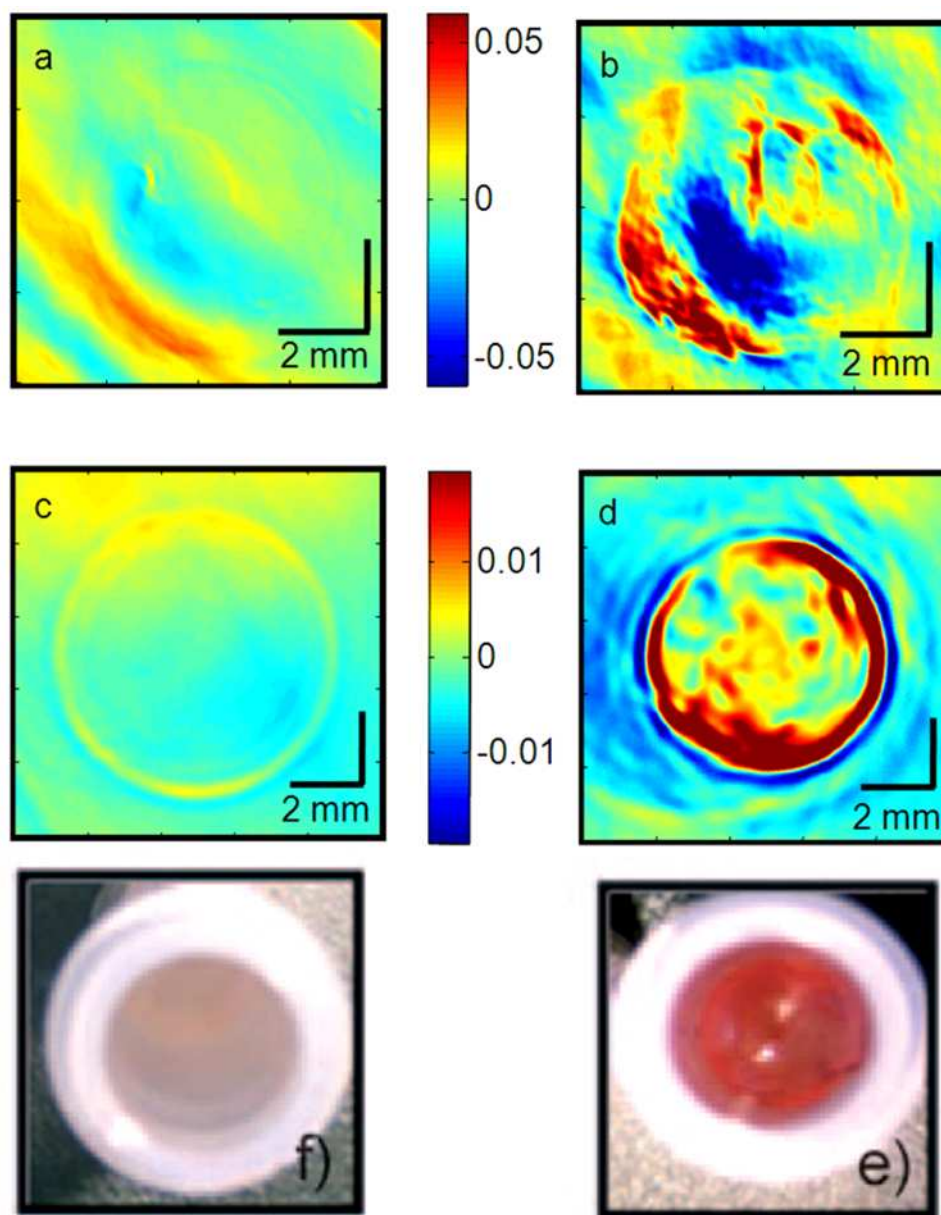
Figure 4.3: (a–d) Cross-sectional PA images of an LDPE tube filled with plasma clot. Color bars between images refer to both images. (a) control, (b) targeted with GNBs using a curved-array PA system ($\lambda = 800$ nm). (c) Control, (d) targeted with GNBs using a photoacoustic breast scanner system ($\lambda = 532$ nm). (e, f) Optical images of plasma clots stained with Biebrich scarlet acid fuchsin solution: (e) targeted with GNBs, (f) control.

gold), as determined by ICP-MS, were found to be 47 μg/g, ND (not detected, $<$ 0.02 μg/g) and ND, respectively. The *in vitro* images along with ICP-MS data of the targeted plasma clots illustrate the concept of intravascular PAT with GNBs.

Experimental section: See appendixB for GNBs preparation and characterization. Curved array photoacoustic tomographic system (See appendixC for system description) and photoacoustic breast scanner system (described in chapter 2) were used for *in vitro* imaging of the targeted plasma clot samples.

4.2 Near infrared photoacoustic detection of sentinel lymph nodes with gold nanobeacons[‖]

The success of PAT with noninvasive SLNs mapping can be considered as a giant step towards breast cancer staging. Noninvasive mapping of SLNs has been explored with PA imaging using various contrast agents, such as methylene blue dye, single-walled carbon nanotubes, gold nanocages, and gold nanorods [56, 117, 132–134]. While these approaches have seen some preliminary success in laboratory animals, it is still poorly understood how nanoparticles traverse through the lymphatic vessels and migrate into the nodes. Clearly, there is a critical unmet clinical need, and delineating this transport mechanism will further improve detection sensitivities, drug delivery efficiencies, and reduce off-target toxicity of engineered nanostructures.

Ligand-directed GNB_{160}s were found to deliver tenfold higher PA signal over blood (i.e., hemoglobin) when targeted to fibrin clots. In the first phase of our experiment, the potential of SLN imaging with GNB_{160} [D_{av}(DLS): 155±11 nm, ICP-OES: 6120 gold/nanobeacons] was tested in a rodent model. Lymph node imaging was possible with GNB_{160} (5 μM) [Figs. 4.4(a) – 4.4(e)], however with eight times diluted GNB_{160}s ($\sim$600 nM), SLNs were not visible [Figs. 4.4(f) – 4.4(j)]. The study produced mixed results with overall unsatisfactory lymph node detection sensitivity.

Our preliminary approach to resolve this issue was to increase the amount of metal within the colloidal nanobeacons. Towards this aim, we prepared polymer-encapsulated gold nanobeacons (P-GNB_{290}s) adopting a unique approach, which is based on the
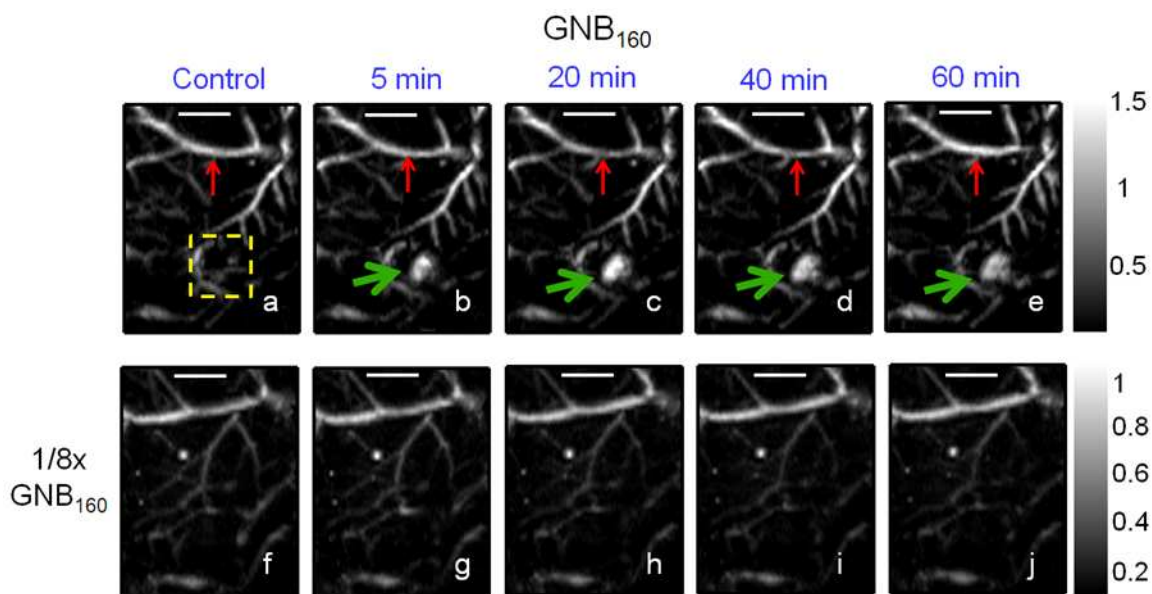
Figure 4.4: Noninvasive photoacoustic imaging of sentinel lymph nodes in rat. Scale bar: 5 mm. (a, f) Control PA images. (b–e) post-injection PA images with 5 μM GNB$_{160}$s injection. Lymph nodes are visible (marked with green arrow) in all post-injection images. (g–j) post-injection PA images with 8 times diluted (625 nM) GNB$_{160}$s injection. No lymph nodes are visible.

self-assembly of amphiphilic di-block copolymer in aqueous media to entrap high payloads of gold. In a typical synthesis, PS-b-PAA [135–138] (Mn $\times$ 10^{-3}: 0.8-b-29.3, PDI = 1.18, 0.0033 mmoles) was dissolved in a mixture of methanol and CHCl$_3$ (4:1) and subjected to controlled evaporation under reduced pressure to generate a thin film of polymer [Fig. 4.5(a)]. The thin film was dispersed in deionized water (0.2 μM) by probe sonication at ambient temperature. Octanethiol coated AuNPs (2 w/v%) were suspended in polysorbate (sorbitan monolaurate (5 vol%) and microfluidized with a PS-b-PAA dispersion (0.5 vol%) to obtain the P-GNB$_{290}$ particles. The nanobeacons were purified by exhaustive dialysis against an infinite sink of nanopure water using a cellulosic dialysis membrane (20 kDa MWCO). P-GNB$_{290}$ was characterized by multiple techniques. Hydrodynamic particle sizes for the P-GNB$_{290}$ were
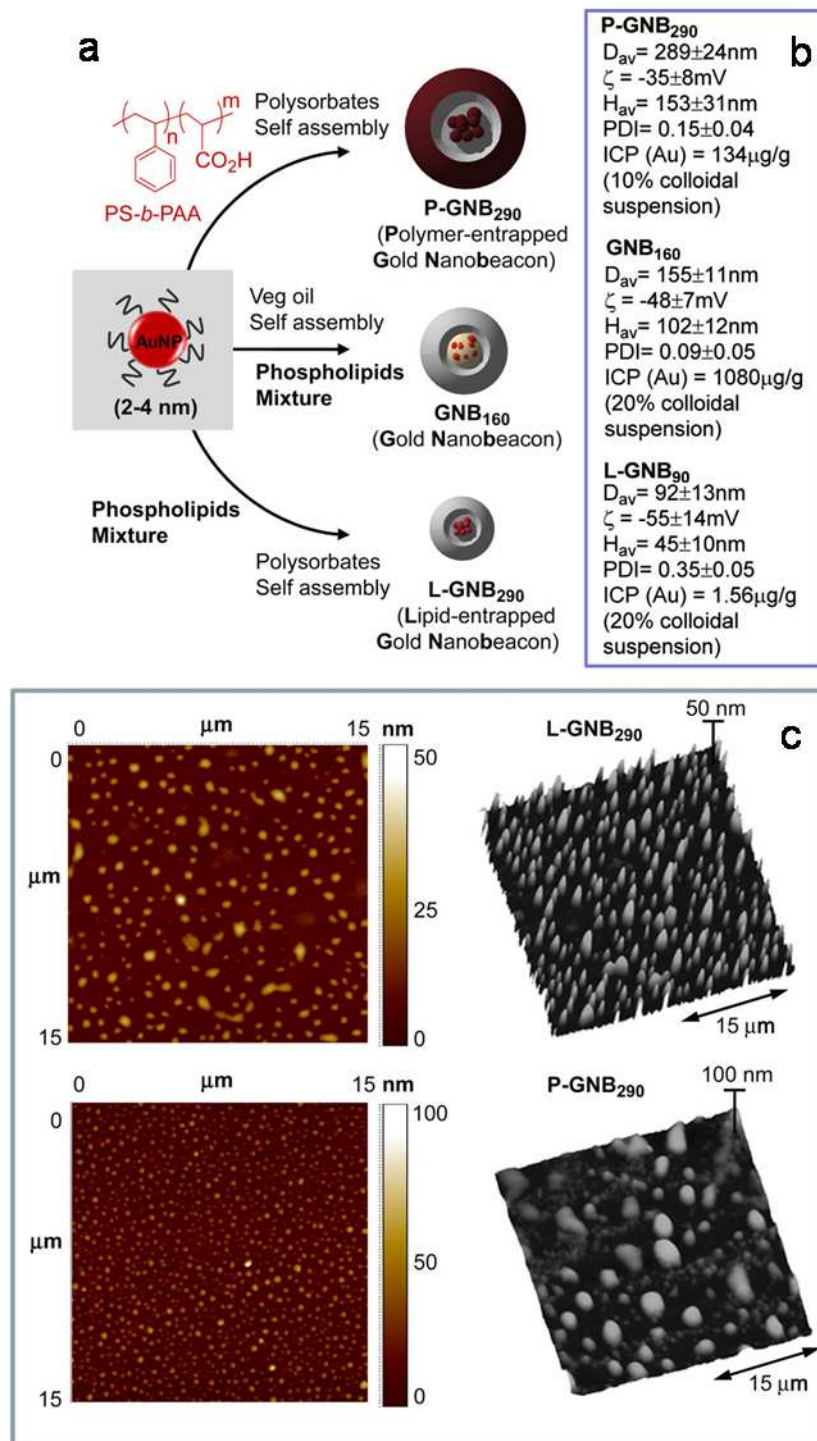
Figure 4.5: (a) Synthesis of GNBs, (b) physico-chemical characterization, (c) anhydrous state AFM images (drop-deposited on glass).

289±24 nm observed by dynamic light scattering measurements with narrow distribution (polydispersity indexes, PDI = 0.15±0.04) [Fig. 4.5(b)]. The particle stability and successful amphiline-encapsulation were confirmed by the presence of negative electrophoretic potential (ζ) values. Anhydrous state morphology of the particles was observed by atomic force microscopy studies [Fig. 4.5(c)]. Gold content was determined by ICP-OES as 134 μg g^{-1}, which corresponds to 71,493 gold metal atoms per nanobeacon.
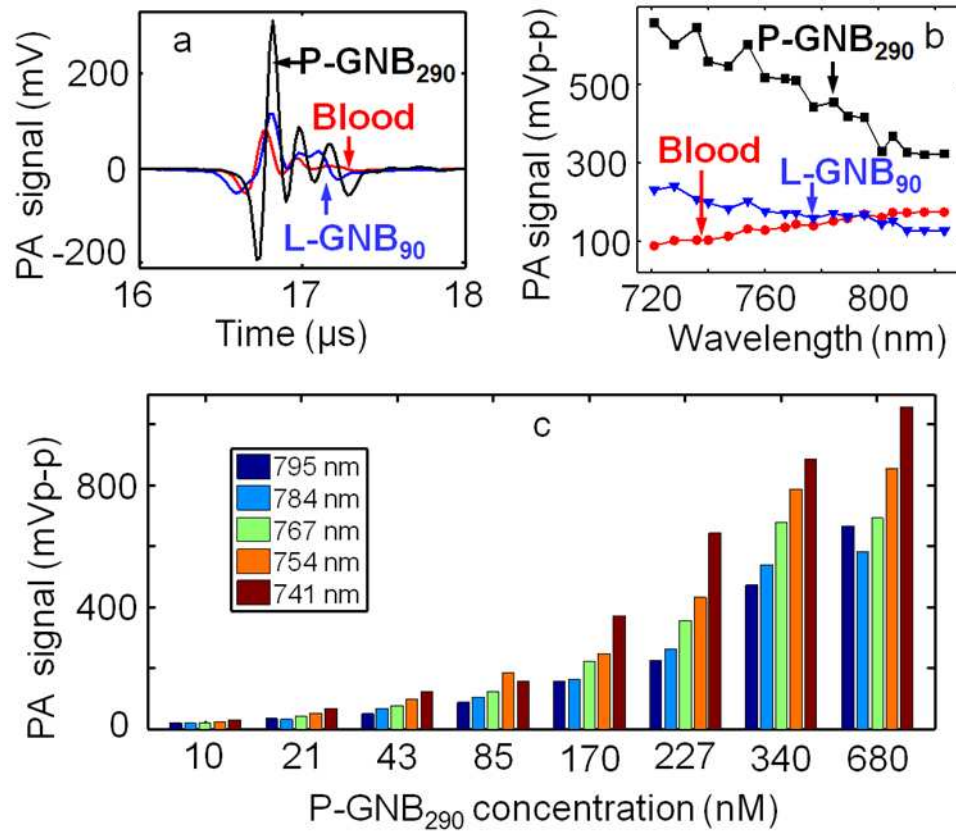
Figure 4.6: (a) PA signals generated from a tube (Silastic$^{\circledR}$ laboratory tubing, Dow Corning Corp., i.d. 300 μm, o.d. 640 μm) filled with P-GNB$_{290}$s (680 nM), L-GNB$_{90}$s (10 nM), and blood at $\lambda = 767$ nm. (b) PA spectrum of P-GNB$_{290}$s, L-GNB$_{90}$s, and blood. (c) PA signal of serially diluted P-GNB$_{290}$s at various wavelengths.

Photoacoustic imaging of P-GNB$_{290}$ in suspension within the NIR range was promising. Figure 4.6(a) shows P-GNB$_{290}$ (680 nM) produced a stronger PA signal than blood ($\lambda = 767$ nm). P-GNB$_{290}$s produced a peak-to-peak PA signal amplitude of 540 ± 30 mV, whereas blood produced 133 ± 7 mV. Figure 4.6(b) shows the PA spectrum over NIR wavelengths from 721 to 823 nm. The PA signal amplitude changed as the concentration of nanobeacons was varied. Figure 4.6(c) shows how the PA signal amplitude changed for several laser wavelengths from serially diluted P-GNB$_{290}$s. It is evident that a significant PA signal was produced even at the low concentration of 10 nM, making P-GNB$_{290}$s a candidate for *in vivo* applications.
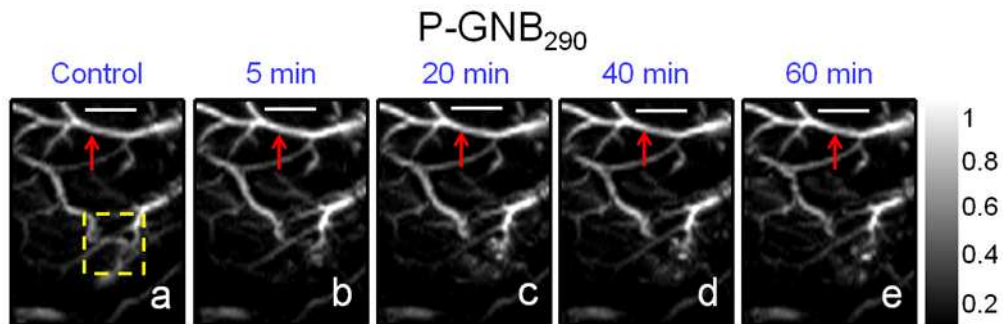
Figure 4.7: Scale bar: 5 mm. (a) Control PA image. (b–e) Post-injection PA image with P-GNB$_{290}$s (680 nM) injection. No lymph node was visible in any of the images. Due to the large particle size of the P-GNB$_{290}$s the uptake of the particles in the lymph node was none.

The potential of SLN imaging with the use of P-GNB$_{290}$s was explored through forepaw injection in a rat model. Interestingly, SLN imaging with P-GNB$_{290}$s (680 nM) was unsuccessful. Figures 4.7(a) and 4.7(e) show the pre- (control) and post-injection (60 min) MAP [38] photoacoustic images. SLNs were dynamically monitored for three days without promising results (n = 4). This confirmed that we were not experiencing a slower, longer-lasting transport of these larger nanobeacons into the lymphatic vessels. These results led us to believe that the uptake of the P-GNB$_{290}$s in the

64

lymphatic channels and transport to the lymph node were poor, which presumembly were correlated with the larger size and mass of these gold nanobeacons (> 250 nm).

The unsuccessful outcome prompted us to explore a smaller lipid-encapsulated ($\sim$90 nm) gold nanobeacon (L-GNB$_{90}$) [Fig. 4.5(a)]. Gold nanoparticles (AuNPs) were uniquely suspended within a polysorbate core matrix to avoid unfavorable interactions with the surrounding plasma proteins. In a typical procedure, octanethiol-functionalized, coated AuNPs (2 w/v% of inner matrix) were suspended in polysorbate (sorbitan monolaureate, 20 vol%) and homogenized with the surfactant mixture at 137.9 MPa for 4 min to produce L-GNB$_{90}$s. The surfactant mixture comprised mainly of phosphatidylcholine (PC) ($\sim$90 mol% of lipid constituents). Hydrodynamic particle sizes for the L-GNB$_{90}$s were 92 $\pm$12 nm (DLS) with narrow polydispersity indexes, PDI $= 0.35\pm0.05$ [Fig. 4.5(b)]. Anhydrous state particle heights were measured to be 45$\pm$10 nm. [Fig. 4.5(c)] Gold content was determined by ICP-OES as 1.56 μg g^{-1}, corresponding to approximately 9 gold metal nanoparticles per L-GNB$_{90}$s.

Figure 4.6(a) shows that L-GNB$_{90}$s (10 nM) produced a stronger PA signal than blood ($\lambda = 767$ nm). L-GNB$_{90}$s produced a peak-to-peak PA signal amplitude of 168$\pm$12 mV. Interestingly, L-GNB$_{90}$s produced a stronger PA signal than blood below 795 nm wavelength but a weaker one above 800 nm. L-GNB$_{90}$s produced weaker PA signals in suspension than P-GNB$_{290}$s, presumably due to its incorporation of much lower concentrations of gold. Although L-GNB$_{90}$s have a weaker absorption coefficient than P-GNB$_{290}$s in the NIR wavelength range, they were still considered useful for *in vivo* SLN imaging application.

The efficacy of L-GNB$_{90}$s for SLN imaging was studied in a rat model following intradermal injection of the particles, as used previously. At baseline, sagittal MAP
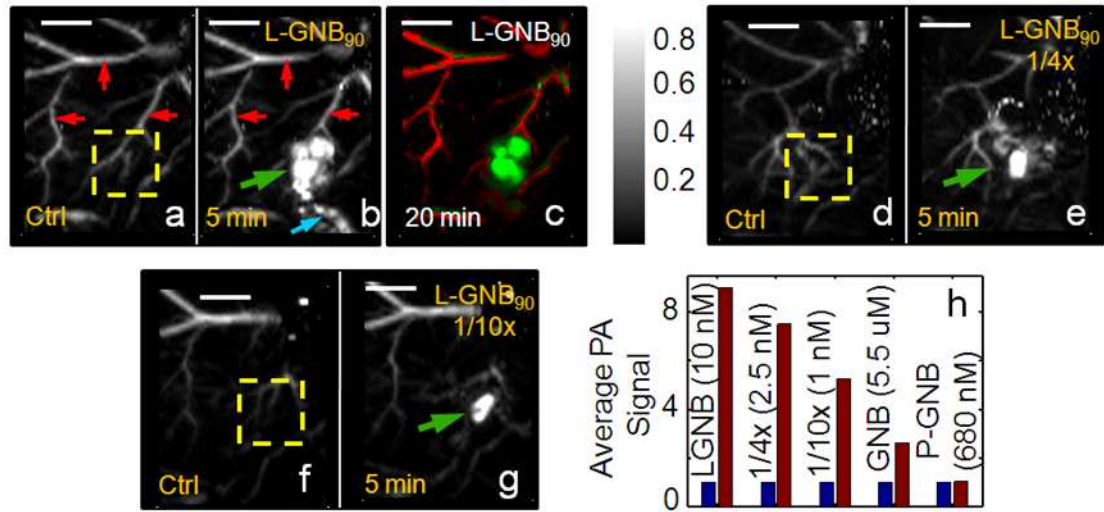
Figure 4.8: **L-GNB$_{90}$ (10 nM):** (a) Sagittal MAP [38] pre-injection control image. Bright parts represent optical absorption from blood vessels, marked with red arrows. (b) PA image (MAP) acquired 5 min after L-GNB$_{90}$ injection. SLNs are clearly visible, marked with green arrow. Lymphatic vessel is also visible, marked with blue arrow. (c) 20 min post-injection PA image with two different color spaces showing the blood vessel as well as the SLNs. (d) Control PA image. (e) 5 min post-injection image of 4 times diluted L-GNB$_{90}$s (2.5 nM). (f) Control PA image. (g) 5 min post-injection image of 10 times diluted L-GNB$_{90}$s (1 nM). (h) Average PA signal from the ROI [marked as yellow dotted square in all the pre-injection or control images, 4.4(a), 4.7(a), 4.8(a), 4.8(d), 4.8(f)]. Blue represents pre-injection and brown represents post-injection.

photoacoustic image (resolution = $\sim$500 μm, in plane) of the axillary area revealed a distinct microvasculature indicated by the red arrows [Fig. 4.8(a)]. Lymph nodes were undetectable at baseline, lacking any intrinsic optical absorbers, in contradistinction to the adjacent blood vessels containing highly absorbing red blood cells. Following baseline image acquisition, L-GNB$_{90}$s (150 μL) were injected intradermally into the forepaw, and serial PA images were acquired. At 5 and 20 mins post-injection, sentinel lymphnodes were easily visualized [Fig. 4.8(b) and 4.8(c)]. In Figure 4.8(b), immediately after the injection, L-GNB$_{90}$s were noted traveling through the lymphatic system (designated by the blue arrow) and accumulating in the lymphnodes. At 20 min, the L-GNB$_{90}$s had reached the SLNs and were no longer observed within the draining

lymphatic vessel. Dynamic PA imaging was performed up to 1 hour post-injection, and SLNs remained visible in all the PA images (see appendixB for more details). The above experiment was successfully repeated with diluted L-GNB$_{90}$s (2.5 and 1 nM). In both cases, lymph nodes were clearly visible [Figs. 4.8(d–e) and 4.4(f–g)] in the post-injection (5 min) MAP photoacoustic image.

The blood vessels and the SLN were detected with a contrast of 12 and 89, respectively (calculated from the 1 hour post-injection MAP image). The contrast is defined as the ratio of the average PA signal amplitude obtained from the blood vessel/SLN to the average background signal amplitude. Thus the contrast ratio between the SLN and the surrounding blood vessel was $\sim$7.5:1. The SNR was 24 dB and 39 dB for blood vessels and SLN, respectively. The SNR, calculated from the raw A-line signal without any signal averaging, was defined as $20\times$log (peak signal amplitude/standard deviation of background). Figure 4.8(c) is illustrated with two different color maps (green for the contribution from the nanobeacons, red for hemoglobin). Some of the nanobeacons transited into the surrounding vessels, as evident from the signal therein. The dissection of the lymph node, after all the imaging was completed, revealed no outwardly visible accumulation of the AuNP themselves (i.e., red color) indicating the patent integrity of the surface lipid coating (see appendixB for more details). We quantified the signal intensities [Fig. 4.8(h)] and observed a $\sim$9 times enhancement with L-GNB$_{90}$s injection, $\sim$7.5 times enhancement with 1/4x diluted L-GNB$_{90}$s, $\sim$5.2 times enhancement with 1/10x diluted L-GNB$_{90}$s, and $\sim$2.6 times enhancement with GNB$_{160}$s. However, with L-GNB$_{90}$s no signal enhancement was seen after injection (average signal is $\sim$1.01 times the pre-injection value). As a result, we concluded that SLNs mapping with P-GNB$_{290}$s was infeasible. The total gold content of the excised lymphnode specimens were analytically determined by ICP-OES as 8.74 μg/g and

1.99 μg/g, (detection limit = 0.02 μg/g), for animals injected with L-GNB$_{90}$s and P-GNB$_{290}$s respectively.

Experimental section: Refer to appendixB for GNB preparation, characterization and appendixC for system description (All SLN images were obtained using reflection-mode deep photoacoustic imaging system with 5 MHz center frequency transducer).

4.3   Conclusions

In summary, both GNB$_{160}$s and L-GNB$_{90}$s can function as contrast agents for PA deep tissue imaging in the NIR window, with the smaller L-GNB$_{90}$s being superior for SLNs detection. Although L-GNB$_{90}$s had lower PAT contrast in suspension, *in vitro* than GNB$_{160}$s or P-GNB$_{290}$s, when injected intradermally L-GNB$_{90}$s travel quickly through the lymphatic vessels and migrate exclusively to the lymph nodes. P-GNB$_{290}$s produced strong PA signals in suspension and therefore could be beneficial for other *in vivo* application. These results suggest that cumulative nanoparticle deposition in lymph nodes is size dependent and that high payloads of gold, although offering greater contrast, may yield nanoagents with poor intradermal migration and lymphatic transport characteristics.

Chapter 5

A novel temperature sensing method**

5.1   Introduction

During thermotherapy or cryotherapy, it is necessary to monitor the temperature distribution in the tissues for the safe deposition of heat energy in the surrounding healthy tissue and efficient destruction of tumor and abnormal cells. To this end, real-time temperature monitoring with high spatial resolution ($\sim$1 mm) and high temperature sensitivity (1 ^{o}C or better) is needed [139]. The most accurate temperature monitoring is by directly measuring the temperature with a thermocouple or thermistor. However, it is invasive, hence, generally not preferred and often not feasible. Several noninvasive temperature monitoring methods have been developed. Infrared thermography is a real-time method with 0.1 ^{o}C accuracy but is limited only to superficial temperature [140]. Ultrasound can be applied for real-time temperature measurements with good spatial resolution and a higher penetration depth, but

---

**Reprinted with permission from M. Pramanik, and L. H. V. Wang, "Thermoacoustic and photoacoustic sensing of temperature," Journal of Biomedical Optics, 14(5), 054024 (2009).

the temperature sensitivity is low [141–143]. Magnetic resonance imaging has the advantages of high resolution and sensitivity, but it is expensive, bulky, and slow [144, 145]. Therefore, an accurate, noninvasive, real-time temperature measurement method needs to be developed.

The TA and PA effects are based on the generation of pressure waves on absorption of microwave and light energy, respectively. A short microwave and laser pulse is usually used to irradiate the tissue. If thermal confinement and stress confinement conditions are met, then pressure waves are generated efficiently. The pressure rise of the generated acoustic wave is proportional to a dimensionless parameter called the Grueneisen parameter, and to the local fluence. The local fluence depends on the tissue parameters, such as the absorption coefficient, scattering coefficient, and anisotropy factor, and does not change significantly with temperature. However, the Grueneisen parameter, which depends on the isothermal compressibility, the thermal coefficient of volume expansion, the mass density, and the specific heat capacity at constant volume of the tissue, changes significantly with temperature. Thus, the generated TA/PA signal amplitude changes with temperature. By monitoring the change in the TA/PA signal amplitude, we were able to monitor the change in temperature of the object.

PA sensing has been used to monitor tissue temperature [139, 146–150]. However, TA sensing of temperature has never been studied. These two techniques do not interact and can be used independently. Depending on the need, one has to choose which technique to use. The main difference between these two techniques is the contrast mechanism. For example, water and ion concentrations are the main sources of contrast in TA measurements, whereas blood and melanin are the main sources of contrast in PA measurements. Therefore, if we need to monitor the temperature

of a blood vessel, then the PA technique will be more useful; whereas if we need to monitor the temperature of muscles, then the TA technique will be preferred. TA/PA temperature sensing is a noninvasive, real-time method. The TA/PA technique has the ability to image deeply (up to 5 cm) with high spatial resolution (scalable: millimeters to microns). We can monitor temperature with high temporal sensitivity ($\sim$2 sec) and high temperature sensitivity (0.15 ^{o}C) and high precision [scalable with temporal resolution: $\pm$0.015 and $\pm$0.15 ^{o}C at 200 s (2000 measurements averaged) and 2 s (20 measurements averaged) resolutions, respectively]. Because microwaves penetrate more deeply into tissue than light, we can potentially monitor temperature *in vivo* for locations deep inside the body.

5.2   Theoretical background

If the microwave/laser excitation is much shorter than both the thermal diffusion (thermal confinement) and the pressure propagation (stress confinement) in a heated region, the fractional volume expansion dV/V can be expressed as

$$dV/V = -\kappa p + \beta T, \qquad (5.1)$$

where κ is the isothermal compressibility, β is the thermal coefficient of volume expansion, and p and T denote changes in pressure (Pascal), and temperature (Kelvin), respectively.

When the fractional change in volume is negligible under rapid heating, the local pressure rise immediately after the microwave/laser excitation pulse can be derived as,

$$p_0 = \frac{\beta T}{\kappa} = \frac{\beta}{\kappa \rho C_v} \eta_{th} A_e, \tag{5.2}$$

where ρ denotes mass density, C_v denotes specific heat capacity at constant volume, A_e is the specific optical/microwave absorption, and η_{th} is the percentage of absorbed energy that is converted to heat.

We define the Grueneisen parameter (dimensionless) as

$$\Gamma = \frac{\beta}{\kappa \rho C_v} = \frac{\beta V_s^2}{C_p} = f(T), \tag{5.3}$$

where V_s is the velocity of sound, C_p denotes the specific heat capacity at constant pressure, and T is the temperature of the object.

Therefore,

$$p_0 = f(T) \eta_{th} A_e, \tag{5.4}$$

Thus, in practice, the measured pressure signal generated due to the microwave/laser excitation can be used to monitor the temperature. Note that, here we always refer to the base temperature of the object, not the change in temperature due to the microwave/laser heating. The instantaneous temperature increase in the object due to the microwave/laser pulse heating is on the order of milliKelvin and its effect on the Grueneisen parameter is negligible. The base temperature of the object is a slowly varying parameter compared to the transient temperature increase induced by a microwave/laser pulse.

5.3   System description

Figure 5.1 shows the combined TA and PA system used for sensing temperature. A similar concept of integrating light with microwaves was used earlier for a breast cancer imaging system [53]. The plastic chamber containing the sample holder was filled with mineral oil, a nonmicrowave-absorbing material. Moreover, because mineral oil is visibly transparent, light absorption is negligible. Mineral oil also acts as a coupling medium for sound propagation, and thus, mineral oil was an ideal choice as a background medium for all our experiments. The microwave/laser assembly was placed under the sample holder chamber, from where it illuminated the sample by either microwave or laser, alternately, for TA/PA sensing. The microwave was delivered using a horn antenna, whereas the laser was delivered by a free-space optical assembly. The prism and ground glass of the laser illumination system were incorporated inside the microwave horn antenna. Light was delivered through a drilled $\sim$10-mm-diam hole in one of the narrow walls of the horn antenna. The laser beam was broadened by a concave lens placed outside the hole in the horn antenna, then reflected by the prism and homogenized by the ground glass. This type of beam expansion scheme has been used extensively before [66, 67, 75]. The insertion of the optical devices inside the microwave horn antenna had no significant effect on the microwave delivery [53]. Microwave source, laser source, and the detection of ultrasound is described in chapter 1. The laser was tuned to a fixed wavelength of 532 nm.

Temperature sensor: A precision thermistor for laboratory applications (sealed PVC tip, resistance of 2252 Ω at 25 ^{o}C and accuracy of $\pm$0.1 ^{o}C; ON-401-PP, Omega) was used to measure the temperature of the sample. The tip of the thermistor was
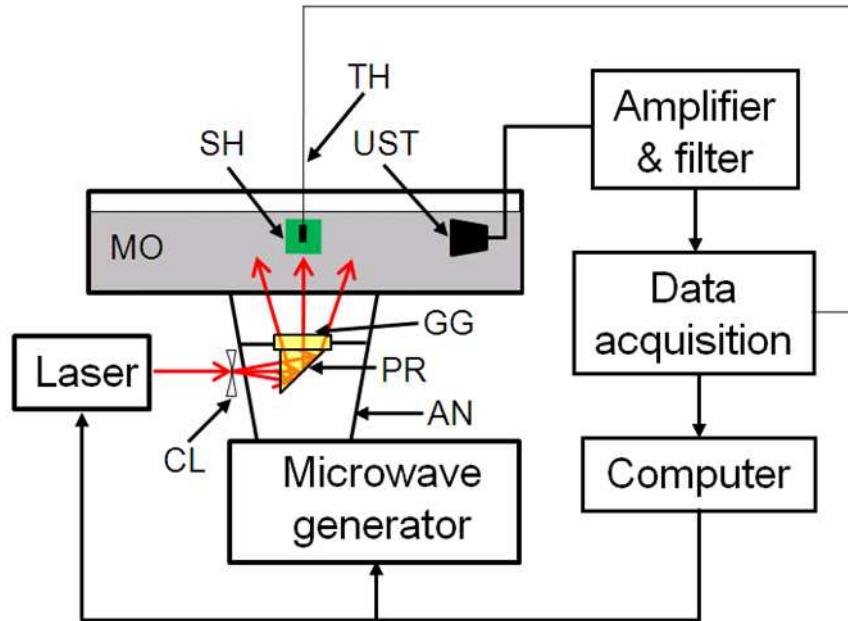
Figure 5.1: Schematic of the experimental setup. MO: mineral oil bath, SH: sample holder vial, UST: ultrasonic transducer, GG: ground glass, PR: prism, AN: horn antenna, CL: concave lens, TH: thermistor.

inserted inside the sample to get an accurate measurement of the temperature. A voltage divider circuit with a dc source (Vizatek, MPS-6003L-1) converted the resistance change of the thermistor in to voltage, which was recorded using a digital oscilloscope. Because the current through the thermistor was very small, the self-heating was negligible.

Experimental procedure: The sample holder vial (LDPE vial with i.d. ∼12 mm and volume ∼5 cc) was filled with different samples, DI water for TA measurements, and ink solution for PA measurements. Two types of experiments were done. A heated sample was allowed to come to room temperature by natural convection, exchanging heat with the background medium (mineral oil). The volume of the sample was very small compared to the mineral oil; thus, the temperature rise of the mineral oil was neglected. The TA/PA signal was recorded with time as the

sample temperature decreased to room temperature. The thermistor was inserted inside the sample to monitor the actual temperature. Next, cold sample was allowed to reach room temperature by natural convection, exchanging heat with mineral oil, and the TA/PA signal was recorded with time as the sample temperature increased to room temperature. The actual temperature of the sample was also monitored using a thermistor as before. Note that, for the decreasing and increasing temperature experiments, the sample holder position may have altered slightly. The sample holder was removed, refilled with cold/hot sample, and then placed back in the system.

5.4   Results and discussion

Figure 5.2(a) shows the peak-to-peak TA signal amplitude and the actual temperature of the DI water. The TA signal decreased as the DI water cooled to room temperature with time. The TA signal follows the actual temperature profile (red line) very well. Figure 5.2(b) plots the TA signal versus the temperature of the sample. The green line shows a linear curve fit with an R^2 of 0.95. A linear relationship between the actual temperature and the TA signal was observed. Figure 5.2(c) shows the TA signal increased when the cold DI water temperature reached room temperature. The TA signal follows the actual temperature profile (red line) very well. Figure 5.2(d) plots the TA signal versus the temperature of DI water, and the green line shows a linear curve fit with an R^2 of 0.91. A linear relationship between the temperature and the TA signal was observed. For water in this temperature range, the Grueneisen parameter is a linear function of temperature [151, 152] and, therefore, the TA signal amplitude also varies linearly with the temperature.
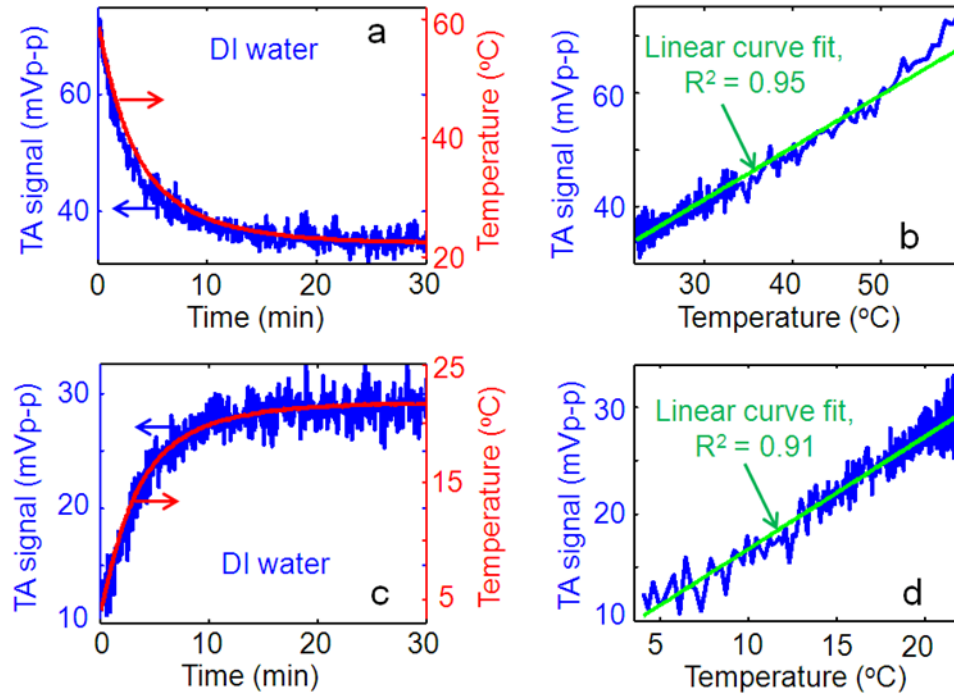
Figure 5.2: (a) TA signal and actual temperature of DI water as heated DI water was allowed to come to room temperature. (b) TA signal versus temperature shows almost a linear relationship (green line) with with an R^2 of 0.95. (c) TA signal and the actual temperature of DI water as cold DI water was allowed to come to room temperature. (d) TA signal versus temperature shows almost a linear relationship (green line) with an R^2 of 0.91.

Similar experiments were done for PA measurements with ink solution as a sample. Figure 5.3(a) shows the PA signal generated from the ink solution and the actual temperature. Once again, the PA signal decreased as the solution temperature approached room temperature, and followed the actual temperature profile (red line) very well. Figure 5.3(b) plots the PA signal versus temperature, with the green line showing a linear curve fit with an R^2 of 0.98. Next, a cold ink solution was allowed to reach room temperature. The PA signal increased as the temperature of the solution increased [Fig. 5.3(c)] and followed the actual temperature profile (red line) very well. Figure 5.3(d) plots the PA signal versus the temperature with the green line showing a linear curve fit with an R^2 of 0.98.
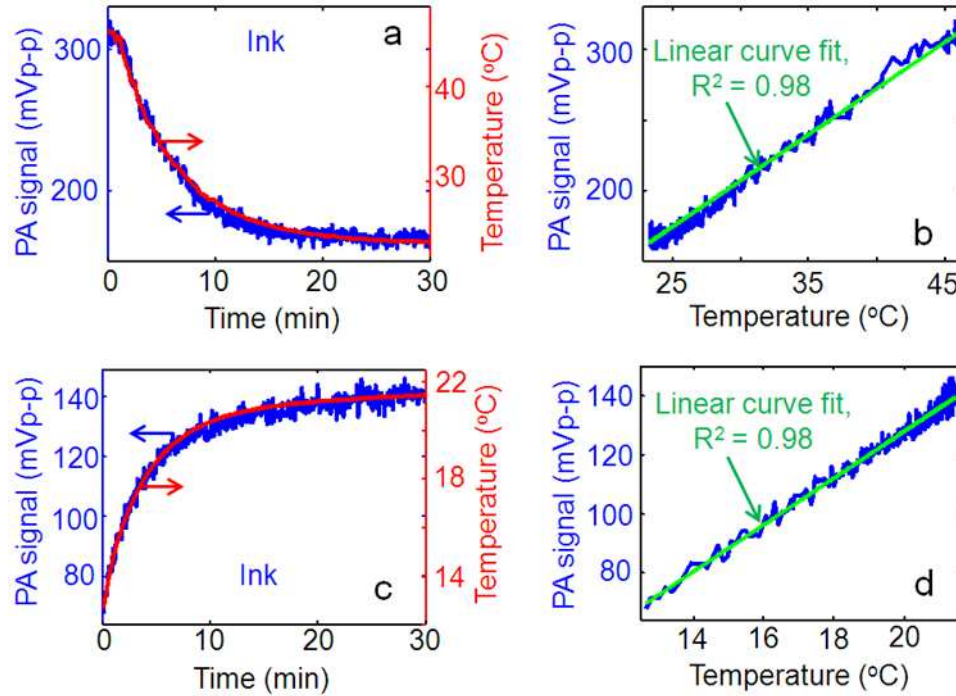
Figure 5.3: (a) PA signal and actual temperature of diluted black ink solution ($\mu_a = 30 \text{ cm}^{-1}$) as the heated sample was allowed to come to room temperature. (b) PA signal versus temperature shows almost a linear relationship. Green line is the linear curve fitting with an R^2 of 0.98. (c) PA signal and the actual temperature of ink solution as cold solution was allowed to come to room temperature. (d) PA signal versus temperature shows almost a linear relationship. Green line is the linear curve fitting with an R^2 of 0.98.

Table 5.1 summarizes the TA/PA measurements. The number of measurements averaged was 20 for each data point, and as the microwave/laser was operating at 10 Hz pulse repetition rate, the temporal resolution was 2 s. We can see the change in signal per degree change in temperature is slightly higher for increasing temperature than for decreasing temperature. It was 3.6% for increasing temperature (compared to 3.0% for decreasing temperature) in the case of TA measurements, and 5.9% for increasing temperature (compared to 4.1% for decreasing temperature) in the case of PA measurements.

Table 5.1: TA/PA signal change per degree centigrade change in temperature of DI water/ink solution in a tube.

		$T_{\max}$ (°C)	$T_{\min}$ (°C)	$S_{\max}$ (mV)	$S_{\min}$ (mV)	Signal change (%/°C)	Signal change (mV/°C)
TA measurements	Decreasing temperature	58.7	22.6	73.3	35.1	3.0	1.0
	Increasing temperature	21.7	4.0	28.9	10.7	3.6	1.0
PA measurements	Decreasing temperature	46.0	23.6	319.8	166.7	4.1	6.8
	Increasing temperature	21.4	12.6	140.3	67.6	5.9	8.3

Figure 5.4(a) shows how the Grueneisen parameter of water varies with temperature ($\Gamma = \frac{\beta V_s^2}{C_p}$) in the temperature range of interest [151, 152]. It increases linearly with temperature, with a slightly higher slope within the range 0–20 °C than within the range 20–100 °C (the slope in the range 0–20 °C is 1.48 times the slope in the range 20–100 °C). This agrees with our observation in both TA and PA measurements for increasing and decreasing temperature. For the TA measurements, the slope in the range 4–22 °C was 1.16 times the slope in the range 23–58 °C, and for the PA measurements the slope in the range 13–22 °C was 1.44 times the slope in the range 24–46 °C. We can also see a slight difference in the signals, depending on the direction from which the sample comes to equilibrium. In the case of TA measurements, the equilibrium signals were 35.1 and 28.9 mV (17.6% difference) for equilibrium reached from cooling and warming, respectively. The corresponding equilibrium temperatures were 22.59 and 21.66 °C. There was an almost 1 °C difference between the two equilibrium temperatures. After accounting for this difference, we see ~14% [17.6−(3.0+3.6)/2 = 14.3%] signal discrepancy. In the case of PA measurements, the equilibrium signals
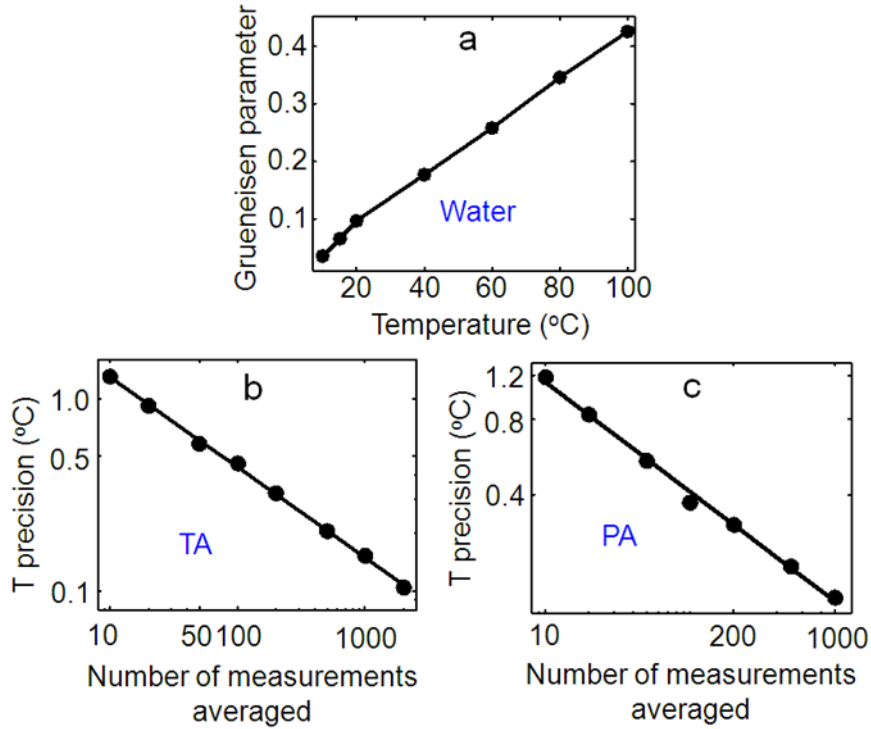
Figure 5.4: (a) Variation of the Grueneisen parameter of water with temperature [151, 152]. (b) Temperature precision versus number of measurements averaged for TA measurements in log-log scale. The plot shows a linear curve with a slope of −0.47. (c) Temperature precision versus number of measurements averaged for PA measurements in log-log scale. The plot shows a linear curve with a slope of −0.44.

were 166.7 and 140.3 mV (15.8% difference) and the equilibrium temperatures were 23.57 and 21.41 ^{o}C, respectively. There was an almost 2 ^{o}C temperature difference between the two equilibrium temperatures. After accounting for this difference, we see ∼6% [15.8−2 × (4.1+5.9)/2 = 5.8%] signal discrepancy. The TA/PA signal generated from the sample is dependent on various factors, such as the orientation of the sample holder and the spatial distribution of microwaves/light on the sample surface. Therefore, the absolute signal is very sensitive to the position of the sample holder. Because the sample holder position was altered slightly between experiments, these variations in signal could arise. If the sample holder had been fixed in its position

between different experiments (increasing and decreasing temperatures), the variation in the signal amplitudes would have been less. Of course, when the technology is used to monitor thermal therapy, the sample will be held stationary.

The temperature measurement precision was ± 1 ^{o}C for TA measurements and ± 0.5 ^{o}C for PA measurements. Here, we have used the terms precision and sensitivity synonymously. The temperature precision is calculated based on the uncertainty in the mean value of the measurements (standard error). The precision would improve if we took a larger sample size. Figure 5.4(b) shows how the temperature precision typically varies with the number of measurements averaged for TA measurements. As expected, the standard error decreased as a factor of the square root of the number of measurements averaged. The greater the number of measurements averaged, the less the standard error, and hence, the higher the precision. The plot is on a log-log scale, yielding a linear curve with -0.47 slope (mean slope $= -0.40 \pm 0.05$, for seven repeated experiments). In an ideal situation, the slope should be -0.5. It is observed that the temperature precision could be as high as ± 0.1 ^{o}C with > 2000 measurements averaged. Of course, the increased precision comes at the expense of temporal resolution. With the current microwave source (a maximum 100 Hz pulse repetition rate), the temporal resolution could be as long as 20 s to achieve a temperature precision of ± 0.1 ^{o}C. However, employing a higher repetition rate microwave source can eventually give us even higher temperature precision with practical temporal resolution. Similarly, figure 5.4(c) shows how the temperature precision varied with the number of measurements averaged for PA measurements. As expected, the precision could be as high as ± 0.1 ^{o}C with > 1000 measurements averaged. As before, the plot is on a log-log scale, with a linear curve with -0.44 slope (mean slope $= -0.40 \pm 0.03$, for five repeated experiments). Note that the precision varies from sample to sample

depending on the SNR. We will show later that, for saline and turkey breast tissue, we obtained even higher precision in temperature based on TA measurements with 20 measurements averaged.
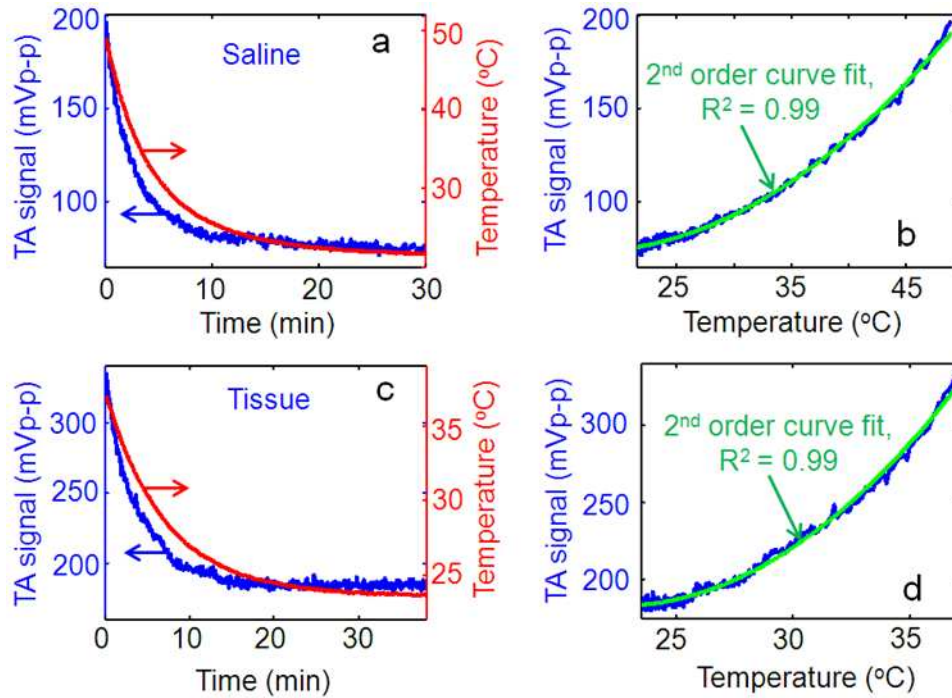
Figure 5.5: (a) Temperature monitoring of saline using TA measurements. TA signal followed the actual temperature profile. (b) TA signal versus temperature showing a second-order relationship (green line)with an R^2 of 0.99. (c) Temperature monitoring of turkey breast tissue using TA measurements. TA signal and actual temperature of turkey breast tissue as heated tissue was allowed to come to room temperature. (d) TA signal versus temperature showing a second-order relationship (green line) with an R^2 of 0.99.

Saline/Tissue temperature monitoring: We also used saline (0.9% w/v of NaCl in water) and turkey breast tissue as a phantom to monitor temperature using TA measurements. The same experimental procedures were followed as before. Figure 5.5(a) shows that the TA signal decreased as the temperature of the saline decreased. The TA signal followed the actual temperature profile (red line) very closely. Figure

5.5(b) shows a second-order curve fit (green line) for the TA signal versus the temperature of saline with an R^2 of 0.99. Figure 5.5(c) shows that the TA signal decreased as the temperature of the tissue decreased. The TA signal followed the actual temperature profile (red line) very closely. Figure 5.5(d) shows a second-order curve fit (green line) for the TA signal versus the temperature with an R^2 of 0.99. Table 5.2 summarizes the TA measurements for the sensing of the saline and turkey breast tissue temperatures. As before, 20 measurements were averaged. For the saline, there was ~5.9% change in TA signal, whereas for tissue there was ~6.1% change in signal per degree centigrade change in temperature. The TA signal generated from the tissue had a very high SNR of ~100 at room temperature (~24 ^oC). Thus, the minimum detectable signal change (i.e., noise-equivalent signal change) is ~1%, which gives us a temperature sensitivity of ~0.15 ^oC (= 1%/6.1%/^oC). However, if the SNR is improved, the sensitivity could be even better. The temperature precision was ±0.15 ^oC (with 20 measurements averaged) based on the standard error. As discussed before, taking the average of a greater number of signals (> 2000) the precision could be improved to ±0.015 ^oC.

Table 5.2: Saline and turkey breast tissue temperature monitoring using TA measurements. The precision is based on taking average of 20 measurements.

	T_{max} (^oC)	T_{min} (^oC)	S_{max} (mV)	S_{min} (mV)	Signal change (%/^oC)	Signal change (mV/^oC)	Precision (^oC)
Saline	49.0	21.9	196.6	75.3	5.9	4.5	±0.3
Turkey breast tissue	37.0	23.6	335.9	184.5	6.1	11.3	±0.15

5.5 Conclusions

We proposed a novel temperature-sensing method based on TA and PA measurements. This noninvasive method has deep-tissue-sensing capabilities. Depending on the tissue types, either the TA or PA component, or both, could be used. We monitored temperature of DI water thermoacoustically within 5 to 60 ^{o}C, and photoacoustically monitored the temperature of diluted ink solution within 12 to 46 ^{o}C. We also showed that the TA-based measurements could be used for saline and turkey breast tissue temperature monitoring. The temperature sensitivity was 0.15 ^{o}C with 2 s (20 measurements averaged) temporal resolution. Measurement precision could be improved by taking more signal averages. In the future, we would like to continue the monitoring of temperature *in vivo* using both TA and PA sensing for various applications, such as temperature monitoring for tissue during radio frequency ablation, radiation therapy, photothermal therapy, photodynamic therapy, cancer treatment using high intensity focused ultrasound (HIFU), and drug delivery using HIFU.

Chapter 6

Conclusions and future directions

6.1   Conclusions

This dissertation presented the feasibility of dual-modality thermoacoustic and photoacoustic imaging, the development of dual-modal contrast agents, the development of a molecular targeted contrast agent for photoacoustic imaging, and a novel temperature sensing technique using thermoacoustic and photoacoustic measurements.

We successfully integrated the two imaging modalities (TAT and PAT) into one system. Our system should be much more comfortable for the patient, and we will not need to apply gel or other chemicals on the skin – our system operates with dry coupling. We also achieved good quality PAT and TAT images of tissue mimicking phantoms, with 0.7 mm spatial resolution and high SNR. We successfully used a negative lens ultrasonic detector to improve the tangential resolution of the breast imaging system. More than twofold resolution improvement was observed in both TAT and PAT. The increase in acceptance angle enabled us to image a larger scanning area, which is especially useful for breast screening. The same concept can be extended to other tomographic imaging systems where a large imaging area is needed and flat

transducers are used as signal detectors. We also showed that a negative lens detector preserves the object shape in the reconstructed images, even when the target is far from the scanning center or close to the detector surface. Such shape preservation could be important in the accurate diagnosis and treatment of tumors.

We developed a dual-modal contrast agent, single-walled carbon nanotubes (SWNTs) for both thermoacoustic and photoacoustic imaging. These nanotubes provided more than twofold signal enhancement in TAT at 3 GHz and more than sixfold signal enhancement in PAT at 1064 nm. We demonstrated a noninvasive SWNTs-enhanced PA identification of SLN in a rat model *in vivo* with a high contrast-to-noise ratio (CNR = 89) and good resolution ($\sim$500 μm). Our results suggest that this technology could be a useful pre-clinical and possibly clinical tool to identify SLNs noninvasively *in vivo*.

We demonstrated the potential for targeted molecular PAT of gold nanobeacons (GNBs). The GNBs provided a more than tenfold signal enhancement in PAT in the NIR wavelength window. *In vitro* and preliminary *in vivo* PAT images substantiated our hypothesis that GNBs can work as a exogenous contrast agent in the NIR wavelengths and they can be used for targeted photoacoustic imaging. We also imaged SLN noninvasively by intradermal injection of GNBs. The uptake of these nanobeacons to the lymph node was particle size dependent. Among the three different sizes of nanobeacons we tried, we found the smallest size particles ($\sim$90 nm diameter) traveled and accumulated in the lymph node faster than the other GNBs of larger sizes ($\sim$160 nm, $\sim$290 nm diameter).

TAT and PAT can be used not only for imaging, but also for therapy. A novel temperature sensing method based on thermoacoustic and photoacoustic measurements

was explored. These noninvasive methods have deep tissue sensing capabilities. Depending on the tissue types, either the TA or PA component, or both, could be used. We monitored the temperature of DI water thermoacoustically within 5 to 60 ^{o}C, and photoacoustically monitored the temperature of diluted ink solution within 12 to 46 ^{o}C. We also showed that the TA-based measurements could be used for saline and turkey breast tissue temperature monitoring. The temperature sensitivity was 0.15 ^{o}C with 2 s (20 measurements averaged) temporal resolution. Measurement precision could be improved by taking more signal averages.

6.2   Future directions

In the future, we propose to integrate TAT and PAT with a clinical ultrasound imaging system. The three compatible imaging modalities could share the same ultrasound detection system and provide complementary contrasts. The long-term goal will be to provide a clinical tool for the early functional monitoring of breast neoadjuvant therapy (chemo- or hormone therapy). Many breast cancer patients receive neoadjuvant treatment to reduce tumor size and enable breast conserving therapy that would otherwise have not been possible. Although it was originally hoped that neoadjuvant therapy would improve patient survival outcomes, data from trials have not shown this benefit. However, this may be due to the inability to monitor response to therapy and modify treatment regimens more carefully. Methods used to monitor response to neoadjuvant chemotherapy or hormone therapy include clinical breast examination, mammography, ultrasound, and magnetic resonance imaging. These methods depend on overall gross tumor morphology and size measurements, which may not

change, despite tumor response on a cellular level. A more sensitive method of detecting response to therapy might allow earlier adjustments in treatment, and might thus result in better outcomes. Furthermore, if drug choices are not resulting in beneficial responses, prompt and early changes in drug regimens will alleviate some of the unnecessary morbidity that patients suffer during treatment while awaiting response to therapy. We believe that the combined contrasts from TAT, PAT, and ultrasonography can accurately predict breast neoadjuvant therapeutic response.

We also propose to study angiogenesis by photoacoustic imaging. Advances in *in vivo* and *in vitro* assays of angiogenesis have been influential for increasing our understanding of regulation of angiogenesis. We will use a Matrigel model to study angiogenesis *in vivo* in rats and mouse. Matrigel is a mixture of basement membrane proteins and growth factors secreted by Engelbreth-Holm-Swarm murine sarcoma cells. It consists of laminin, type IV collagen, entactin, nidogen, heparan sulfate proteoglycan, and growth factors, including transforming growth factor-β, epidermal growth factor, platelet-derived growth factor, and insulin growth factor-1. When endothelial cells are grown *in vitro* on Matrigel, these cells are known to organize into capillary-like tubules. Within 1 h of plating on the gel, endothelial cells form cords, which develop into a three-dimensional branching network. By mixing test substances with Matrigel prior to gel polymerization or by adding them to the endothelial cell suspension, both putative inducers and inhibitors of neovascularization can be studied. This Matrigel model will be used for targeted imaging. Briefly, mice or rats, will be anesthetized and subcutaneously injected with Matrigel (BD Biosciences, San Jose, California), thawed at 4 ºC and enriched with fibroblast growth factor-2 (500 nm/mL; Sigma Aldrich, St. Louis, MO) and heparin (64 U/mL). After injection, the matrigel will form ellipsoidal plug. Following the implant, PA imaging will be performed from day

87

7 onwards. Animals with Matrigel plugs will undergo PA imaging following a treatment of targeted GNBs, and then will be sacrificed. The excised Matrigel plugs will be sectioned in to slices corresponding to the PAT scan plane and stained with $CD31$ immunohistochemical stain. Histologic vascular parameters, including microvascular density (MVD), vessel number (VN), vascular area, and vascular perimeter, will be measured. Then, PAT and histologic parameters will be correlated. It is hoped that the findings will contribute new information on angiogenesis that will be therapeutically valuable.

Appendix A

Safety standards, SWNTs preparation and characterization, animal and drug information

Safety standards for microwave and laser exposure:

For microwave exposure in TAT, we refer to the safety standards of rf heating approved by IEEE [63] and FDA [153, 154]. Rf heating is measured in specific absorption rate (SAR) in units of W/kg. According to the IEEE standards, our case involves microwave exposure under a controlled environment, which means that the exposure is incurred by persons who are aware of the potential for exposure. With 3 GHz microwaves under a controlled environment, the IEEE standards limit the SAR to 0.4 W/kg as averaged over the whole body and limit the spatial peak SAR to 8.0 W/kg as averaged over any 1 gm of tissue. The SARs are averaged over any 6 min interval. The FDA standards are more relaxed than the IEEE counterparts. Note that since MRI uses rf, it is constrained by the same safety standards. We calculated the SAR distribution by simulating the transport of microwave in the breast tissue.

The simulation is done by using the finite difference time domain (FDTD) method [155, 156] with dielectric parameters of breast tissues [157]. It is observed that the local peak SAR value is less than 3.0 W/kg. In addition, since the average power of the microwave source is less than 0.4 W at the current repetition rate and the body weight is over 1 kg, the whole body averaged SAR is guaranteed to be below the IEEE limit. Therefore, the rf heating in the breast is within both the IEEE and FDA safety standards. Further, the detection time at any position will be within five minutes, so the local maximum temperature increase in the breast tissue is less than 0.3 ^oC even if there is no blood perfusion and other heat conduction.

When PAT is used to image human subjects *in vivo*, the maximum permissible pulse energy and the maximum permissible pulse repetition rate are governed by the ANSI laser safety standards [68]. The safety limits for the skin depend on the optical wavelength, pulse duration, exposure duration, and exposure aperture. In the spectral region of 400–700 nm, the maximum permissible exposure (MPE) on the skin surface by any single laser pulse should not exceed 20 mJ/cm^2. In the 700–1050 nm region, the MPE increases with the wavelength λ in nm as $20 \times 10^{2(\lambda-700)/1000}$ mJ/cm^2. At 800 nm, for example, the MPE is 31.7 mJ/cm^2. In the 1050–1400 nm region, the MPE increases to 100 mJ/cm^2. In PAT, the laser beam is always expanded so that the fluence is within the ANSI maximum permissible energy limit.

SWNTs synthesis:

A diblock copolymer templating method was used to coat Fe coated on Si wafers [158]. The wafers were placed in a 3 in quartz reaction chamber (Easy Tube 2000, First Nano) and heated in Ar to 900 ^oC. The chamber was filled with H$_2$ for 2 min,

and CH_4 was added to the gas flow as the carbon feedstock for 20 min to initiate the growth of SWNTs. Subsequently, the carbon feedstock was switched off and the furnace was cooled to room temperature. The SWNTs were further dispersed in 1 wt% Pluronic® F127 surfactant (1 g of surfactant in 100 g of deionized water) at the appropriate concentration and sonicated rigorously to obtain a homogeneous dispersion.

Characterization of SWNTs:

Raman spectroscopy (LabRAM Aramis, Horiba JvonYvon) at 633 nm excitation, transmission electron microscope imaging (JEOL 2000 FX electron microscope operating at 200 kV), ζ potential (Malvern Zetasizer NanoZS system with irradiation from a 632.8 nm He-Ne laser), and atomic force microscopy (MFD-3D-BIO, Asylum Research) were used to characterize the SWNTs.

Figure A.1(a) shows a representative bright-field TEM image of densely populated SWNTs on the surface of the substrate. Further investigation by high-resolution TEM (HRTEM) [Fig. A.1(b)] and AFM [Fig. A.1(c)] showed SWNTs with diameters between 1.2 and 2.2 nm and lengths between 500 nm and 1 μm. Figure A.1(d) shows a representative Raman spectrum of SWNTs at the laser excitation wavelength of 633 nm. The Raman spectrum shows a G band at 1596 cm^{-1} and a D band at 1320 cm^{-1}, with a D/G band ratio for SWNTs of < 0.1, indicating that the SWNTs have very few defects [159]. The radial breathing modes [Fig. A.1(d) inset], unique to SWNTs [159], further corroborate the HRTEM and AFM results and confirm the presence of SWNTs. SWNT suspensions with different concentrations (0.1–1 mg/mL) were prepared in 10 mL of 1% biologically compatible Pluronic® F127 surfactant
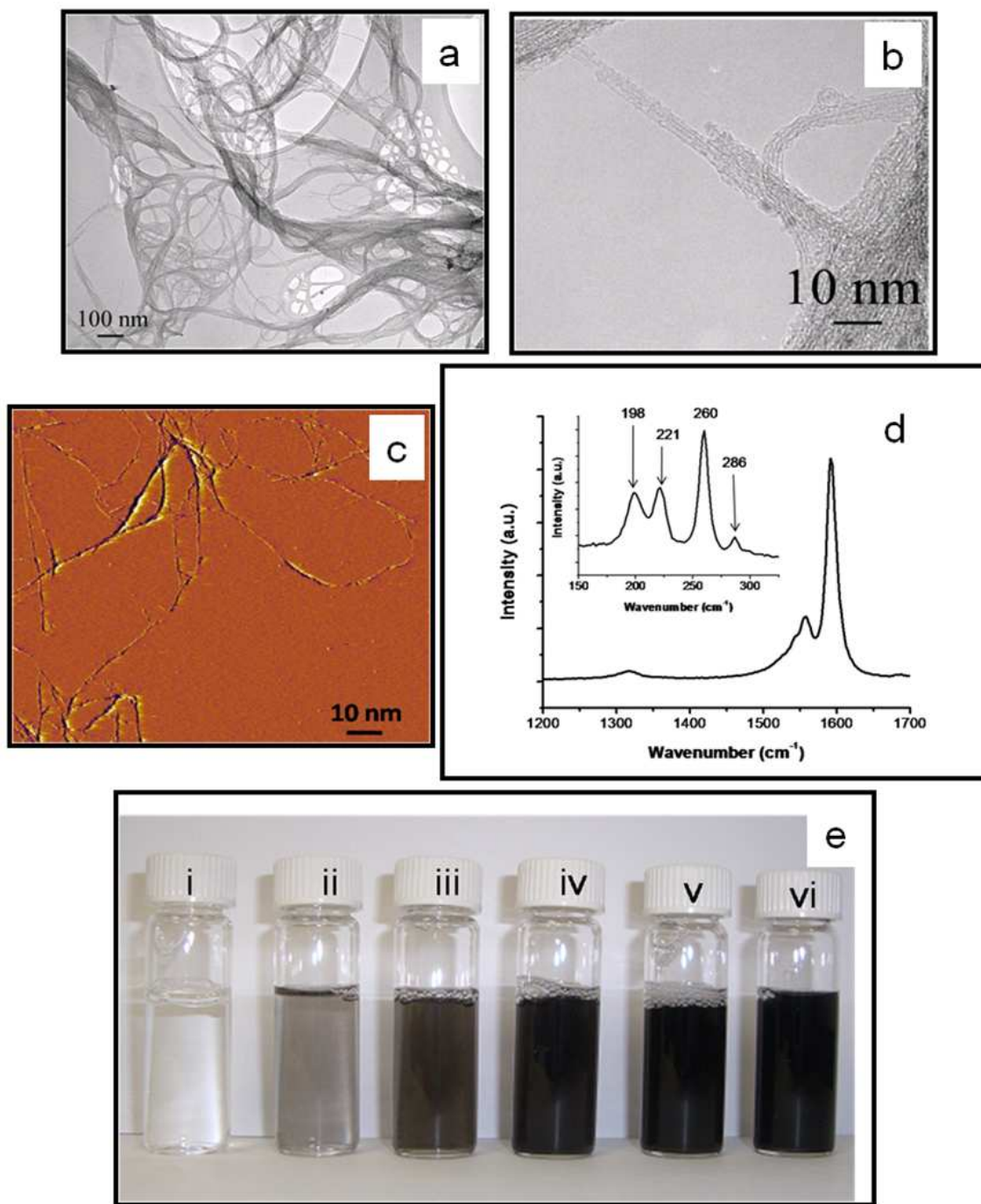
Figure A.1: (a) A low-resolution bright-field TEM, (b) HRTEM image of bundled SWNTs grown using Fe as the catalyst. (c) Tapping mode AFM images of dispersed SWNTs. (d) D-band and G-band Raman spectra of the SWNTs. The inset shows the radial breathing modes. (e) Vials contain aqueous dispersions of SWNTs in Pluronic® F127 after being sonicated. From left to right, the concentrations are (i) 0, (ii) 0.1, (iii) 0.25, (iv) 0.5, (v) 0.75 and, (vi) 1 mg/mL.

solution (pH 7). The different domains of the nonionic Pluronic F127 likely wrapped themselves in energy-minimized conformations around the nanotubes to solubilize the SWNTs by steric stabilization, producing nearly neutral nanotube suspensions [160]. These suspensions were stable during the period of the entire study. The ζ-potential measurements were performed on 0.1 mg/mL SWNTs dispersed in Pluronic F127 and showed a peak ζ potential of -14 mV with a Gaussian distribution (full width half maximum of the distribution = 10 mV). This value is similar to other reported ζ-potential measurements on neutral stable SWNTs dispersed in Pluronic F127 [160]. Figure A.1(e) shows an optical image of the SWNTs (0.1–1 mg/mL concentration) dispersed in Pluronic F127 after aggressive sonication.

Photoacoustic spectroscopy of SWNTs:

Figure A.2(a) shows the PA signals obtained from a tygon tube (i.d. 250 μm, o.d. 500 μm) filled with SWNTs (0.25 mg/mL) and rat blood. The laser was tuned to 764 nm wavelength. At this excitation wavelength, the peak-to-peak PA signal amplitude obtained from SWNTs was ~600 mV, compared to a ~170 mV peak-to-peak PA signal amplitude from blood alone. Figure A.2(b) shows the PA spectrum (peak-to-peak PA signal amplitude versus excitation light wavelength) of the SWNTs (in black) for an excitation wavelength range of 740–820 nm. The PA spectrum of rat blood (in red) is also shown in the same figure. It is evident that the PA signal obtained from SWNTs is much stronger than that of blood over the entire wavelength range. Therefore, one can choose a specific light wavelength for imaging within a broad range. Figure A.2(c) plots the ratio of the peak-to-peak PA signal amplitude of SWNTs to that of blood between 740 and 820 nm. The PA signal from the tygon tube filled with SWNTs is more than four times stronger than that from blood at 750 nm. Over the entire

93

740–820 nm window, the PA signal from SWNTs is more than two times stronger than that from blood.
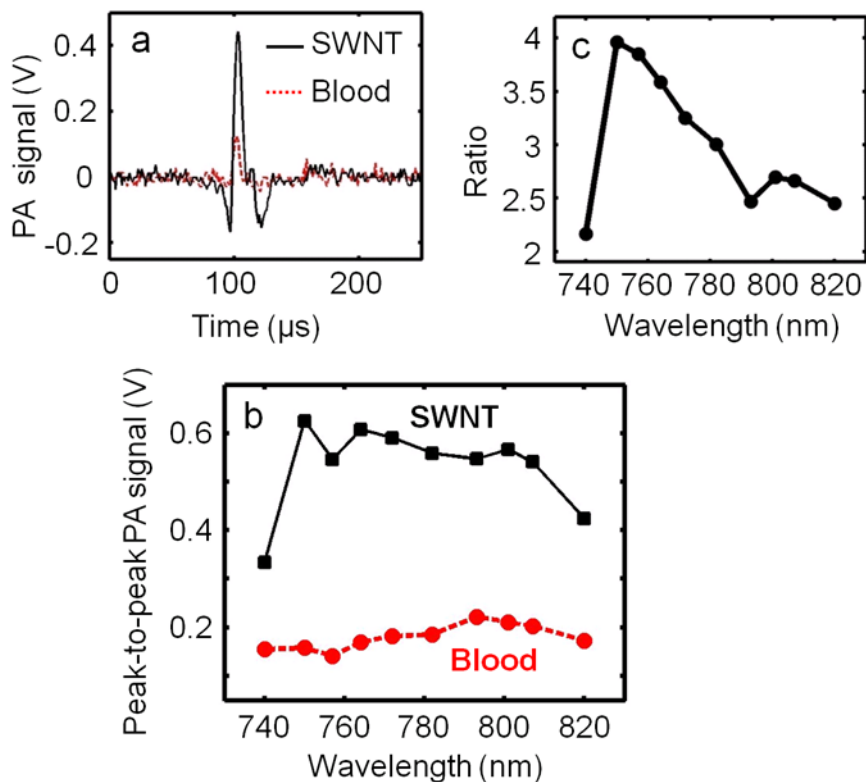
Figure A.2: (a) PA signals generated from a tygon tube (i.d. 250 μm, o.d. 500 μm) filled with SWNTs (0.25 mg/mL) and rat blood. The excitation optical wavelength is 764 nm. (b) PA spectra of SWNTs and blood over a 740–820 nm range of NIR wavelengths. (c) Ratio of the peak-to-peak PA signal amplitudes generated from SWNTs to those generated from blood.

Animal and drug information:

Guidelines on the care and the use of laboratory animals at Washington University in St. Louis were followed for all animal experiments. Adult Sprague Dawley rats with body weights ranging from 250–350 g were used for the *in vivo* studies. Initial anesthetization of the rat was done using a mixture of ketamine (85 mg/kg) and xylazine

(15 mg/kg). During the image acquisition, anesthesia was maintained using vaporized isoflurane (1 L/min oxygen and 0.75% isoflurane, Euthanex Corp.), and a pulse oximeter (NONIN Medical INC., 8600V) was used to monitor the vitals. If needed, 0.9% saline was administered to the rat for hydration. After image acquisition, the animal was euthanized by pentobarbital overdose.

For *in vivo* imaging the hair on the region of interest of the rat was gently removed before imaging, using a commercial hair-removal lotion. For SLN imaging 75-150 μL of intradermal injection was performed on the left/right forepaw pad, depending on which side of the rat was imaged.

Appendix B

GNBs preparation and characterization

Materials:

Unless otherwise listed, all solvents and reagents were purchased from Aldrich Chemical Co. (St. Louis, MO) and used as received. Anhydrous chloroform and methanol were purchased from Aldrich Chemical Co. and distilled over calcium hydride prior to use. Poly(styrene-b-acrylic acid) [135–138] (PS-b-PAA) was purchased from Polymer Source Inc. (Montreal, Canada). Biotinylated dipalmitoyl-phosphatidylethanolamine and high purity egg yolk phosphatidylcholine were purchased from Avanti Polar Lipids, Inc. Cholesterol and octylthiol-coated gold nanoparticles were purchased and used as received from Aldrich Chemical Co. (St. Louis, MO). Sorbitan monolaurate was purchased from Aldrich. Argon and nitrogen (Ultra High Purity: UHP, 99.99%) were used for storage of materials. The Spectra/Por membrane (Cellulose MWCO: 10,000 Da) used for dialysis was obtained from Spectrum Medical Industries, Inc. (Laguna Hills, CA).

Methods:

Preparation of GNB: In a typical procedure, octanethiol-coated gold nanoparticles (2–4 nm) in toluene (100 mg) are suspended in almond oil (4 mL) and vigorously vortexed to homogeneity. The suspension was filtered through a small bed of cotton. The solvent was evaporated under reduced pressure at 60 ^{o}C. The surfactant comixture included high-purity egg yolk phosphatidylcholine (91 mol%, 377.4 mg), cholesterol (8 mol%, 16.9 mg), and biotinylated dipalmitoyl phosphatidylethanolamine (1 mol%, 5.8 mg). The surfactant co-mixture was dissolved in chloroform, evaporated under reduced pressure, dried in a vacuum oven at 40 ^{o}C overnight, and dispersed into water by probe sonication. This suspension was combined with the gold nanoparticles suspended in almond oil (20% v/v, 0.2 mm) in distilled deionized water (77.3% w/v), and glycerin (1.7% w/v). The mixture was continuously processed thereafter at 20000 psi (ca. 137.9 MPa) for 4 min with an S110 Microfluidics emulsifier at 4 ^{o}C. The nanobeacons were dialyzed against water using a 20000 Da MWCO cellulose membrane for a prolonged period of time (3 days) and then passed through a 0.45 μm Acrodisc syringe filter. To prevent bacterial growth, the nanobeacons were stored under an argon atmosphere (typically at 4 ^{o}C). Dynamic light scattering: average diameter $D_{av} = (154\pm10)$ nm; $\zeta = (-47\pm7)$ mV. AFM: average height $H_{av} = (101\pm51)$ nm.

Typical procedure for preparation of control nanobeacon: In a typical experimental procedure, the surfactant co-mixture included high purity egg yolk phosphatidylcholine (90 mole%, 558.6 mg), cholesterol (8 mole%, 26.3 mg), and biotinylated-dipalmitoyl phosphatidylethanolamine (2 mole%, 16.2 mg).

Figure B.1: Number-averaged hydrodynamic diameter profiles for (a) GNB and (b) control nanobeacon from dynamic light scattering measurements; (c) distribution of particle height of GNB from AFM analyses; (d) change in particle sizes over time (> 150 days stored at 4 ^{o}C under argon in sealed serum vials).

The surfactant co-mixture was dissolved in chloroform, filtered and evaporated under reduced pressure, dried in a 40 ^{o}C vacuum oven overnight, and dispersed into water by probe sonication. This suspension was combined with the almond oil mixture (20% v/v), distilled deionized water (77.3% w/v), and glycerin (1.7% w/v). The mixture was continuously processed thereafter at 20,000 PSI for 4 min with an S110 Microfluidics emulsifier (Microfluidics) at 4 ^{o}C. The nanobeacons were dialyzed against water using a 20,000 Da MWCO cellulose membrane for a prolonged period of time and then passed through a 0.45 μm Acrodisc Syringe filter. To prevent bacterial growth the nanobeacons were stored under argon atmosphere typically at 4 ^{o}C.

DLS (D_{av})/nm = 153±11 nm; Zeta (ζ)/mV = −23±09 mV; PDI: 0.14±0.02.

Preparation of L-GNB$_{90}$: In a typical experimental procedure, octanethiol coated gold nanoparticles (2-4 nm, Aldrich Inc., 2% w/v) in toluene (100 mg) were suspended in sorbitan sesquioleate (4 mL, 2 mole%) and vigorously vortexed to homogeneity. The suspension was filtered through a small bed of cotton. The solvent was evaporated under reduced pressure at 45 °C. The surfactant co-mixture included high purity egg yolk phosphatidylcholine (91 mole%, 380 mg), cholesterol (8 mole%, 17.39 mg), and biotinyl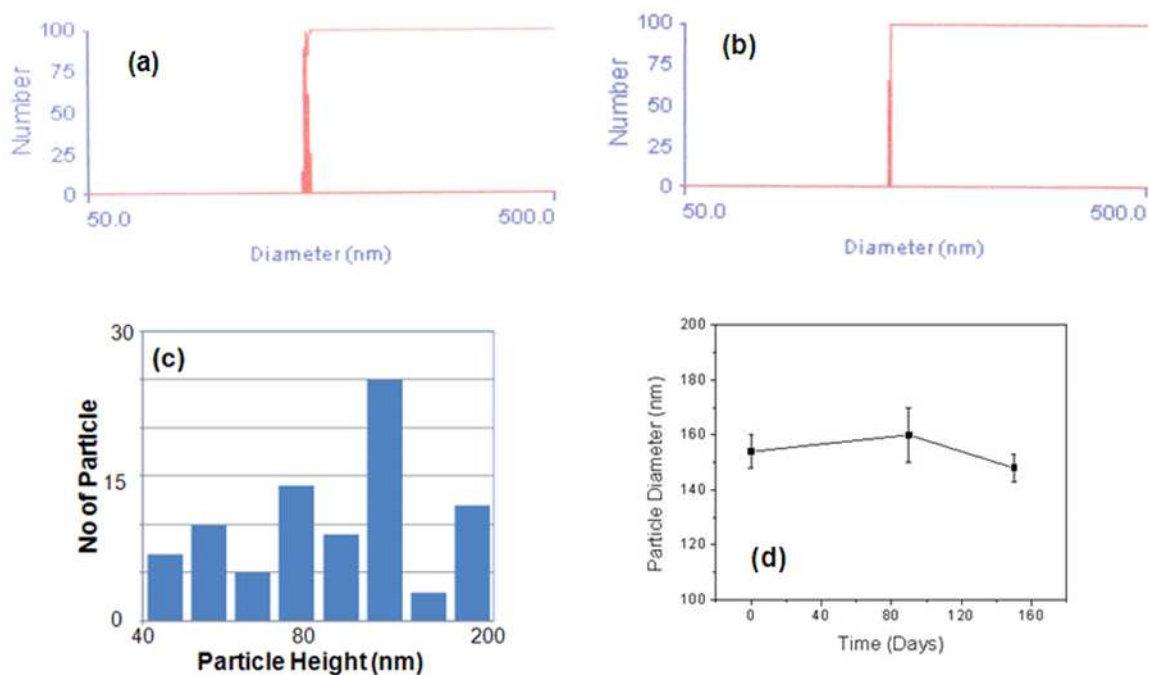ated-dipalmitoyl phosphatidylethanolamine (1 mole%, 6.2 mg). The surfactant co-mixture was dissolved in chloroform, evaporated under reduced pressure, dried in a 40 °C vacuum oven overnight, and dispersed into water by probe sonication. This suspension was combined with the gold nanoparticle-suspended sorbitan sesquioleate mixture (20% v/v), distilled deionized water (15.23 mL, 77.3% w/v), and glycerin (0.37 mL, 1.7%, w/v). The mixture was continuously processed thereafter at 20,000 PSI for 4 minutes with an S110 Microfluidics emulsifier (Microfluidics) at 4 °C. The nanobeacons were dialyzed against water using a 20,000 Da MWCO cellulose membrane for a prolonged period of time and then passed through a 0.45 μm Acrodisc Syringe filter. To prevent bacterial growth the nanobeacons were stored under an argon atmosphere typically at 4 °C. DLS (D$_{av}$)/nm = 92±13 nm; Zeta (ζ)/mV = −55±14 mV; AFM (H$_{av}$)/nm = 45±10 nm, ICP-MS = 1.56 μg of gold /g of 20% colloidal suspension.

Preparation of P-GNB$_{290}$: In a typical experimental procedure, octane thiol coated gold nanoparticles (2-4 nm, Aldrich Inc.) in toluene were suspended in sorbitan monolaurate (1 mL, 5 mole%) and vigorously vortexed to homogeneity. The suspension was filtered through a small bed of cotton. The amphiline PS-b-PAA [135–138] (Mn × 10^{-3}: 0.8-b-29.3 polydispersity index: PDI = 1.18, 0.0034 mmoles, 104.0 mg, 0.5 mole%) was dissolved in a mixture of methanol and chloroform (4:1), filtered

through a small bed of cotton, evaporated under reduced pressure at 50 ^{o}C, dried in a 40 ^{o}C vacuum oven for 6 h, and dispersed into water by probe sonication until a clear suspension was obtained. This suspension (10 mL) was combined with the gold nanoparticle-suspended polysorbate mixture (1 mL, 5 mole%), distilled deionized water (8.45 mL, 0.2 μM), and glycerin (0.45 mL). The mixture was then briefly probe sonicated at ambient temperature followed by continuous processing at 20,000 PSI (137.9 MPa) for 4 minutes with an S110 Microfluidics emulsifier (Microfluidics) at 4 ^{o}C. The nanobeacons were purified by exhaustive dialysis against deionized water using 20 KDa MW CO cellulosic membrane. The nanoparticles were recovered and passed through a 0.45 μm Acrodisc Syringe filter. To slow microbial growth the colloids were stored under an argon atmosphere typically at 4 ^{o}C. DLS (D$_{av}$)/nm = 289$\pm$24 nm; Zeta (ζ)/mV = -35 ± 08 mV; AFM (H$_{av}$)/nm = 153$\pm$31 nm, PDI = 0.15$\pm$0.04, ICP-MS = 134 μg of gold /g of 10% colloidal suspension.

Measurements:

Dynamic light scattering measurements: Hydrodynamic diameter distribution and distribution averages for the GNB and controls in aqueous solutions were determined by dynamic light scattering. Hydrodynamic diameters were determined using a Brookhaven Instrument Co. (Holtsville, NY) Model Zeta Plus particle size analyzer. Measurements were made following dialysis (MWCO 10 kDa dialysis tubing, Spectrum Laboratories, Rancho Dominguez, CA) of GNB suspensions into deionized water (0.2 M). Nanobeacons were dialyzed into water prior to analysis. Scattered light was collected at a fixed angle of 90^0. A photomultiplier aperture of 400 mm was used, and the incident laser power was adjusted to obtain a photon counting rate between 200 and 300 kcps. Only measurements for which the measured and calculated

baselines of the intensity autocorrelation function agreed to within +0.1% were used to calculate nanoparticle hydrodynamic diameter values. All determinations were made in multiples of five consecutive measurements.

Electrophoretic potential measurements: Zeta potential (ζ) values for the GNB were determined with a Brookhaven Instrument Co. (Holtsville, NY) model Zeta Plus zeta potential analyzer. Measurements were made following dialysis (MWCO 10 kDa dialysis tubing, Spectrum Laboratories, Rancho Dominguez, CA) of GNB suspensions into water. Data were acquired in the phase analysis light scattering (PALS) mode following solution equilibration at 25 ^oC. Calculation of ζ from the measured nanoparticle electrophoretic mobility (μ) employed the Smoluchowski equation: $\mu = \varepsilon\zeta/\eta$, where ε and η are the dielectric constant and the absolute viscosity of the medium, respectively. Measurements of ζ were reproducible to within ±4 mV of the mean value given by 16 determinations of 10 data accumulations.

UV-visible spectroscopy: Absorption measurements were made with a Shimadzu UV-1601 P/N 206-67001 spectrophotometer using Shimadzu-UV probe 2.21 software.

Transmission electron microscopy measurements: Glow discharged carbon/ formvar coated nickel grids were floated on a drop of sample for 2 min. Grids were blotted, rinsed quickly in water, and stained in 1% aqueous uranyl acetate for 1 min. Samples were blotted, air dried, and viewed on a Zeiss 902 Electron Microscope, and recorded with Kodak E.M. film. Micrographs were collected at 100,000X magnification. The number-average particle diameter (D_{ah}) values and standard deviations were generated from the analyses of a minimum of 100 particles from three micrographs.

Atomic force microscopy measurements: A Digital Instruments Dimension 3000 series AFM (calibration date 08/2008) and standard Veeco tapping mode silicon probes w/PtIr coating were used for scanning the samples.

In a typical methodology, aqueous suspensions of GNB samples were dried in a class 10000-clean room on a clean glass slide for 3 h. Once dried, samples were placed on the AFM and scanned. Pertinent scanning parameters were as follows: Resonant frequency (probe): 60–80 kHz; Example of tip velocity: (4 μm/s for 2 μm), (15 μm/s for 5 μm), (30 μm/s for 10 μm). Aspect ratio: 1:1; Lift height: 20 nm; Resolution: 512 samples/line, 256 lines. The average particle height (H_{av}) values and standard deviations were generated from the analyses of a minimum of 100 particles from three micrographs.

Inductively coupled plasma-optical emission spectroscopy (ICP-OES): The iodine and bismuth contents of cROMP were analyzed by inductively coupled plasma-optical emission spectroscopy (ICP-MS, SOP7040, Rev 9) conducted at the Bodycote, West Coast Analytical Service (WCAS), Santa Fe Springs, CA. Briefly, the samples were analyzed by a Leeman Labs Direct Reading Echelle ICP-MS, or a DRE (Direct Reading Echelle) instrument which was designed to handle sub-ppm to percent level metal concentrations. DRE consists of a 2 dimensional, high resolution Echelle grating which precisely and reliably locate any peak in the ICP spectrum.

***In vitro* human plasma clot phantoms:** In a typical procedure, whole porcine blood was obtained fresh and anticoagulated (9:1 vol/vol) with sterile sodium citrate. Plasma clots were produced by combining plasma and 100 mmol/L calcium chloride (3:1 vol/vol) with 5 U thrombin (Sigma-Aldrich, Inc.) in an LDPE tube ($\sim$1 cc volume, i.d. $\sim$6 mm). The plasma was allowed to coagulate slowly at room temperature.

The clots were incubated individually with 150 μg biotinylated antifibrin monoclonal antibody (NIB5F3) [131] in 10 mL PBS with 1% crystalline BSA (Sigma Chemical Co) for 2 h. The antibody-treated clots were then incubated with excess avidin (50 μg/mL PBS) for 30 min, followed by biotinylated GNB (30 μL/mL PBS) for 30 min. The control clots were treated similarly with control nanoparticle (30 μL/mL PBS).

Staining of human plasma clot phantoms: Biebrich Scarlet-Acid Fuchsin Solution was diluted 1:1 in 1X PBS. Plasma clot targeted with GNB and control samples were incubated with 200 μL diluted staining solution on the surface at room temperature for five minutes, then wash with 1X PBS for three times. Keep samples in 1X PBS buffer at refrigerator overnight.

Noninvasive PA imaging with L-GNB$_{90}$: Figure B.2 shows the noninvasive lymph node imaging with L-GNB$_{90}$s as the contrast agent. Different concentration of the L-GNB$_{90}$s was tried and all of them were able to show the lymph node very clearly.

Although the preparation of GNBs utilized in general pharmaceutically accepted components such as phospholipids, vegetable oil, glycerin etc, the more in depth animal studies are warranted to understand the behavior of each component *in vivo*.
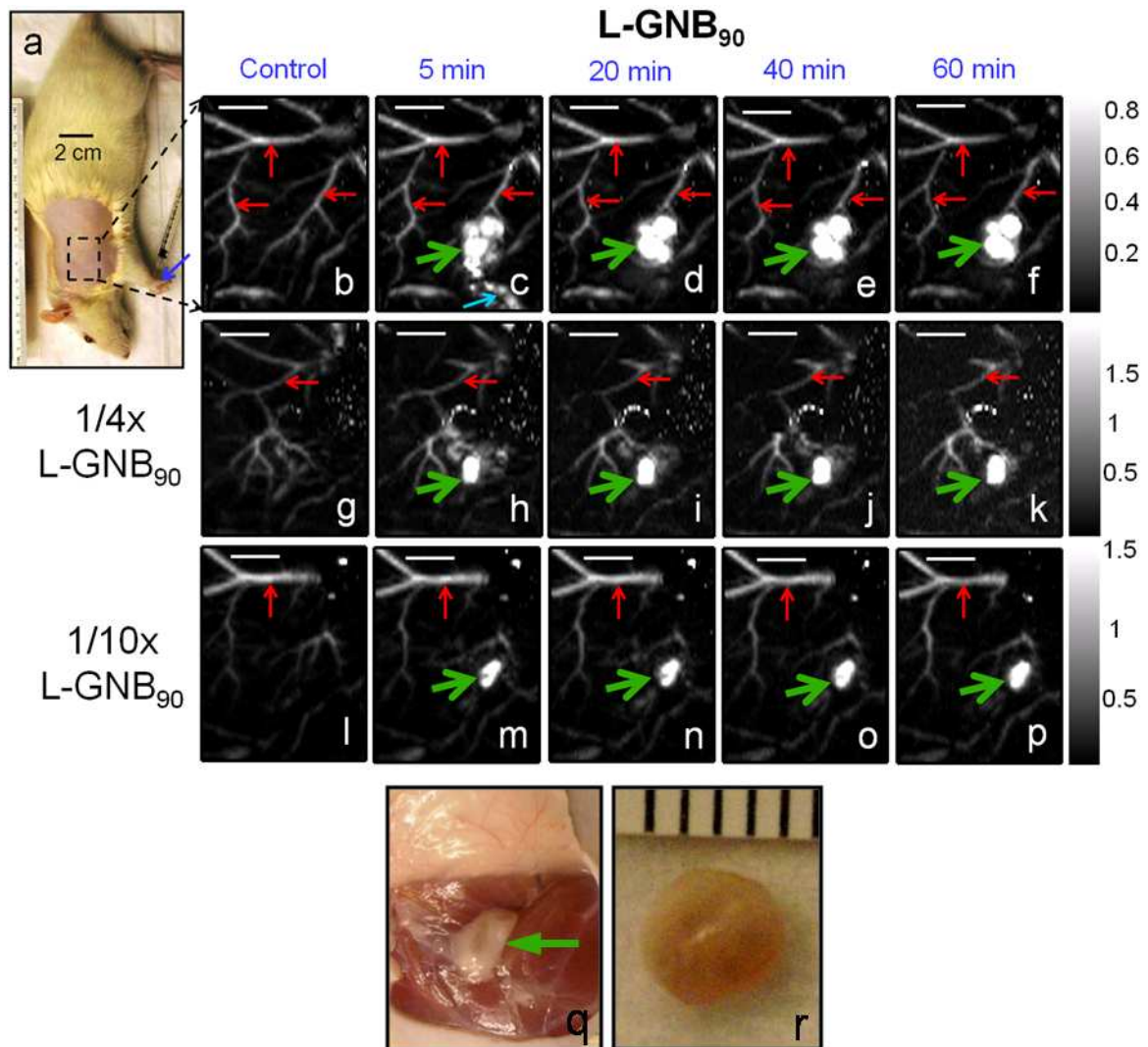
Figure B.2: *In vivo* photoacoustic imaging of sentinel lymph nodes of rat noninvasively. $\lambda = 767$ nm. (a) Photograph of the rat after the hair was removed from the scanning region before taking the PA images. The scanning region is marked with a black dotted square. (b–p) Sagittal maximum amplitude projection (MAP) [38] images. Blood vessels are marked with red arrows, SLNs are marked with green arrow, lymph vessel is marked with blue arrow. Scale bar: 5 mm. (b, g, l) Control PA image with no nanobeacons injected. (c–f) 10 nM L-GNB$_{90}$s were used. (h–k) Four times diluted L-GNB$_{90}$s (2.5 nM) were used. (m–p) Ten times diluted L-GNB$_{90}$s (1 nM) were used. (q) Digital optical photograph of the rat with the skin removed after PA imaging. Lymph node area is shown with green arrow. (r) Excised lymph node. Smallest tick: 1 mm.

Appendix C

Imaging systems

Reflection-mode deep photoacoustic imaging system [97]:

A tunable Ti:sapphire laser (LT-2211A, LOTIS TII) pumped by Q-switched Nd:YAG (LS-2137, LOTIS II) laser was the light source, providing < 15 ns pulse duration and a 10 Hz pulse repetition rate. A dark-field ring-shaped illumination was used [37]. The light energy on the sample surface was controlled to conform to the ANSI standard for maximum permissible exposure [68]. A 3.5 MHz/5 MHz central frequency, spherically focused (4.95 cm/2.54 cm focus length, 1.91 cm diameter active area element, and 70%/72% bandwidth) ultrasonic transducer (V380/V308, Panametrics-NDT) was used to acquire the generated PA signals. The signal was then amplified by a low-noise amplifier (5072PR, Panametrics-NDT), and recorded using a digital oscilloscope (TDS 5054, Tektronix) with a 50 mega-sampling rate. PA signal fluctuations due to pulse-to-pulse energy variation were compensated by signals from a photodiode (DET110, Thorlabs), which sampled the energy of each laser pulse.

A linear translation stage (XY-6060, Danaher Motion) was used for raster scanning to obtain three-dimensional (3-D) PA data. A computer controlled the stage and synchronized it with the data acquisition. To shorten the data acquisition time,

a continuous scan was used without signal averaging. An A-line (A-scan) was the PA signal obtained along the depth direction at a single point. Multiple A-lines [acquired by a one-dimensional (1-D) scan] gave a two-dimensional (2-D) B-scan. A 3-D image was acquired with a 2-D scan. A 1-D depth-resolved image was obtained by multiplying the time axis of the initial A-scan (resolved in time along the depth direction) by the speed of sound in soft tissue ($\sim$1500 m/s).

The scanning time depends on the laser pulse repetition rate (PRR), the scanning step size, and the FOV. Typical values are a scanning step size for a 1-D scan = 0.2 mm, for a 2-D scan = 0.4 mm, a laser PRR = 10 Hz, and a FOV = 24 mm $\times$ 24 mm. The acquisition time = $\sim$25 sec for a B-scan, and = $\sim$18 min for a 3-D image. Please note that no signal averaging is done for any of the PA images. The transducer was located inside a water container with an opening of 5 cm $\times$ 5 cm at the bottom, sealed with a thin, clear membrane. The object was placed under the membrane, and ultrasonic gel was used for coupling the sound.

Curved array photoacoustic tomographic system [161]:

The light source was same as in reflection-mode deep photoacoustic imaging system. A uniform illumination area of approximately 20 mm in diameter on the sample surface was produced by diverging the laser beam with a concave lens and homogenizing it by a circular diffuser. The sample was placed at the center (focal point of the curved transducer) and was illuminated orthogonal to the imaging plane of the transducer for maximum uniformity. The transducer consisted of 128 elements arranged along a 90^0 arc with a 25 mm center of curvature (5 MHz central frequency, BW 80%, custom manufactured Imasonic Inc., Besanon, France).The transducer used piezocomposite

technology for high sensitivity and signal-to-noise ratio. Individual elements had an elevation height of 10 mm with an azimuthal pitch of one wavelength (0.308 mm) and kerf of 0.1 mm. Electronic beam formation provided in-plane dynamic focusing. PA signals from each element were amplified with 60–70 dB gain and multiplexed in to 16 parallel data acquisition channels. The data was DMA-transferred to RAM and subsequently to disk for post-processing. The acquisition rate was 1 frame/second. Images were reconstructed using a delay-and-sum algorithm [162].

References

[1] *http://www.cancer.gov/cancertopics/types/breast.*

[2] E. D. Pisano, "Diagnostic performance of digital versus film mammography for breast-cancer screening (vol 353, pg 1773, 2005)," *New England Journal of Medicine*, vol. 355, no. 17, pp. 1840–1840, 2006.

[3] C. D. Lehman, C. Isaacs, M. D. Schnall, E. D. Pisano, S. M. Ascher, P. T. Weatherall, D. A. Bluemke, D. J. Bowen, P. K. Marcom, D. K. Armstrong, S. M. Domchek, G. Tomlinson, S. J. Skates, and C. Gatsonis, "Cancer yield of mammography, MR, and US in high-risk women: Prospective multi-institution breast cancer screening study," *Radiology*, vol. 244, no. 2, pp. 381–388, 2007.

[4] C. Kuhl, "The current status of breast MR imaging - part I. choice of technique, image interpretation, diagnostic accuracy, and transfer to clinical practice," *Radiology*, vol. 244, no. 2, pp. 356–378, 2007.

[5] C. D. Lehman, C. Gatsonis, C. K. Kuhl, R. E. Hendrick, E. D. Pisano, L. Hanna, S. Peacock, S. F. Smazal, D. D. Maki, T. B. Julian, E. R. DePeri, D. A. Bluemke, and M. D. Schnall, "MRI evaluation of the contralateral breast in women with recently diagnosed breast cancer," *Journal of Womens Health*, vol. 16, no. 6, pp. 929–929, 2007.

[6] D. Saslow, C. Boetes, W. Burke, S. Harms, M. O. Leach, C. D. Lehman, E. Morris, E. Pisano, M. Schnall, S. Sener, R. A. Smith, E. Warner, M. Yaffe, K. S. Andrews, and C. A. Russell, "American cancer society guidelines for breast screening with MRI as an adjunct to mammography," *CA - A Cancer Journal for Clinicians*, vol. 57, no. 2, pp. 75–89, 2007.

[7] P. H. Kuo, E. Kanal, A. K. Abu-Alfa, and S. E. Cowper, "Gadolinium-based MR contrast agents and nephrogenic systemic fibrosis," *Radiology*, vol. 242, no. 3, pp. 647–649, 2007.

[8] S. S. Chaudhary, M. R. K., S. A., and T. J. M., "Dielectric properties of normal & malignant human breast tissues at radiowave & microwave frequencies," *Indian Journal of Biochemistry and Biophysics*, vol. 21, no. 2, pp. 76–79, 1984.

[9] C. C. Johnson and A. W. Guy, "Nonionizing electromagnetic wave effects in biological materials and system," *Proc. IEEE*, vol. 60, no. 6, pp. 692–718, 1972.

[10] K. R. Foster and J. L. Schepps, "Dielectric-properties of tumor and normal-tissues at radio through microwave-frequencies," *Journal of Microwave Power and Electromagnetic Energy*, vol. 16, no. 2, pp. 107–119, 1981.

[11] F. Homburger and W. H. E. Fishman, *The Physiopathology of Cancer.* New York: Hoeber Harper, 1953.

[12] R. G. Olsen, "Generation of acoustic images from the absorption of pulsed microwave energy," in *Acoustic Imaging* (J. P. Powers, ed.), pp. 53–59, New York: Plenum, 1982.

[13] J. C. Lin and K. H. Chan, "Microwave thermoelastic tissue imaging - system-design," *IEEE Transactions on Microwave Theory and Techniques*, vol. 32, no. 8, pp. 854–860, 1984.

[14] R. L. Nasoni, G. A. Evanoff, J. P. G. Halverson, and T. Bowen, "Thermoacoustic emission by deeply penetrating microwave radiation," in *Ultrason. Sym. Proc.*, vol. 5, pp. 633–637, 1984.

[15] K. H. Chan and J. C. Lin, "Microwave-induced thermoacoustic tissue imaging," in *Proceeding of the Annual International Conference of the IEEE Engineering in Medicine and Biology Society*, (New Orleans), pp. 445–446, 1988.

[16] R. G. Olsen and J. C. Lin, "Acoustic imaging of a model of a human hand using pulsed microwave irradiation," *Bioelectromagnetics*, vol. 4, pp. 397–400, 1983.

[17] L. H. V. Wang, X. M. Zhao, H. T. Sun, and G. Ku, "Microwave-induced acoustic imaging of biological tissues," *Review of Scientific Instruments*, vol. 70, no. 9, pp. 3744–3748, 1999.

[18] R. A. Kruger, K. D. Miller, H. E. Reynolds, W. L. Kiser, D. R. Reinecke, and G. A. Kruger, "Breast cancer in vivo: Contrast enhancement with thermoacoustic CT at 434 MHz - feasibility study," *Radiology*, vol. 216, no. 1, pp. 279–283, 2000.

[19] F. W. Kremkau, *Diagnostic ultrasound: principles and instruments.* Philadelphia: W. B. Saunders, 1993.

[20] J. H. Jacobi and L. E. Larsen, "Microwave time delay spectroscopy imagery of isolated canine kidney," *Medical Physics*, vol. 7, no. 1, pp. 1–7, 1980.

[21] J. L. Guerquin-Kern, G. Peronnet, L. Jofre, and J. C. Bolomey, "Active microwave tomographic imaging of isolated, perfused animal organs," *Bioelectromagnetics*, vol. 6, pp. 145–156, 1985.

[22] L. E. Larsen, J. H. Jacobi, I. M. Theory, and T. Society., *Medical applications of microwave imaging.* New York: IEEE Press, 1986.

[23] M. S. Hawley, A. Broquetas, L. Jofre, J. C. Bolomey, and G. Gaboriaud, "Microwave imaging of tissue blood content changes," *Journal of Biomedical Engineering*, vol. 13, no. 3, pp. 197–202, 1991.

[24] M. Miyakawa, "Tomographic measurement of temperature-change in phantoms of the human-body by chirp radar-type microwave computed-tomography," *Medical and Biological Engineering and Computing*, vol. 31, pp. S31–S36, 1993.

[25] P. M. Meaney, K. D. Paulsen, A. Hartov, and R. K. Crane, "An active microwave imaging-system for reconstruction of 2-D electrical property distributions," *IEEE Transactions on Biomedical Engineering*, vol. 42, no. 10, pp. 1017–1026, 1995.

[26] S. Y. Semenov, R. H. Svenson, A. E. Boulyshev, A. E. Souvorov, V. Y. Borisov, Y. Sizov, A. N. Starostin, K. R. Dezern, G. P. Tatsis, and V. Y. Baranov, "Microwave tomography: Two-dimensional system for biological imaging," *IEEE Transactions on Biomedical Engineering*, vol. 43, no. 9, pp. 869–877, 1996.

[27] E. C. Fear and M. A. Stuchly, "Microwave system for breast tumor detection," *IEEE Microwave and Guided Wave Letters*, vol. 9, no. 11, pp. 470–472, 1999.

[28] I. T. Rekanos, S. M. Panas, and T. D. Tsiboukis, "Microwave imaging using the finite-element method and a sensitivity analysis approach," *IEEE Transactions on Medical Imaging*, vol. 18, no. 11, pp. 1108–1114, 1999.

[29] A. G. Bell, "On the production and reproduction of sound by light," *American Journal of Science*, vol. 20, pp. 305–324, 1880.

[30] V. E. Gusev and A. A. Karabutov, *Laser Optoacoustics*. New York: American Institute of Physics, 1993.

[31] G. Ku and L. H. V. Wang, "Scanning microwave-induced thermoacoustic tomography: Signal, resolution, and contrast," *Medical Physics*, vol. 28, no. 1, pp. 4–10, 2001.

[32] A. A. Karabutov, E. V. Savateeva, and A. A. Oraevsky, "Optoacoustic tomography: New modality of laser diagnostic systems," *Laser Physics*, vol. 13, no. 5, pp. 711–723, 2003.

[33] R. G. M. Kolkman, E. Hondebrink, W. Steenbergen, and F. F. M. de Mul, "In vivo photoacoustic imaging of blood vessels using an extreme-narrow aperture sensor," *IEEE Journal of Selected Topics in Quantum Electronics*, vol. 9, no. 2, pp. 343–346, 2003.

[34] R. G. M. Kolkman, J. H. G. M. Klaessens, E. Hondebrink, J. C. W. Hopman, F. F. M. de Mul, W. Steenbergen, J. M. Thijssen, and T. G. van Leeuwen,

"Photoacoustic determination of blood vessel diameter," *Physics in Medicine and Biology*, vol. 49, no. 20, pp. 4745–4756, 2004.

[35] J. J. Niederhauser, M. Jaeger, and M. Frenz, "Real-time three-dimensional optoacoustic imaging using an acoustic lens system," *Applied Physics Letters*, vol. 85, no. 5, pp. 846–848, 2004.

[36] T. Nakata and T. Ninomiya, "Real-time photodisplacement imaging using parallel excitation and parallel heterodyne interferometry," *Journal of Applied Physics*, vol. 97, no. 10, p. 103110, 2005.

[37] K. Maslov, G. Stoica, and L. V. H. Wang, "In vivo dark-field reflection-mode photoacoustic microscopy," *Optics Letters*, vol. 30, no. 6, pp. 625–627, 2005.

[38] H. F. Zhang, K. Maslov, G. Stoica, and L. H. V. Wang, "Functional photoacoustic microscopy for high-resolution and noninvasive in vivo imaging," *Nature Biotechnology*, vol. 24, no. 7, pp. 848–851, 2006.

[39] R. A. Kruger, P. Y. Liu, Y. R. Fang, and C. R. Appledorn, "Photoacoustic ultrasound (PAUS) - reconstruction tomography," *Medical Physics*, vol. 22, no. 10, pp. 1605–1609, 1995.

[40] R. A. Kruger, D. R. Reinecke, and G. A. Kruger, "Thermoacoustic computed tomography-technical considerations," *Medical Physics*, vol. 26, no. 9, pp. 1832–1837, 1999.

[41] Y. V. Zhulina, "Optimal statistical approach to optoacoustic image reconstruction," *Applied Optics*, vol. 39, no. 32, pp. 5971–5977, 2000.

[42] C. G. A. Hoelen and F. F. M. de Mul, "Image reconstruction for photoacoustic scanning of tissue structures," *Applied Optics*, vol. 39, no. 31, pp. 5872–5883, 2000.

[43] K. P. Kostli, D. Frauchiger, J. J. Niederhauser, G. Paltauf, H. P. Weber, and M. Frenz, "Optoacoustic imaging using a three-dimensional reconstruction algorithm," *IEEE Journal of Selected Topics in Quantum Electronics*, vol. 7, no. 6, pp. 918–923, 2001.

[44] K. P. Kostli and P. C. Beard, "Two-dimensional photoacoustic imaging by use of fourier-transform image reconstruction and a detector with an anisotropic response," *Applied Optics*, vol. 42, no. 10, pp. 1899–1908, 2003.

[45] M. C. Pilatou, N. J. Voogd, F. F. M. de Mul, W. Steenbergen, and L. N. A. van Adrichem, "Analysis of three-dimensional photoacoustic imaging of a vascular tree in vitro," *Review of Scientific Instruments*, vol. 74, no. 10, pp. 4495–4499, 2003.

[46] H. Haltmeier, O. Scherzer, P. Burgholzer, and G. Paltauf, "Thermoacoustic computed tomography with large planar receiver," *Inverse Problems*, vol. 20, pp. 1663–1673, 2004.

[47] L. H. V. Wang and H.-i. Wu, *Biomedical Optics: Principles and Imaging.* Wiley, 2007.

[48] M. H. Xu and L. H. V. Wang, "Analytic explanation of spatial resolution related to bandwidth and detector aperture size in thermoacoustic or photoacoustic reconstruction," *Physical Review E*, vol. 67, no. 5, p. 056605, 2003.

[49] Z. Guo, L. Li, and L. H. V. Wang, "Speckle-free nature of photoacoustic tomography," *Medical Physics*, vol. 36, no. 9, pp. 4084–4088, 2009.

[50] W. F. Cheong, S. A. Prahl, and A. J. Welch, "A review of the optical-properties of biological tissues," *IEEE Journal of Quantum Electronics*, vol. 26, no. 12, pp. 2166–2185, 1990.

[51] F. A. Duck, *Physical Properties of Tissue.* Academic Press Limited, 1990.

[52] M. H. Xu and L. H. V. Wang, "Photoacoustic imaging in biomedicine," *Review of Scientific Instruments*, vol. 77, no. 4, p. 041101, 2006.

[53] M. Pramanik, G. Ku, C. H. Li, and L. H. V. Wang, "Design and evaluation of a novel breast cancer detection system combining both thermoacoustic (TA) and photoacoustic (PA) tomography," *Medical Physics*, vol. 35, no. 6, pp. 2218–2223, 2008.

[54] M. Pramanik, G. Ku, and L. H. V. Wang, "Tangential resolution improvement in thermoacoustic and photoacoustic tomography using a negative acoustic lens," *Journal of Biomedical Optics*, vol. 14, no. 2, p. 024028, 2009.

[55] M. Pramanik, M. Swierczewska, D. Green, B. Sitharaman, and L. H. V. Wang, "Single-walled carbon nanotubes as a multimodal - thermoacoustic and photoacoustic - contrast agent," *Journal of Biomedical Optics*, vol. 14, no. 3, p. 034018, 2009.

[56] M. Pramanik, K. H. Song, M. Swierczewska, D. Green, B. Sitharaman, and L. H. V. Wang, "In vivo carbon nanotube-enhanced non-invasive photoacoustic mapping of the sentinel lymph node," *Physics in Medicine and Biology*, vol. 54, no. 11, pp. 3291–3301, 2009.

[57] D. Pan, M. Pramanik, A. Senpan, X. Yang, K. H. Song, M. J. Scott, H. Zhang, P. J. Gaffney, S. A. Wickline, L. H. V. Wang, and G. M. Lanza, "Molecular photoacoustic tomography with colloidal nanobeacons," *Angewandte Chemie International Edition*, vol. 48, no. 23, pp. 4170–4173, 2009.

[58] D. Pan, M. Pramanik, A. Senpan, S. Ghosh, S. A. Wickline, L. H. V. Wang, and G. M. Lanza, "Near infrared photoacoustic detection of sentinel lymph nodes with gold nanobeacons," *Biomaterials*, 2010 (In Press).

[59] M. Pramanik and L. H. V. Wang, "Thermoacoustic and photoacoustic sensing of temperature," *Journal of Biomedical Optics*, vol. 14, no. 5, p. 054024, 2009.

[60] S. J. Nass, I. C. Henderson, and J. C. Lashof, *Mammography and Beyond: Developing Techniques for the Early Detection of Breast Cancer*. Washington, D.C: Inst. Med.: Nat. Acad. Press, 2001.

[61] M. Lazebnik, D. Popovic, L. McCartney, C. B. Watkins, M. J. Lindstrom, J. Harter, S. Sewall, T. Ogilvie, A. Magliocco, T. M. Breslin, W. Temple, D. Mew, J. H. Booske, M. Okoniewski, and S. C. Hagness, "A large-scale study of the ultrawideband microwave dielectric properties of normal, benign and malignant breast tissues obtained from cancer surgeries," *Physics in Medicine and Biology*, vol. 52, no. 20, pp. 6093–6115, 2007.

[62] A. Swarup, S. S. Stuchly, and A. Surowiec, "Dielectric-properties of mouse MCA1 fibrosarcoma at different stages of development," *Bioelectromagnetics*, vol. 12, no. 1, pp. 1–8, 1991.

[63] IEEE Std, *IEEE standard for safety levels with respect to human exposure to radio frequency electromagnetic fields 3 kHz to 300 GHz*. IEEE Std C95.1, 1999.

[64] B. Monsees, J. M. Destouet, and W. G. Totty, "Light scanning versus mammography in breast cancer detection," *Radiology*, vol. 163, pp. 463–465, 1987.

[65] Y. W. Wang, X. Y. Xie, X. D. Wang, G. Ku, K. L. Gill, D. P. O'Neal, G. Stoica, and L. H. V. Wang, "Photoacoustic tomography of a nanoshell contrast agent in the in vivo rat brain," *Nano Letters*, vol. 4, no. 9, pp. 1689–1692, 2004.

[66] G. Ku, B. D. Fornage, X. Jin, M. H. Xu, K. K. Hunt, and L. H. V. Wang, "Thermoacoustic and photoacoustic tomography of thick biological tissues toward breast imaging," *Technology in Cancer Research and Treatment*, vol. 4, no. 5, pp. 559–565, 2005.

[67] G. Ku and L. H. V. Wang, "Deeply penetrating photoacoustic tomography in biological tissues enhanced with an optical contrast agent," *Optics Letters*, vol. 30, no. 5, pp. 507–509, 2005.

[68] Laser Institute of America, *American National Standard for Safe Use of Lasers ANSI Z136.1*. New York, NY: American National Standards Institute, Inc., 2000.

[69] M. H. Xu and L. H. V. Wang, "Time-domain reconstruction for thermoacoustic tomography in a spherical geometry," *IEEE Transactions on Medical Imaging*, vol. 21, no. 7, pp. 814–822, 2002.

[70] Y. Xu, D. Z. Feng, and L. H. V. Wang, "Exact frequency-domain reconstruction for thermoacoustic tomography - I: Planar geometry," *IEEE Transactions on Medical Imaging*, vol. 21, no. 7, pp. 823–828, 2002.

[71] Y. Xu, M. H. Xu, and L. H. V. Wang, "Exact frequency-domain reconstruction for thermoacoustic tomography – II: Cylindrical geometry," *IEEE Transactions on Medical Imaging*, vol. 21, no. 7, pp. 829–833, 2002.

[72] R. A. Kruger, K. K. Kopecky, A. M. Aisen, D. R. Reinecke, G. A. Kruger, and W. L. Kiser, "Thermoacoustic CT with radio waves: A medical imaging paradigm," *Radiology*, vol. 211, no. 1, pp. 275–278, 1999.

[73] R. A. Kruger, W. L. J. Kiser, A. P. Romilly, and P. Scmidt, "Thermoacoustic CT of the breast: pilot study observations," in *Proc. SPIE* (A. O. Alexander, ed.), vol. 4256, pp. 1–5, SPIE, 2001.

[74] A. A. Oraevsky, E. V. Savateeva, S. V. Solomatin, A. A. Karabutov, V. G. Andreev, Z. Gatalica, T. Khamapirad, and P. M. Henrichs, "Optoacoustic imaging of blood for visualization and diagnostics of breast cancer," in *Proc. SPIE* (A. A. Oraevsky, ed.), vol. 4618, pp. 81–94, 2002.

[75] X. D. Wang, Y. J. Pang, G. Ku, X. Y. Xie, G. Stoica, and L. H. V. Wang, "Non-invasive laser-induced photoacoustic tomography for structural and functional in vivo imaging of the brain," *Nature Biotechnology*, vol. 21, no. 7, pp. 803–806, 2003.

[76] G. Ku, X. D. Wang, X. Y. Xie, G. Stoica, and L. H. V. Wang, "Imaging of tumor angiogenesis in rat brains in vivo by photoacoustic tomography," *Applied Optics*, vol. 44, no. 5, pp. 770–775, 2005.

[77] C. H. Li, M. Pramanik, G. Ku, and L. H. V. Wang, "Image distortion in thermoacoustic tomography caused by microwave diffraction," *Physical Review E*, vol. 77, no. 3, p. 031923, 2008.

[78] C. H. Li, G. Ku, and L. H. V. Wang, "Negative lens concept for photoacoustic tomography," *Physical Review E*, vol. 78, no. 2, p. 021901, 2008.

[79] V. Ntziachristos, J. Ripoll, L. H. V. Wang, and R. Weissleder, "Looking and listening to light: the evolution of whole-body photonic imaging," *Nature Biotechnology*, vol. 23, no. 3, pp. 313–320, 2005.

114

[80] L. Ottobrini, P. Ciana, A. Biserni, G. Lucignani, and A. Maggi, "Molecular imaging: A new way to study molecular processes in vivo," *Molecular and Cellular Endocrinology*, vol. 246, no. 1-2, pp. 69–75, 2006.

[81] W. Krause, *Contrast agents II: Optical, Ultrasound, X-Ray Imaging and Radiopharmaceutical Imaging.* Springer, 2002.

[82] E. L. Ritman, "Molecular imaging in small animals - roles for micro-CT," *Journal of Cellular Biochemistry*, vol. 39, pp. 116–124, 2002.

[83] J. V. Frangioni, "In vivo near-infrared fluorescence imaging," *Current Opinion in Chemical Biology*, vol. 7, no. 5, pp. 626–634, 2003.

[84] S. R. Meikle, P. Kench, M. Kassiou, and R. B. Banati, "Small animal SPECT and its place in the matrix of molecular imaging technologies," *Physics in Medicine and Biology*, vol. 50, no. 22, pp. R45–R61, 2005.

[85] X. D. Wang, X. Y. Xie, G. N. Ku, and L. H. V. Wang, "Noninvasive imaging of hemoglobin concentration and oxygenation in the rat brain using high-resolution photoacoustic tomography," *Journal of Biomedical Optics*, vol. 11, no. 2, p. 024015, 2006.

[86] G. F. Lungu, M. L. Li, X. Y. Xie, L. H. V. Wang, and G. Stoica, "In vivo imaging and characterization of hypoxia-induced neovascularization and tumor invasion," *International Journal of Oncology*, vol. 30, no. 1, pp. 45–54, 2007.

[87] M. L. Li, J. T. Oh, X. Y. Xie, G. Ku, W. Wang, C. Li, G. Lungu, G. Stoica, and L. H. V. Wang, "Simultaneous molecular and hypoxia imaging of brain tumors in vivo using spectroscopic photoacoustic tomography," *Proc. IEEE*, vol. 96, no. 3, pp. 481–489, 2008.

[88] P. Vaupel, A. Mayer, S. Briest, and M. Hockel, "Oxygen transport to tissue XXVI," vol. 566, pp. 333–342, Springer, 2005.

[89] B. P. Schneider and K. D. Miller, "Angiogenesis of breast cancer," *Journal of Clinical Oncology*, vol. 23, no. 8, pp. 1782–1790, 2005.

[90] B. Sitharaman, K. R. Kissell, K. B. Hartman, L. A. Tran, A. Baikalov, I. Rusakova, Y. Sun, H. A. Khant, S. J. Ludtke, W. Chiu, S. Laus, E. Toth, L. Helm, A. E. Merbach, and L. J. Wilson, "Superparamagnetic gadonanotubes are high-performance MRI contrast agents," *Chemical Communications*, no. 31, pp. 3915–3917, 2005.

[91] P. Cherukuri, C. J. Gannon, T. K. Leeuw, H. K. Schmidt, R. E. Smalley, S. A. Curley, and R. B. Weisman, "Mammalian pharmacokinetics of carbon nanotubes using intrinsic near-infrared fluorescence," *PNAS*, vol. 103, no. 50, pp. 18882–18886, 2006.

[92] M. R. McDevitt, D. Chattopadhyay, B. J. Kappel, J. S. Jaggi, S. R. Schiffman, C. Antczak, J. T. Njardarson, R. Brentjens, and D. A. Scheinberg, "Tumor targeting with antibody-functionalized, radiolabeled carbon nanotubes," *Journal of Nuclear Medicine*, vol. 48, no. 7, pp. 1180–1189, 2007.

[93] Z. Liu, W. B. Cai, L. N. He, N. Nakayama, K. Chen, X. M. Sun, X. Y. Chen, and H. J. Dai, "In vivo biodistribution and highly efficient tumour targeting of carbon nanotubes in mice," *Nature Nanotechnology*, vol. 2, no. 1, pp. 47–52, 2007.

[94] M. E. Hughes, E. Brandin, and J. A. Golovchenko, "Optical absorption of DNA-carbon nanotube structures," *Nano Letters*, vol. 7, no. 5, pp. 1191–1194, 2007.

[95] S. Berciaud, L. Cognet, P. Poulin, R. B. Weisman, and B. Lounis, "Absorption spectroscopy of individual single-walled carbon nanotubes," *Nano Letters*, vol. 7, no. 5, pp. 1203–1207, 2007.

[96] C. J. Gannon, P. Cherukuri, B. I. Yakobson, L. Cognet, J. S. Kanzius, C. Kittrell, R. B. Weisman, M. Pasquali, H. K. Schmidt, R. E. Smalley, and S. A. Curley, "Carbon nanotube-enhanced thermal destruction of cancer cells in a noninvasive radiofrequency field," *Cancer*, vol. 110, no. 12, pp. 2654–2665, 2007.

[97] K. H. Song and L. H. V. Wang, "Deep reflection-mode photoacoustic imaging of biological tissue," *Journal of Biomedical Optics*, vol. 12, no. 6, p. 060503, 2007.

[98] M. J. O'Connell, S. M. Bachilo, C. B. Huffman, V. C. Moore, M. S. Strano, E. H. Haroz, K. L. Rialon, P. J. Boul, W. H. Noon, C. Kittrell, J. P. Ma, R. H. Hauge, R. B. Weisman, and R. E. Smalley, "Band gap fluorescence from individual single-walled carbon nanotubes," *Science*, vol. 297, no. 5581, pp. 593–596, 2002.

[99] A. Saib, L. Bednarz, R. Daussin, C. Bailly, X. Lou, J. M. Thomassin, C. Pagnoulle, C. Detrembleur, R. Jerome, and I. Huynen, "Carbon nanotube composites for broadband microwave absorbing materials," *IEEE Transactions on Microwave Theory and Techniques*, vol. 54, no. 6, pp. 2745–2754, 2006.

[100] C. A. Grimes, C. Mungle, D. Kouzoudis, S. Fang, and P. C. Eklund, "The 500 MHz to 5.50 GHz complex permittivity spectra of single-wall carbon nanotube-loaded polymer composites," *Chemical Physics Letters*, vol. 319, no. 5-6, pp. 460–464, 2000.

[101] P. C. P. Watts, W. K. Hsu, A. Barnes, and B. Chambers, "High permittivity from defective multiwalled carbon nanotubes in the X-band," *Advanced Materials*, vol. 15, no. 7-8, pp. 600–603, 2003.

[102] X. Jin, A. Keho, K. Meissner, and L. H. V. Wang, "Iron-oxide nanoparticles as a contrast agent in thermoacoustic tomography," in *Proc. SPIE*, vol. 6437, 2007.

[103] M. Eghtedari, A. Oraevsky, J. A. Copland, N. A. Kotov, A. Conjusteau, and M. Motamedi, "High sensitivity of in vivo detection of gold nanorods using a laser optoacoustic imaging system," *Nano Letters*, vol. 7, no. 7, pp. 1914–1918, 2007.

[104] K. Yamamoto, T. Kamimura, and K. Matsumoto, "Nitrogen doping of single-walled carbon nanotube by using mass-separated low-energy ion beams," *Japanese Journal of Applied Physics Part 1-Regular Papers Short Notes and Review Papers*, vol. 44, no. 4A, pp. 1611–1614, 2005.

[105] A. De La Zerda, C. Zavaleta, S. Keren, S. Vaithilingam, S. Bodapati, Z. Liu, J. Levi, B. R. Smith, T. J. Ma, O. Oralkan, Z. Cheng, X. Y. Chen, H. J. Dai, B. T. Khuri-Yakub, and S. S. Gambhir, "Carbon nanotubes as photoacoustic molecular imaging agents in living mice," *Nature Nanotechnology*, vol. 3, no. 9, pp. 557–562, 2008.

[106] N. W. S. Kam, M. O'Connell, J. A. Wisdom, and H. J. Dai, "Carbon nanotubes as multifunctional biological transporters and near-infrared agents for selective cancer cell destruction," *PNAS*, vol. 102, no. 33, pp. 11600–11605, 2005.

[107] NIH Consensus Statement, *Treatment of early stage breast cancer NIH Consensus Statement*, vol. 8. 1990.

[108] K. K. Swenson, M. J. Nissen, C. Ceronsky, L. Swenson, M. W. Lee, and T. M. Tuttle, "Comparison of side effects between sentinel lymph node and axillary lymph node dissection for breast cancer," *Annals of Surgical Oncology*, vol. 9, no. 8, pp. 745–753, 2002.

[109] D. Krag, D. Weaver, T. Ashikaga, F. Moffat, V. S. Klimberg, C. Shriver, S. Feldman, R. Kusminsky, M. Gadd, J. Kuhn, S. Harlow, and P. Beitsch, "The sentinel node in breast cancer - a multicenter validation study," *New England Journal of Medicine*, vol. 339, no. 14, pp. 941–946, 1998.

[110] K. M. McMasters, T. M. Tuttle, D. J. Carlson, C. M. Brown, R. D. Noyes, R. L. Glaser, D. J. Vennekotter, P. S. Turk, P. S. Tate, A. Sardi, P. B. Cerrito, and M. J. Edwards, "Sentinel lymph node biopsy for breast cancer: A suitable alternative to routine axillary dissection in multi-institutional practice when optimal technique is used," *Journal of Clinical Oncology*, vol. 18, no. 13, pp. 2560–2566, 2000.

[111] P. Borgstein, "Intradermal blue dye to identify sentinel lymph node in breast cancer - reply," *Lancet*, vol. 350, no. 9082, pp. 958–958, 1997.

[112] O. A. Ung, "Australasian experience and trials in sentinel lymph node biopsy: the RACS SNAC trial," *Asian Journal of Surgery*, vol. 27, pp. 284–290, 2004.

[113] A. D. Purushotham, S. Upponi, M. B. Klevesath, L. Bobrow, K. Millar, J. P. Myles, and S. W. Duffy, "Morbidity after sentinel lymph node biopsy in primary breast cancer: Results from a randomized controlled trial," *Journal of Clinical Oncology*, vol. 23, no. 19, pp. 4312–4321, 2005.

[114] S. Krishnamurthy, N. Sneige, D. G. Bedi, B. S. Edieken, B. D. Fornage, H. M. Kuerer, S. E. Singletary, and K. K. Hunt, "Role of ultrasound-guided fine-needle aspiration of indeterminate and suspicious axillary lymph nodes in the initial staging of breast carcinoma," *Cancer*, vol. 95, no. 5, pp. 982–988, 2002.

[115] E. E. Deurloo, P. J. Tanis, K. G. A. Gilhuijs, S. H. Muller, R. Kroger, J. L. Peterse, E. J. T. Rutgers, R. V. Olmos, and L. J. S. Kool, "Reduction in the number of sentinel lymph node procedures by preoperative ultrasonography of the axilla in breast cancer," *European Journal of Cancer*, vol. 39, no. 8, pp. 1068–1073, 2003.

[116] B. Brancato, M. Zappa, D. Bricolo, S. Catarzi, G. Risso, R. Bonardi, P. Cariaggi, A. Bianchin, P. Bricolo, M. Rosselli Del Turco, L. Cataliotti, S. Bianchi, and S. Ciatto, "Role of ultrasound-guided fine needle cytology of axillary lymph nodes in breast carcinoma staging," *Radiol Med*, vol. 108, no. 4, pp. 345–55, 2004.

[117] K. H. Song, E. W. Stein, J. A. Margenthaler, and L. H. V. Wang, "Noninvasive photoacoustic identification of sentinel lymph nodes containing methylene blue in vivo in a rat model," *Journal of Biomedical Optics*, vol. 13, no. 5, p. 054033, 2008.

[118] B. Z. Yin, D. Xing, Y. Wang, Y. G. Zeng, Y. G. Zeng, Y. Tan, and Q. Chen, "Fast photoacoustic imaging system based on 320-element linear transducer array," *Physics in Medicine and Biology*, vol. 49, no. 7, pp. 1339–1346, 2004.

[119] Y. G. Zeng, D. Xing, Y. Wang, B. Z. Yin, and Q. Chen, "Photoacoustic and ultrasonic coimage with a linear transducer array," *Optics Letters*, vol. 29, no. 15, pp. 1760–1762, 2004.

[120] D. W. Yang, D. Xing, H. M. Gu, Y. Tan, and L. M. Zeng, "Fast multi-element phase-controlled photoacoustic imaging based on limited-field-filtered back-projection algorithm," *Applied Physics Letters*, vol. 87, no. 19, p. 194101, 2005.

[121] R. Weissleder and U. Mahmood, "Molecular imaging," *Radiology*, vol. 219, no. 2, pp. 316–333, 2001.

[122] P. M. Winter, S. D. Caruthers, S. A. Wickline, and G. M. Lanza, "Nanotechnologies for cellular and molecular imaging by MRI," pp. 227–49, 2005.

[123] G. M. Whitesides, "Nanoscience, nanotechnology, and chemistry," *Small*, vol. 1, no. 2, pp. 172–179, 2005.

[124] R. Weissleder, K. Kelly, E. Y. Sun, T. Shtatland, and L. Josephson, "Cell-specific targeting of nanoparticles by multivalent attachment of small molecules," *Nature Biotechnology*, vol. 23, no. 11, pp. 1418–1423, 2005.

[125] S. D. Caruthers, S. A. Wickline, and G. M. Lanza, "Nanotechnological applications in medicine," *Current Opinion in Biotechnology*, vol. 18, no. 1, pp. 26–30, 2007.

[126] I. J. Majoros and J. J. R. Baker, *Dendrimer Based Nanomedicine*. Pan Stanford Pb., 2008.

[127] D. Pan, G. M. Lanza, S. A. Wickline, and S. D. Caruthers, "Nanomedicine: Perspective and promises with ligand-directed molecular imaging," *European Journal of Radiology*, vol. 70, pp. 274–285, 2009.

[128] C. J. Hawker and K. L. Wooley, "The convergence of synthetic organic and polymer chemistries," *Science*, vol. 309, no. 5738, pp. 1200–1205, 2005.

[129] R. K. O'Reilly, C. J. Hawker, and K. L. Wooley, "Cross-linked block copolymer micelles: functional nanostructures of great potential and versatility," *Chemical Society Reviews*, vol. 35, no. 11, pp. 1068–1083, 2006.

[130] A. Agarwal, S. W. Huang, M. O'Donnell, K. C. Day, M. Day, N. Kotov, and S. Ashkenazi, "Targeted gold nanorod contrast agent for prostate cancer detection by photoacoustic imaging," *Journal of Applied Physics*, vol. 102, no. 6, p. 064701, 2007.

[131] S. Raut and P. J. Gaffney, "Evaluation of the fibrin binding profile of two anti-fibrin monoclonal antibodies," *Thrombosis and Haemostasis*, vol. 76, no. 1, pp. 56–64, 1996.

[132] K. H. Song, C. H. Kim, C. M. Cobley, Y. N. Xia, and L. H. V. Wang, "Near-infrared gold nanocages as a new class of tracers for photoacoustic sentinel lymph node mapping on a rat model," *Nano Letters*, vol. 9, no. 1, pp. 183–188, 2009.

[133] K. H. Song, C. H. Kim, K. Maslov, and L. H. V. Wang, "Noninvasive in vivo spectroscopic nanorod-contrast photoacoustic mapping of sentinel lymph nodes," *European Journal of Radiology*, vol. 70, no. 2, pp. 227–231, 2009.

[134] J. W. Kim, E. I. Galanzha, E. V. Shashkov, H. M. Moon, and V. P. Zharov, "Golden carbon nanotubes as multimodal photoacoustic and photothermal high-contrast molecular agents," *Nature Nanotechnology*, vol. 4, no. 10, pp. 688–694, 2009.

[135] G. Laruelle, J. Francios, and L. Billon, "Self-assembly in aqueous media of amphiphilic poly acrylic acid based di-block copolymers synthesized by direct nitroxide-mediated polymerization," *Macromolecular Rapid Communications*, vol. 25, no. 21, pp. 1839–1844, 2004.

[136] H. Y. Huang, T. Kowalewski, E. E. Remsen, R. Gertzmann, and K. L. Wooley, "Hydrogel-coated glassy nanospheres: A novel method for the synthesis of shell cross-linked knedels," *Journal of the American Chemical Society*, vol. 119, no. 48, pp. 11653–11659, 1997.

[137] J. Wu and A. Eisenberg, "Proton diffusion across membranes of vesicles of poly(styrene-b-acrylic acid) diblock copolymers," *Journal of the American Chemical Society*, vol. 128, no. 9, pp. 2880–2884, 2006.

[138] J. Xu, G. Sun, R. Rossin, A. Hagooly, Z. Li, K. Fukukawa, B. W. Messmore, D. A. Moore, M. J. Welch, C. J. Hawker, and K. L. Wooley, "Labeling of polymer nanostructures for medical imaging: Importance of charge density, spacer length, and crosslinking extents," *Macromolecules*, vol. 40, no. 9, pp. 2971–2973, 2007.

[139] I. V. Larina, K. V. Larin, and R. O. Esenaliev, "Real-time optoacoustic monitoring of temperature in tissues," *Journal of Physics D-Applied Physics*, vol. 38, no. 15, pp. 2633–2639, 2005.

[140] A. J. Welch and M. J. C. Van Gemert, *Optical-Thermal Response of Laser-Irradiated Tissue*. New York: Plenum, 1995.

[141] R. Seip and E. S. Ebbini, "Noninvasive estimation of tissue temperature response to heating fields using diagnostic ultrasound," *IEEE Transactions on Biomedical Engineering*, vol. 42, no. 8, pp. 828–839, 1995.

[142] R. Seip, P. VanBaren, C. A. Cain, and E. S. Ebbini, "Noninvasive real-time multipoint temperature control for ultrasound phased array treatments," *IEEE Transactions on Ultrasonics Ferroelectrics and Frequency Control*, vol. 43, no. 6, pp. 1063–1073, 1996.

[143] R. MaassMoreno and C. A. Damianou, "Noninvasive temperature estimation in tissue via ultrasound echo-shifts .1. analytical model," *Journal of the Acoustical Society of America*, vol. 100, no. 4, pp. 2514–2521, 1996.

[144] S. J. Graham, M. J. Bronskill, and R. M. Henkelman, "Time and temperature dependence of MR parameters during thermal coagulation of ex vivo rabbit muscle," *Magnetic Resonance in Medicine*, vol. 39, no. 2, pp. 198–203, 1998.

[145] P. Steiner, R. Botnar, B. Dubno, G. G. Zimmermann, G. S. Gazelle, and J. F. Debatin, "Radio-frequency-induced thermoablation: Monitoring with T1-weighted and proton-frequency-shift MR imaging in an interventional 0.5-T environment," *Radiology*, vol. 206, no. 3, pp. 803–810, 1998.

[146] S. Y. Emelianov, S. R. Aglyamov, A. B. Karpiouk, S. Mallidi, S. Park, S. Sethuraman, J. Shah, R. W. Smalling, J. M. Rubin, and W. G. Scott, "Synergy and applications of combined ultrasound, elasticity, and photacoustic imaging," in *Proc. IEEE Ultrasound Symp*, pp. 405–415, 2006.

[147] J. Shah, S. R. Aglyamov, K. Sokolov, T. E. Milner, and S. Y. Emelianov, "Ultrasound-based thermal and elasticity imaging to assist photothermal cancer therapy preliminary study," *Proc. IEEE Ultrason Symp*, pp. 1029–1032, 2006.

[148] S. Sethuraman, S. R. Aglyamov, R. W. Smalling, and S. Y. Emelianov, "Remote temperature estimation in intravascular photoacoustic imaging," *Ultrasound Med Biol*, vol. 34, no. 2, pp. 299–308, 2008.

[149] J. Shah, S. Park, S. R. Aglyamov, T. Larson, L. Ma, K. Sokolov, K. Johnston, T. E. Milner, and S. Y. Emelianov, "Photoaoustic imaging and temperature measurement for photothermal cancer therapy," *Journal of Biomedical Optics*, vol. 13, no. 3, p. 034024, 2008.

[150] S. H. Wang, C. W. Wei, S. H. Jee, and P. C. Li, "Photoacoustic temperature measurements for monitoring of thermal therapy," in *Proc. SPIE*, vol. 7177, p. 71771S, 2009.

[151] J. A. D. Matthew, *CRC Handbook of Chemistry and Physics - Weast,Rc*, vol. 331. 1988.

[152] *Handbook of physical quantities*. Boca Raton: CRC Press, 1997.

[153] Department of Health & Human Services, *Food and Drug Administration Modernization Act of 1997; Modifications to the List of Recognized Standards, Recognition List Number: 011*. FDA Docket No. 2004N-0226 2004.

[154] IEC 60601-2-33, *Medical Electrical Equipment - Part 2: Particular Requirements for the Safety of Magnetic Resonance Equipment for Medical Diagnosis*. 2002.

[155] C. H. Li, G. W. Kattawar, P. W. Zhai, and P. Yang, "Electric and magnetic energy density distributions inside and outside dielectric particles illuminated

by a plane electromagnetic wave," *Optics Express*, vol. 13, no. 12, pp. 4554–4559, 2005.

[156] A. Taflove and S. C. Hagness, *Computational Electrodynamics: The Finite-Difference Time-Domain Method*. Boston, MA: Artech House Publishers, 2000.

[157] X. Li and S. C. Hagness, "A confocal microwave imaging algorithm for breast cancer detection," *IEEE Microwave and Wireless Components Letters*, vol. 11, no. 3, pp. 130–132, 2001.

[158] Q. Fu, S. M. Huang, and J. Liu, "Chemical vapor depositions of single-walled carbon nanotubes catalyzed by uniform Fe_2O_3 nanoclusters synthesized using diblock copolymer micelles," *Journal of Physical Chemistry B*, vol. 108, no. 20, pp. 6124–6129, 2004.

[159] M. S. Dresselhaus, G. Dresselhaus, R. Saito, and A. Jorio, "Raman spectroscopy of carbon nanotubes," *Physics Reports-Review Section of Physics Letters*, vol. 409, no. 2, pp. 47–99, 2005.

[160] B. White, S. Banerjee, S. O'Brien, N. J. Turro, and I. P. Herman, "Zeta-potential measurements of surfactant-wrapped individual single-walled carbon nanotubes," *Journal of Physical Chemistry C*, vol. 111, no. 37, pp. 13684–13690, 2007.

[161] J. Gamelin, A. Aguirre, A. Maurudis, F. Huang, D. Castillo, L. H. V. Wang, and Q. Zhu, "Curved array photoacoustic tomographic system for small animal imaging," *Journal of Biomedical Optics*, vol. 13, no. 2, p. 024007, 2008.

[162] M. H. Xu and L. H. V. Wang, "Universal back-projection algorithm for photoacoustic computed tomography," *Physical Review E*, vol. 71, no. 1, p. 016706, 2005.

Vita

Manojit Pramanik

Date of Birth   August 7, 1981

Place of Birth   Haldia (W.B.), India

Degrees   B.Tech. Electrical Engineering, 2002
M.Tech. Instrumentation Engineering, 2004
Ph.D. Biomedical Engineering, May 2010

Publications   [Pan, D., Pramanik, M.], et al. (2010). *Biomaterials* **In Press**.

Pramanik, M. and Wang, L. H. V. (2009). *J. Biomed. Opt.* **14**(5), 054024.

Pramanik, M., Song, K. H., et al. (2009). *Phys. Med. Biol.* **54**(11), 3291–3301.

[Pan, D., Pramanik, M.], et al. (2009). *Angew. Chem. Int. Ed.* **48**(23), 4170–4173.

Pramanik, M., Ku, G., et al. (2009). *J. Biomed. Opt.* **14**(2), 024028.

Pramanik, M., Swierczewska, M., et al. (2009). *J. Biomed. Opt.* **14**(3), 034018.

Pramanik, M., Ku, G., et al. (2008). *Med. Phys.* **35**(6), 2218–2223.

Li, C. H., Pramanik, M., et al. (2008). *Phys. Rev. E* **77**(3), 031023.

May 2010

Dual-modality imaging, Pramanik, Ph.D., 2010